DESIGN AND CHARACTERIZATION OF SURFACE-ENHANCED RAMAN SCATTERING NANOPARTICLES AS SPECTROSCOPIC PROBES FOR BIOLOGICAL IMAGING

BY

BRENT M DEVETTER

DISSERTATION

Submitted in partial fulfillment of the requirements
for the degree of Doctor of Philosophy in Electrical and Computer Engineering
in the Graduate College of the
University of Illinois at Urbana-Champaign, 2016

Urbana, Illinois

Doctoral Committee:

Professor Rohit Bhargava, Chair
Professor Catherine J. Murphy
Associate Professor Gang Logan Liu
Assistant Professor Wenjuan Zhu

ABSTRACT

The development of highly sensitive and chemically specific optical probes has only been marginally realized to date. Surface-enhanced Raman spectroscopy (SERS) is an emerging technique that offers both chemical sensitivity and specificity. This dissertation examines the rational design, synthesis, characterization, and application of SERS-based optical probes designed for biological imaging and chemical sensing experiments. Special attention is paid to both the probe stability and the stability of its chemical signature. Our results indicate that significant care is required to successfully manufacture and use probes that are intended for biological investigation. An inner-filter effect between the extinction of light propagating through a matrix of probes, modeled as a colloidal solution, and surface-enhancement requires precise selection of the laser excitation wavelength and the optical properties of the probe. Metallic nanostructures consisting of noble metals such as gold and silver were investigated as probes because they provide intense surface-enhancement effects and the ability to tune their optical properties as desired. In particular, gold nanostructures are highly desirable because of their biocompatibility and inertness. Surface chemistry modification and characterization of metallic nanostructures were investigated to further our understanding of the requirements needed for preparing highly stable probes. Light scattering simulations were performed to predict the influence of certain geometries, materials, and illumination modalities on the probe's optical properties. This dissertation discusses studies that have investigated the long-term stability nanoprobes, the kinetics of surface ligand exchange, nanoprobe imaging in cellular systems, the properties of reflective substrates, and electron microscopy characterization of metallic nanostructures.

ACKNOWLEDGMENTS

I would like to acknowledge support from the University of Illinois at Urbana-Champaign *via* the NIH National Cancer Institute Alliance for Nanotechnology in Cancer Midwest Cancer Nanotechnology Training Center Grant R25 CA154015A. Our research was supported by a Beckman Institute seed grant and National Science Foundation grant CHE 0957849. Transmission electron microscopy, optical absorption spectroscopy, and dynamic light scattering/ζ-potential measurements were carried out in part at the Frederick Seitz Materials Research Laboratory Central Research Facilities, University of Illinois. I would also like to acknowledge my advisor, Rohit Bhargava, my coworkers, and collaborators especially Amish Shah, Sean Sivapalan, and Matthew Schulmerich.

TABLE OF CONTENTS

CHAPTER 1 INTRODUCTION 1
1.1 Minimally invasive diagnostics: Optical probes and chemical sensing 1
1.2 Optical properties of metals 4
1.3 Light scattering 8
1.4 Surface-enhanced Raman spectroscopy (SERS) 10
1.5 Light propagation and enhancement 13
1.6 Analytical light scattering calculations 16
1.7 Numerical light scattering calculations 18
1.8 Gold nanoparticle synthesis and characterization 23
1.9 Recent applications of SERS 25
1.10 Dissertation overview 28
1.11 References 30

CHAPTER 2 COMPUTATIONAL STUDY OF THE SURFACE-ENHANCED RAMAN SCATTERING FROM SILICA-COATED SILVER NANOWIRES 37
2.1 Introduction 37
2.2 Results and discussion 40
2.3 Conclusion 46
2.4 References 47

CHAPTER 3 OBSERVATION OF MOLECULAR DIFFUSION IN POLYELECTROLYTE-WRAPPED SURFACE-ENHANCED RAMAN SCATTERING NANOPROBES 49
3.1 Introduction 49
3.2 Experimental 52
3.3 Results and discussion 55
3.4 Conclusion 68
3.5 References 69

CHAPTER 4 MEASURING BINDING KINETICS OF AROMATIC THIOLATED MOLECULES WITH NANOPARTICLES *VIA* SURFACE-ENHANCED RAMAN SPECTROSCOPY 71
4.1 Introduction 71
4.2 Theory 74

4.3 Results and discussion 79
4.4 Experimental 92
4.5 Conclusion 94
4.6 References 95

CHAPTER 5 NUCLEAR-TARGETED SURFACE-ENHANCED RAMAN SCATTERING NANOPARTICLES 98
5.1 Introduction 98
5.2 Theory 100
5.3 Results and discussion 105
5.4 Experimental 111
5.5 References 115

CHAPTER 6 REFLECTIVE SUBSTRATES IN MID-INFRARED SPECTROSCOPY 117
6.1 Introduction 117
6.2 Theory 118
6.3 Results and discussion 121
6.4 Experimental 132
6.5 Conclusion 132
6.6 References 133

CHAPTER 7 COHERENT NANOAREA ELECTRON DIFFRACTION OF AU@AG NANORODS REVEALS STRUCTURAL INFORMATION 135
7.1 Introduction 135
7.2 Results and discussion 136
7.3 Experimental 141
7.4 References 143

CHAPTER 1

INTRODUCTION

1.1 Minimally invasive diagnostics: Optical probes and chemical sensing

As the quality of life and lifespan of our society has improved, it has become increasingly vital to develop new medical technologies that can help identify and lead to the eradication of devastating diseases such as cancer. The development and advancement of novel nanotechnologies within the last thirty years has encouraged the cultivation of medical, computing, and scientific breakthroughs that have transformed society. Broadly speaking, nanotechnology involves objects or structures with feature sizes on the order of 1 – 100 nm.[1] Metallic nanostructures—due to their brilliant optical properties—have been inadvertently used since as least as early as the Roman Empire (*circa* 300 AD) in stained glass created by skilled artisans.[2] Modern-day usage has shifted away from artwork and has focused on the development, design, and theoretical treatment of applications as diverse as data storage,[3–5] optical displays,[4,6] solar energy,[7,8] and medical diagnostics and therapeutics.[9,10] As a truly interdisciplinary subject area, metallic nanostructures and their applications incorporate the work of chemists, physicists, biologists, and engineers. In this dissertation, we focus on a portion of this burgeoning field: the development of highly sensitive and reproducible optical probes specifically for biological and chemical sensing purposes.

The ability to perform optical imaging at the cellular and subcellular level is exceedingly difficult due to a lack of optical contrast; in other words, the change in index of refraction between subcellular components is quite small and, as a result, we cannot easily image cells using bright-field optical microscopy. While certain techniques such as phase-contrast microscopy can improve image quality and highlight small changes in index of refraction, it still

does not reveal important chemical differences between cells.[11] Clinical diagnosis of cancers at the cellular level requires a highly skilled pathologist to examine chemically stained tissue sections using chromophores, such as hematoxylin and eosin (H&E), for additional contrast. Constituents such as DNA, receptors, and other biomolecules that act as biomarkers for disease are dimensionally below the diffraction-limit of light such that it is not possible to directly image these components with a light microscope. Grading or examination of the tissue, unfortunately, is subject to a certain of degree of interpretation and opinion. As a result, the pathologist makes decisions based on morphology and the chemical information provided immunohistochemical stains. While not the subject of this dissertation, label-free spectroscopic-based imaging techniques that utilize the innate chemical contrast of various biomolecules are promising but have yet to be widely used, in part, due to instrumentation requirements, algorithm development, and additional engineering before widespread commercialization.[12–14]

To overcome the lack of optical contrast in cells and tissues new contrast agents beyond those of simple immunohistochemical stains have been developed. These contrast agents are a popular and successful avenue for visualizing the spatial distribution of cellular features. Traditionally, contrast agents such as fluorescent dye molecules[15,16] were used in biomedical imaging applications but new materials have been recently developed that surpass the capabilities of fluorophores, which are prone to photobleaching. Modern nanotechnology has brought about the development of semiconductor quantum dots consisting of materials such as cadmium selenide (CdSe), cadmium sulfide (CdS), and cadmium telluride (CdTe). Quantum dots have been shown to be a promising alternative to fluorescent dyes because they are less susceptible to photobleaching and may be excited with ultraviolet light regardless of the quantum dot's emission wavelength.[17–19] Both fluorophores and quantum dots suffer from a few crucial

flaws: they are cytotoxic, have nonspecific emission profiles, and generally emit visible light, which is absorbed by tissues.[20] For *in vivo* applications, highly cytotoxic materials such as cadmium are generally unacceptable for clinical use except in the most dire situations. Researchers have investigated various coatings and surface chemistries for quantum dots to minimize cytotoxicity, but considerable concern lingers for how the body may tolerate and accumulate these toxic metal-containing materials over long periods of time.[21]

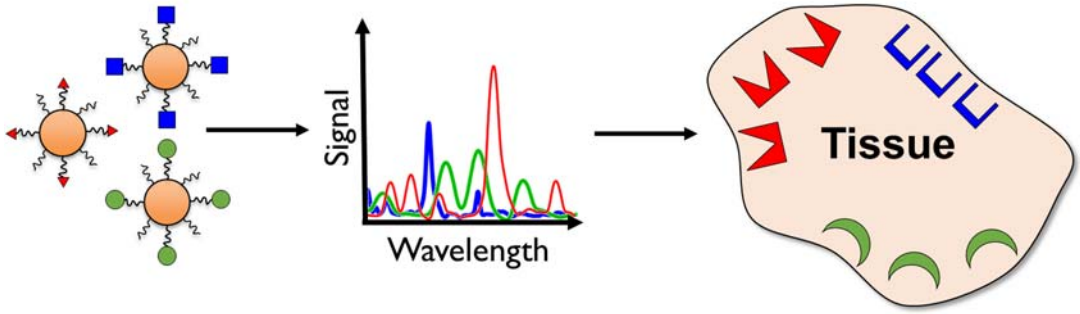

Figure 1.1. Schematic overview of molecularly specific and targeted gold nanoprobes for tissue imaging applications. Gold nanoprobes offer biocompatibility, robust surface functionalization chemistries, and are not susceptible to photobleaching. Unique emission profiles for each variety of nanoprobe allow for simultaneous multiplexing.

Noble metal (particularly gold) nanostructures, on the other hand, are highly promising as optical probes for cellular labeling, as shown in Figure 1.1, and chemical imaging studies. Metallic nanostructures can enhance chemically specific emission profiles and exhibit sensitivities approaching that of fluorescence.[22] Gold nanostructures, unlike cadmium-based alloys, are considered to be a chemically inert material and even have a medical history of being biologically safe. Colloidal gold has been used to treat rheumatoid arthritis and numerous studies have shown that properly functionalized gold nanostructures exhibit minimal toxicity both *in vivo* and *in vitro*.[23–25] In fact, the average human weighing 70 kg contains roughly 2.5 mg of gold as a result of environmental exposure.[23] The inertness of nanosized gold along with its

brilliant optical properties have made many researchers hopeful of new diagnostic opportunities in medicine.

1.2 Optical properties of metals

The extraordinary optical properties of colloidal metallic nanostructures may be described *via* a modification of the semi-classical Lorentz model for dielectrics.[26] The most generalized form of the Lorentz model assumes that dielectric materials act as damped, driven harmonic oscillators where electrons behave as masses attached to springs and oscillate in response to the driving force of incident light. A time-harmonic incident electric field $\mathbf{E}(t) = \mathbf{E}_0 \mathrm{e}^{-\mathrm{i}\omega t}$ is assumed to act as acting as the driving force (*i.e.*, $\mathbf{F}_{\text{driving}} = -e\mathbf{E}(t)$), where $-e$ is the charge of an electron (1.60218×10^{-19} C). A restoring force $\mathbf{F}_{\text{restoring}} = -k\mathbf{x} = -m\omega_0^2\mathbf{x}$ accounts for bound electrons, where k is the spring constant, $\mathbf{x}$ is the displacement vector, m is the mass of an electron (9.10938×10^{-31} kg), and ω_0 is the frequency of the oscillator ($\omega_0 = \sqrt{k/m}$). To broadly account for losses caused by effects such as electron-electron scattering, electron-lattice collisions, and other quantum mechanical interactions we define a damping coefficient γ and a subsequent damping force $\mathbf{F}_{\text{damping}} = -m\gamma\dot{\mathbf{x}}$. We may use and rearrange Newton's second law for a driven, damped harmonic oscillator ($m\ddot{\mathbf{x}} = \mathbf{F}_{\text{driving}} + \mathbf{F}_{\text{damping}} + \mathbf{F}_{\text{restoring}}$) as the following:

$$m\ddot{\mathbf{x}} + m\gamma\dot{\mathbf{x}} + m\omega_0^2\mathbf{x} = -e\mathbf{E}(t) \tag{1.1}$$

Assuming a time-harmonic solution $\mathbf{x}(t) = \mathbf{x}_0 e^{-\mathrm{i}\omega t}$, we may solve for $\mathbf{x}(t)$:

$$\mathbf{x}(t) = -\frac{e}{m}\mathbf{E}(t)\frac{1}{(\omega_0^2 - \omega^2) - i\gamma\omega} \tag{1.2}$$

The macroscopic polarization vector for N electrons ($\mathbf{P} = Ne\mathbf{x}(t)$) may be used to relate the displacement to a more useful quantity such as permittivity:

$$\mathbf{D} = \varepsilon_0\mathbf{E} + \mathbf{P} = \varepsilon\mathbf{E} \tag{1.3}$$

where **D** is the electric field displacement vector, ε_0 is the permittivity of free-space, and ε is an effective permittivity for an arbitrary dielectric material. Therefore, the relative permittivity of a dielectric material may be described as:

$$\varepsilon_r = \varepsilon / \varepsilon_0 = 1 - \frac{\omega_p^2}{(\omega^2 - \omega_0^2) - i\gamma\omega} \tag{1.4}$$

where $\omega_p = \sqrt{Ne^2 / m\varepsilon_0}$ is the plasma frequency of the material. Expanding the real and imaginary components ($\varepsilon_r = \varepsilon_r' + i\varepsilon_r''$) of the relative permittivity leads to:

$$\varepsilon_r' = 1 + \frac{\omega_p^2(\omega_0^2 - \omega^2)}{(\omega^2 - \omega_0^2)^2 + \gamma^2\omega^2} \tag{1.5}$$

$$\varepsilon_r'' = \frac{\omega_p^2\gamma\omega}{(\omega^2 - \omega_0^2)^2 + \gamma^2\omega^2} \tag{1.6}$$

The line shape of the imaginary (or absorption) term corresponds to a Lorentzian with a peak value at $\omega = \omega_0$. When the frequency is below the plasma frequency, the material has a negative permittivity, meaning that it has reflective optical properties. This effect can be additive and, therefore, a variety of complex phenomena can occur depending on the number of resonances in the material. For a material with a single resonant frequency: wavelengths far above (and greater

than ω_p) or far below (and less than ω_p) ω_0 will behave transparently, and near the resonant frequency will be absorptive. At the plasma frequency, the material's ε_r' changes sign from negative to positive for increasing frequency. For many optics applications we represent the permittivity in terms of a complex index of refraction: $\tilde{n} = n - ik$, where the relationship between the complex permittivity is:

$$\varepsilon_r' = n^2 - k^2 \tag{1.7}$$

$$\varepsilon_r'' = 2nk \tag{1.8}$$

A modification to the Lorentz model, called the Drude-Lorentz model, assumes that electrons in metals are unbound (*i.e.*, $\omega_0 = 0$) such that electrons behave as a free-electron gas:

$$\varepsilon_r = 1 - \frac{\omega_p^2}{\omega^2 - i\gamma\omega} \tag{1.9}$$

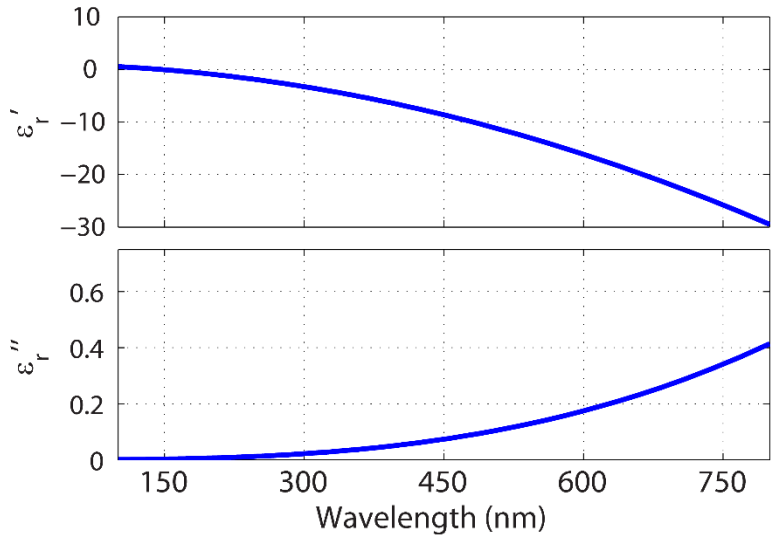

Figure 1.2. Real and imaginary permittivity functions of silver demonstrating that metals have negative real permittivities and small imaginary permittivities in the visible spectrum.

If we consider the real and imaginary components of the permittivity for silver ($\omega_p = 1.4 \times 10^{16}$ s^{-1} and $\gamma = 0.032 \times 10^{15}$ s^{-1}) using the Drude-Lorentz model,[27] we obtain Figure 1.2.

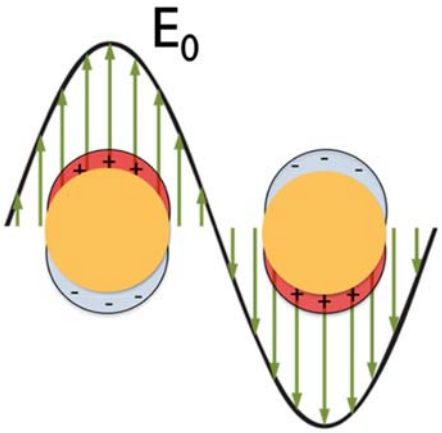

Figure 1.3. Metal nanoparticles exhibit a localized surface plasmon resonance (LSPR) in which free electrons coherently oscillate in response to an incident electric field. Light near the resonance frequency will be strongly absorbed by the nanoparticles.

Nanoparticles consisting of noble metals such as gold, silver, and copper exhibit an effect called the localized surface plasmon resonance (LSPR). As shown in Figure 1.3, the LSPR is described by a coherent oscillation of the free-electron gas that moves in response to an incident electric field. The Drude-Lorentz model describes the permittivity of these metals such that we can analytically calculate the LSPR for highly symmetric nanostructures. In particular, the polarizability α for a spherical nanostructure is described by the Clausius-Mossotti relation:[28]

$$\alpha(\omega) = \frac{\varepsilon_r(\omega) - \varepsilon_m}{\varepsilon_r(\omega) + 2\varepsilon_m} \tag{1.10}$$

Silver is a nearly ideal plasmonic material in which experimental optical measurements match the prediction produced by the Drude-Lorentz model well. Gold, on the other hand, does

not match as well because of effects such as interband transitions that occur at ultraviolet/blue frequencies; it is necessary to perform additional empirical fitting and modification to the Drude-Lorentz model in order to adequately match experimental measurements. The following is a modified Drude-Lorentz model appropriate for metals with interband transitions, like gold:[26]

$$\varepsilon_r = \varepsilon_\infty - \frac{\omega_p^2}{\omega^2 - i\gamma\omega} \tag{1.11}$$

where ε_∞ is a high-frequency permittivity constant. Researchers commonly use a combination of empirically derived fitting functions applied to the Drude-Lorentz model or experimentally measured optical constants of thin films of gold evaporated onto substrates.[26,29,30]

1.3 Light scattering

Long before the field of nanoscience was developed, early physicists such as James Clerk Maxwell, John Tyndall, and Lord Rayleigh studied the properties of light. In particular, Lord Rayleigh sought to understand the origin of the blue sky. As described by Milton Kerker, Rayleigh had argued that the blue sky was a consequence of light scattering because experiments demonstrated that skylight was polarized; and that polarization was caused by the scattering of light by small isotropic particles (or oscillating dipoles) with respect to the wavelength of light.[31] By the late 1800s, Rayleigh had arrived at the now well-known $1/\lambda^4$ dependence on the intensity of scattered light through dimensional analysis. This relationship is responsible for the blue sky because shorter wavelengths of light have greater scattering intensity and longer wavelengths have less scattering intensity, resulting in the appearance of a blue sky. Today, we refer to inelastic light scattering as Rayleigh scattering and mathematically describe its intensity *I* as the following (for perpendicularly polarized scattered light):[31]

$$I = \frac{16\pi^4 a^6}{r^2 \lambda^4} \left(\frac{n^2 - 1}{n^2 + 2} \right)^2 \tag{1.12}$$

where a is the size of the radius of the scatterer, λ is the wavelength of light, r is the observation distance, and n is the index of refraction of the scatterer.

Shortly after the formulation of Rayleigh scattering, a physicist named C. V. Raman identified a weak form of scattering or "secondary radiation".[32] Raman observed a shift in the color of light when a solution was illuminated with sunlight and transmitted through colored filters. Raman first published his results on secondary radiation in 1928 and quickly won the Nobel Prize in Physics in 1930 for the discovery of inelastic light scattering. In honor of Raman, we now call this phenomenon Raman scattering.

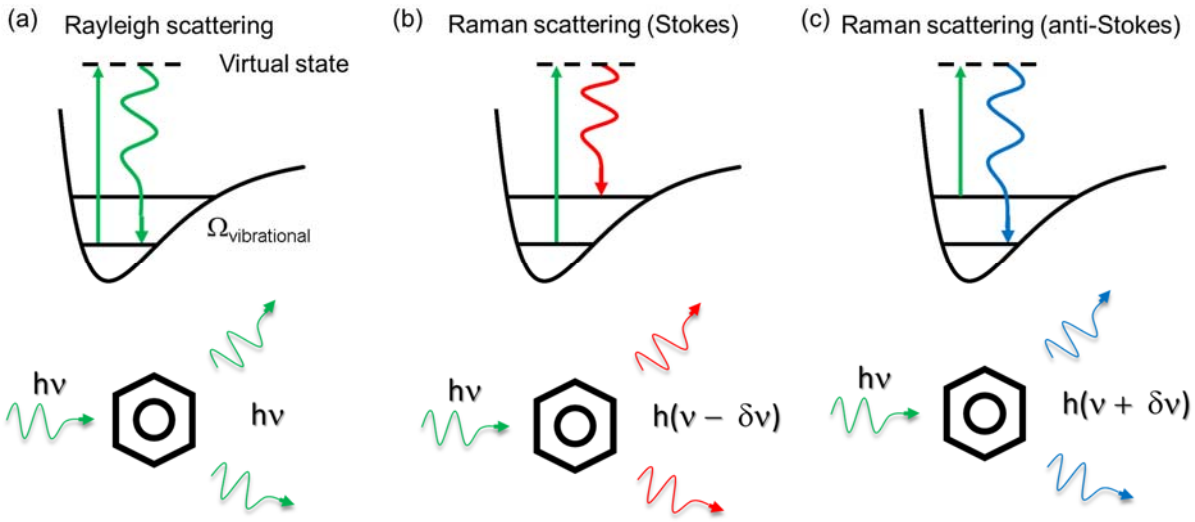

Figure 1.4. Illustration of (a) Rayleigh scattering, (b) Stokes-shifted Raman scattering, and (c) anti-Stokes shifted Raman scattering.

Rayleigh and Raman scattering are pictorially represented in Figure 1.4 using Jablonski diagrams. In Rayleigh scattering, a photon briefly (on the order of femtoseconds) excites a molecule to a virtual state and scatters a photon of the same energy. A virtual state is a short-

lived state that is not necessarily an eigenvalue of the wavefunction of the molecule; meaning that it does not satisfy selection rules for electronic transitions. Raman scattering is a form of inelastic light scattering in which a molecule in the ground state (or an excited vibrational state) scatters a photon with lesser (or greater) energy than the incident photon. This leads to a molecularly specific scattering process from which is it possible to identify (and multiplex) numerous molecule-metal probes, which is essential for rapidly identifying numerous biomarkers specific to a disease. For a vibrational mode of a molecule to be Raman-active, there must be a change in molecular polarizability under excitation:

$$\frac{\partial \alpha}{\partial q_i} \neq 0 \tag{1.13}$$

where q_i is a generalized coordinate for each mode.

As shown by C. V. Raman, observation of secondary radiation is a rare event, resulting in exceedingly weak signals. To some extent, improvements in instrumentation and optical devices such as lasers have mitigated these concerns; nonetheless, the Raman scattering cross section of most molecules is far below that of the fluorescence or absorption cross section. Raman scattering was a useful quantitative chemical analysis tool but did not reach its widespread popularity until the discovery of the surface-enhancement effect.

1.4 Surface-enhanced Raman spectroscopy (SERS)

In 1974 Martin Fleischmann and coworkers observed that a roughened silver electrode with adsorbed pyridine molecules produced an unexpectedly high Raman scattering signal.[33] At the time, the mechanism for this effect was not well understood and was simply attributed to a greater surface area as a result of surface roughening.[34] A few year later in 1977, Richard Van

Duyne and David Jeanmaire coined the term surface-enhanced Raman scattering (SERS). In their paper, they confirmed and explained the results observed by Fleischmann with an electromagnetic model.[35] Despite the potential applications of SERS, its popularity remained low until the late 1990s when two research groups discovered the capability of single-molecule SERS. In 1997, Shuming Nie and Steven Emory published a paper in *Science* describing single-molecule SERS using rhodamine 6G as a reporter molecule and aggregated silver nanoparticles dried on a silicon substrate.[36] The same year, Katrin Kneipp and coworkers published a report in *Physical Review Letters* demonstrating single-molecule SERS using the reporter molecule crystal violet and a solution of aggregated colloidal silver.[37] At the time, Nie calculated enhancement factors on the order of $10^{14} - 10^{15}$; similarly, Kneipp reported enhancement of 10^{14}. In order to support their theory of single-molecule SERS, both order-of-magnitude estimates were compared to fluorescence cross sections to demonstrate that SERS is as intense as single-molecule fluorescence. These calculations, however, have been shown to be incorrectly normalized to a non-resonant Raman mode (in the case of Kneipp's report) and incorrectly used a multiplier (in the case of Nie's report).[38,39] A more reasonable estimate that has been confirmed by simulation and experiments for single-molecule SERS is $10^{8} - 10^{10}$. Subsequent advances in nanotechnology and optical instrumentation around this time led to the explosion in popularity of SERS alongside these pioneering papers.

To this day, controversy surrounds the physical origin and mechanisms of SERS. The majority of researchers today accept that SERS is a consequence of two primary mechanisms.[39] The dominant and more easily explained mechanism is called electromagnetic enhancement. Electromagnetic enhancement is a simply a consequence of the antenna-like nature of plasmonic nanostructures or nano-featured surfaces. Acting as antennae, nanostructures concentrate

incident light by many orders of magnitude near their surface. Therefore, molecules placed near the surface will experience enhancement due to the relative intensity of the local electric field $\mathbf{E}_{loc}$ at both the incident frequency ω_0 (incoming light) and the Raman scattered frequency $\omega_0 \pm \omega_s$ (outgoing light). Electromagnetic enhancement *G* is a multiplicative factor consisting of the incident and scattered electric fields:[40]

$$G = \left|\mathbf{E}_{\text{loc}}(\omega_0)\right|^2 \left|\mathbf{E}_{\text{loc}}(\omega_0 \pm \omega_s)\right|^2 \tag{1.14}$$

The Stokes-shifted frequency is typically small ($\omega_s \approx 0$) and therefore we approximate the electromagnetic enhancement as:

$$G \approx \left|\mathbf{E}_{\text{loc}}(\omega_0)\right|^4 \tag{1.15}$$

It is possible to design nanostructures with excellent electromagnetic enhancement.[41,42] Nanostructures with sharp edges or corners exhibit several orders of magnitude higher enhancement factors in an analogous manner to a lightning rod where the electric field is strongly localized to areas of high radii of curvature.[43] It has been repeatedly shown that nanocubes have one of the highest electromagnetic enhancement factors of all reproducibly synthesizable nanostructures (consistent edge length, number of faces, etc.).[44,45] Aggregated nanoparticles have extremely high electromagnetic enhancement factors as a consequence of interplasmonic coupling between metallic surfaces forming so-called "hot-spots"; however, the reproducibility of aggregated nanoparticles is poor at best because it is difficult to precisely position molecules with surfaces.[46]

The second mechanism called the chemical enhancement effect is more elusive and has yet to be fully explained either experimentally or theoretically. Researchers generally argue that

chemical enhancement is due to a combination of metal-molecule resonances, charge transfer, and deformation in the polarizability of the bound molecule.[47] Because the chemical enhancement effect is relatively weak and it is unclear how to engineer nanoparticles and molecules to exploit it, researchers typically neglect its contribution and focus on electromagnetic enhancement.[39,46,47]

Undesirable or uncontrollable hot-spots are the greatest impediment to the development of SERS as an analytical technique. Researchers have shown that a silver nanoparticle lattice consisting of 1,000,000 sites with 63 hot-spots contributed a total of 24% of the measured enhancement to the SERS substrate.[48] Large contributions to the SERS signal such as these can completely dismantle the quantitative nature of SERS. If we are able to improve our control over the synthesis and fabrication of colloidal nanoparticles and plasmonic substrates, respectively, hot-spot formation may be minimized to a point that it is no longer a significant disadvantage.

1.5 Light propagation and enhancement

Consideration of the propagation of light through turbid media is crucial when dealing with colloidal nanoparticles. Colloidal SERS measurements exhibit an inner-filter effect or a competition between enhancement and extinction as light propagates through the volume of nanoparticles.[49–51] Absorption and enhancement are closely related, but do not overlap. The relationship between these two effects is not intuitive and requires careful calculations to elucidate the influence of one on the other.[52]

As shown in Figure 1.5, light propagating through a turbid media decays exponentially. SERS measurements performed on colloids mimic a tumor environment with a three-dimensional matrix of nanoparticles embedded within a volume. To study the inner-filter effect,

we combine the Beer-Lambert law with analytic calculations for the electromagnetic enhancement. The Beer-Lambert law may be described by the following:

$$A = \varepsilon bc \tag{1.16}$$

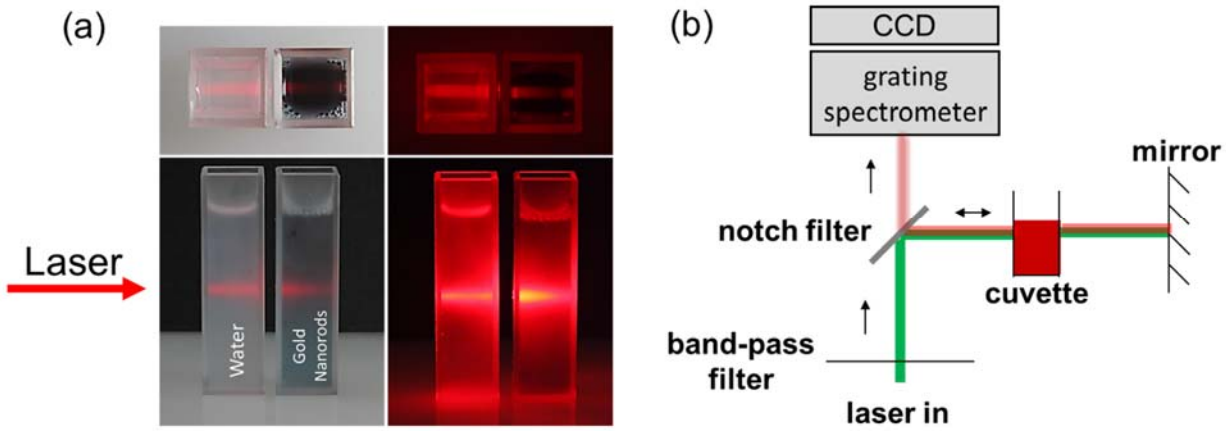

Figure 1.5. (a) Colloidal propagation model illustrating the propagation of laser light through a turbid (gold nanorod) and non-turbid media (water). As light propagates through the turbid media, it decays exponentially as described by the Beer-Lambert law. Image from reference [50]. (b) Experimental setup for measuring colloidal nanoparticle solutions and collection of Raman scattered light. The collimated laser beam illuminates the sample, is reflected passed through a holographic notch filter to remove Rayleigh scattered light, and then collected into a CCD spectrograph.

where A is the absorbance, ε is the extinction coefficient, b is the path length, and c is the concentration. All of these quantities may be measured or looked up in tables. Accordingly, the intensity of light I at an initial intensity I_0 decays exponentially according to the Beer-Lambert law: $A = \log_{10}(I / I_0) \leftrightarrow I / I_0 = e^{-\varepsilon bc}$. The extinction coefficient for plasmonic nanostructures is often calculated using analytical or numerical software. Fortunately, these calculations are straightforward and easy to perform; therefore, it is often possible to quantitatively make predictions based on the Beer-Lambert law. As we will discuss in Sections 1.6 and 1.7, electromagnetic enhancement may also be calculated using various analytical models or

numerical tools.

The intensity as a function of frequency is given by:[53,54]

$$I(\omega,\omega_0) = N\left|\chi\right|^2 G(\omega,\omega_0)\int_0^b dz e^{-zn_{\text{media}}c[\varepsilon(\omega)-\varepsilon(\omega_0)]} \tag{1.17}$$

where N is the number of molecules in the excitation volume, χ is the susceptibility of a Raman-active molecule, and n_{media} is the index of refraction of the surrounding solution. Figure 1.6 shows how closely related extinction and enhancement overlap. We have previously shown through both experimental measurements and theoretical models that excitation of

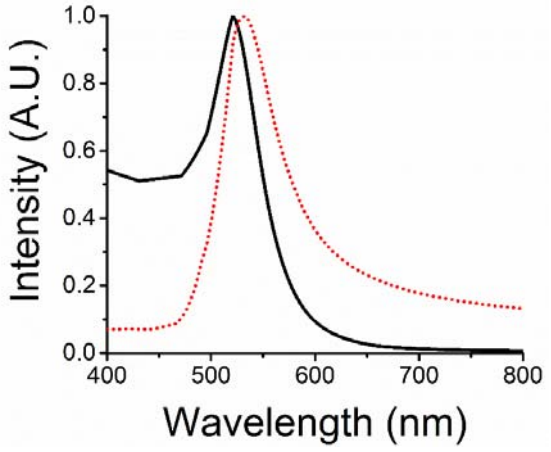

Figure 1.6. Calculated extinction (black, solid line) and electromagnetic enhancement (red, dotted line) of a 10 nm gold nanoparticle. Overlapping of extinction and enhancement require careful consideration of parameters such as excitation wavelength, path length, concentration, and choice of nanoparticle shape/size.

colloidal nanospheres with a laser wavelength of 532 nm will not yield a measurable signal because extinction dominates enhancement at this frequency.[49,50] At an appropriate concentration (*i.e.*, < 10 nM), measurements with 633 nm and 785 nm have been successful because enhancement dominates extinction. Anisotropic nanostructures have a tunable extinction cross section such that it is possible to design nanostructures for certain excitation wavelengths. For example, optimal SERS signal is obtained with LSPRs slightly blue-shifted from an excitation

wavelength of 785 nm.[50] Gold nanostructures have tunable optical properties based on their size and shape such that it is possible to perform SERS imaging with near-infrared light, which increases tissue penetration depth by decreasing optical absorption through the so-called "water-window".[20]

1.6 Analytical light scattering calculations

The optical properties of colloidal metals interested early scientists such as James Clerk Maxwell, Michael Faraday, and Gustav Mie. In 1908, Mie published an analytical solution to spherical scattering to explain the brilliant and unexpected reddish hue observed from colloidal gold.[55] Mie theory is an extremely powerful tool that has found extensive modern day usage because we can now fabricate a wide variety of nanospheres. Additionally, computers can now implement Mie's algorithms with little effort; Mie developed all of his original mathematics without the use of a computer. Briefly, Mie theory solves the Helmholtz equation:[28]

$$\nabla^2 \mathbf{E} + k^2 \mathbf{E} = 0 \tag{1.18}$$

where k is the wavevector. And Gauss's and Faraday's laws state (for a source-free system):

$$\nabla \cdot \mathbf{E} = 0 \tag{1.19}$$

$$\nabla \times \mathbf{E} = \mathrm{i}\omega\mu\mathbf{H} \tag{1.20}$$

Mie theory expands on these fundamental relations in terms of vector spherical harmonics **M** and **N**:

$$\mathbf{M} = \nabla \times (\mathbf{r}\psi) \tag{1.21}$$

$$\nabla \times \mathbf{N} = k\mathbf{M} \tag{1.22}$$

where **r** is the radius vector. For a function $\psi(r, \theta, \phi)$, in spherical coordinates, separation of

variables is used to solve Helmholtz's equation. The general solution is described elsewhere.[28,56] Applying boundary conditions for a spherical scatterer at the origin, scattering coefficients may be derived:[28]

$$a_n = \frac{m\psi_n(mx)\psi_n'(x) - \psi_n(x)\psi_n'(mx)}{m\psi_n(mx)\xi_n'(x) - \xi_n(x)\psi_n'(mx)} \tag{1.23}$$

$$b_n = \frac{\psi_n(mx)\psi_n'(x) - m\psi_n(x)\psi_n'(mx)}{\psi_n(mx)\xi_n'(x) - m\xi_n(x)\psi_n'(mx)} \tag{1.24}$$

From an experimental perspective far-field properties of spherical scatterers are far more useful than knowing the scattered electric field. Derived using the optical theorem, one can arrive at the scattering C_{sca} and extinction C_{ext} cross sections after some manipulation:[28]

$$C_{\text{sca}} = \frac{2\pi}{k^2}\sum_{n=1}^{\infty}(2n+1)(|a_n|^2 + |b_n|^2) \tag{1.25}$$

$$C_{\text{ext}} = \frac{2\pi}{k^2}\sum_{n=1}^{\infty}(2n+1)\,\text{Re}(a_n + b_n) \tag{1.26}$$

where *n* is the number of terms and *m* is the ratio of the refractive index of the scatterer and the external medium. Extinction is simply the sum of scattering and absorption contributions ($C_{\text{ext}} = C_{\text{sca}} + C_{\text{abs}}$).

In the case of most colloidal plasmonic nanomaterials, rigorous Mie theory is unnecessarily complicated and unneeded. The quasi-static approximation may be used if the assumption that a constant electric field over the nanostructure is valid. In other words, if the particle size is small with respect to the wavelength of the illumination light, then we may use the following to calculate the cross-sectional quantities:[28]

$$C_{\text{sca}} = \frac{8}{3} x^4 \left| \frac{m^2 - 1}{m^2 + 2} \right|^2 \tag{1.27}$$

$$C_{\text{ext}} = 4x \, \text{Im} \left\{ \frac{m^2 - 1}{m^2 + 2} \right\} \tag{1.28}$$

where $x = 2\pi n_{\text{media}} a / \lambda$ and a is the radius of the nanoparticle.

1.7 Numerical light scattering calculations

The immense popularity of plasmonic nanostructures has encouraged the development and extension of numerical electromagnetic computational tools and techniques to metallic nanostructures. With the continual improvement of computing systems in terms of clock speed and memory, it is now possible to calculate the near-field enhancement or far-field extinction properties of arbitrarily shaped nanostructures. A short, but incomplete, list of numerical techniques used in plasmonics calculations include the T-matrix method,[57] the discrete dipole approximation (DDA),[58,59] the finite element method (FEM),[42,60] the finite difference time domain (FDTD) method,[61,62] and the boundary element method (BEM).[63–66] Commercial products such as COMSOL Multiphysics for FEM and Lumerical for FDTD are now routinely used to calculate optical properties. The FEM and BEM methods are briefly discussed below, as they have been used throughout this dissertation.

The finite element method is a complex computational technique that makes it possible to numerically solve partial differential equations that would otherwise be intractable using analytical or quasi-analytical techniques. The mathematics behind FEM for two- and three-dimensional geometries is exceedingly complicated and is generally handled through the use of commercially developed software rather than manually writing FEM code. In the field of

plasmonics, one of the most popular software packages for solving numerical problems is called COMSOL Multiphysics. The theory behind FEM may be briefly summarized by the following linear operation:

$$\hat{A}x = B \tag{1.29}$$

where $\hat{A}$ is an operator acting on an unknown quantity of interest, x, and B corresponds to sources in the simulation space. In the weighted residual method of the FEM, x is expanded in terms of a set of basis functions v_j and expansion coefficients c_j:[56,67]

$$x = \sum_j c_j v_j \tag{1.30}$$

From here, it is necessary to use a weighting factor (commonly set to v_j) and integrate over the set of basis functions such that a system of linear equations is obtained:

$$S_{ij} = \int v_i \hat{A}(v_j) d\Omega \tag{1.31}$$

$$\sum_j S_{ij} c_j = \int v_j B \, d\Omega \tag{1.32}$$

where each equation is integrated over a domain Ω. The techniques for formulating these domains and solving the set of linear equations is exceedingly complex and beyond the scope of this dissertation. The major advantage of the FEM is its flexibility in terms of being able to solve any boundary value problem on arbitrary geometries. FEM is also well-suited for frequency-dependent material properties and non-cubic grids, unlike the FDTD method.[42]

In Figure 1.7(a), the finite element method was compared to the quasi-static approximation by calculating the extinction cross section C_{ext}. The two methods have excellent agreement, indicating that the simulation domain was appropriately designed for far-field calculations.

Furthermore, we show in Figure 1.7(b) that it is possible to calculate the near-field enhancement of plasmonic nanoparticles. While the case of a spheroid is analytically solvable, more complex geometries mandate numerical solutions.

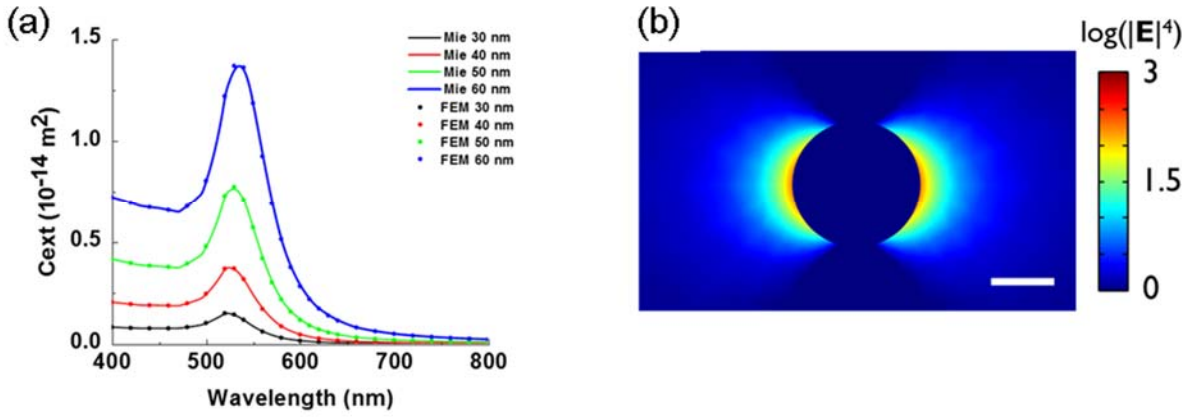

Figure 1.7. (a) A comparison of the finite element method (FEM) calculations using COMSOL Multiphysics and analytical Mie theory (quasi-static approximation) for gold nanospheres of varying diameter surrounded by water (n = 1.33). (b) Near-field $|\mathbf{E}|^4$ distribution of a gold nanosphere illuminated by 785 nm light.

Interested in simulating the electron energy loss spectra of arbitrarily shaped objects, F. J. García de Abajo formulated a technique for solving Maxwell's equations in inhomogeneous media derived from the boundary element method (BEM).[63] In the BEM, scalar and vector potentials are solved using surface integral equations with surface charges and currents, respectively. Starting from Maxwell's equations:[64,68]

$$\nabla \cdot \mathbf{B} = 0 \tag{1.33}$$

where **B** is the magnetic flux density. It follows from the properties of vector fields (*i.e.*, $\nabla \cdot (\nabla \times \mathbf{f}) = 0$ for any vector field **f**) that an arbitrary quantity called the magnetic vector potential **A** may then be defined and related to **B** by the following:

$$\mathbf{B} = \nabla \times \mathbf{A} \tag{1.34}$$

The electric field **E** is related to the scalar electric potential ϕ and **A** by:

$$\mathbf{E} = \mathrm{i}k\mathbf{A} - \nabla\phi \tag{1.35}$$

for an electrodynamic system. As a result of the arbitrary nature of **A**, it is possible to define its divergence as we see fit. For the so-called Lorentz gauge condition, the divergence of **A** is chosen to be (assuming non-magnetic materials):[64]

$$\nabla \cdot \mathbf{A} = \mathrm{i}k\varepsilon\phi \tag{1.36}$$

For instances where the permittivity ε is nonzero at interfaces such that the surface charge σ_j and surface current $\mathbf{h}_j$ are calculated as:[63,64]

$$\sigma_j = \frac{\varepsilon}{4\pi}\mathbf{E}_j \cdot \nabla\left(\frac{1}{\varepsilon_j}\right) \tag{1.37}$$

$$\mathbf{h}_j = -\frac{\mathrm{i}\omega\phi_j\nabla\varepsilon_j}{4\pi} \tag{1.38}$$

The surface integral equations for each j^{th} boundary of interface S_j are:

$$\phi(\mathbf{r}) = \phi_j^{ext}(\mathbf{r}) + \oint_{S_j} da\, G_j(\mathbf{r},\mathbf{s})\sigma_j(\mathbf{s}) \tag{1.39}$$

$$\mathbf{A}_j(\mathbf{r}) = \mathbf{A}_j^{ext}(\mathbf{r}) + \oint_{S_j} da\, G_j(\mathbf{r},\mathbf{s})\mathbf{h}_j(\mathbf{s}) \tag{1.40}$$

where the external scalar and vector potentials ϕ_j^{ext} and $\mathbf{A}_j^{ext}$ are caused by sources in the j^{th} boundary at position **r** and interface **s**. The point source response function (Green's function) is defined as:[68]

$$(\nabla^2 + k_j^2)G_j(\mathbf{r},\mathbf{r}') = -4\pi\delta(\mathbf{r}-\mathbf{r}') \tag{1.41}$$

$$G_j(\mathbf{r},\mathbf{r}') = \frac{e^{ik_j|\mathbf{r}-\mathbf{r}'|}}{|\mathbf{r}-\mathbf{r}'|} \tag{1.42}$$

The integral equations are solved by imposing interfacial boundary conditions for small element sizes. From these equations, it is possible to calculate the electric field throughout the simulation space. Ulrich Hohenester and Andreas Trügler developed a software package called metallic nanoparticle boundary element method (MNPBEM) in MATLAB. MNPBEM is a convenient and efficient package for calculating the optical properties of arbitrarily shaped plasmonic nanostructures in homogeneous media. MNPBEM has been used extensively in electron energy loss spectroscopy, optical far- and near-field calculations.[64–66]

Useful far- and near-field optical properties may be calculated once the electric field is known. The relationship for calculating the absorption cross section is derived using energy conservation and in three dimensions is given by:[69]

$$C_{\text{abs}} = nk_0 \int d^3r \, \text{Im}[\varepsilon(\mathbf{r})]\left|\mathbf{E}(\mathbf{r})\right|^2 \tag{1.43}$$

for a given electric field $\mathbf{E}_0$ propagating in a surrounding medium with index of refraction n, free-space wavevector k_0, and a nanostructure permittivity of ε. Similarly, the extinction cross section may be evaluated from the following:

$$C_{\text{ext}} = -nk_0 \, \text{Im}\left\{\int \text{d}^3\text{r}[\varepsilon(\mathbf{r})-1]\mathbf{E}(\mathbf{r})\cdot\mathbf{E}_{\text{inc}}^*(\mathbf{r})\right\} \tag{1.44}$$

where $\mathbf{E}_{\text{inc}}(\mathbf{r})$ is the incident electric field and $\mathbf{E}(\mathbf{r})$ is the scattered electric field.

1.8 Gold nanoparticle synthesis and characterization

Michael Faraday was the first modern-day scientist to synthesize and study colloidal gold. Faraday added phosphorous, acting as a reducing agent, to an aqueous solution of gold chloride.[70] Faraday's original colloids are still held and exhibited at the Royal Institute in London. In 1951, John Turkevich and coworkers systematically studied the nucleation and growth of gold nanoparticles using a variety of chemical reducing agents including a technique that utilized a boiling aqueous solution of gold chloride and sodium citrate. Sodium citrate acts as a reducing agent at elevated temperatures and as a stabilizer at room temperature.[71–73] While the monodispersity of Turkevich synthesized nanoparticles is not exceptional, this method is robust and heavily used even today for manufacturing spherical gold and silver nanoparticles. For simple systems such as the Turkevich method, the nucleation of gold nanoparticles may be described by the following:[74]

$$[AuCl_4]^- + 3e^- \rightleftharpoons Au^0 + 4Cl^- \tag{1.45}$$

Numerous anisotropic metallic nanostructures have been synthesized within the last decade. One of the most attractive features of anisotropic plasmonic nanostructures, is the ability to tune their near- and far-field optical properties throughout the visible and near-infrared spectrum. Gold nanorods, in particular, have been successful and have found heavy usage in SERS and plasmonic sensing applications. The synthesis of gold nanorods has its origins in electrochemistry where a porous alumina template was used to assist anisotropic growth during electrochemical reduction.[75] An aqueous seed-mediated wet chemical synthesis of gold nanorods originated in the early 2000s.[76,77] Before this time, electrochemically produced gold nanorods were relatively large and did not exhibit a strong dipolar LSPR.[25] In the aqueous synthesis of gold nanorods a surfactant called cetyltrimethylammonium bromide (CTAB) is used to help

direct anisotropic growth. The choice of surfactant is essential for growth; for example, similar surfactants such as cetyltrimethylammonium chloride and cetyltrimethylammonium iodide have not been successfully used to grow nanorods. The counterion, in this case, is essential to the growth mechanism because it can bind differently to certain crystalline facets. Short-aspect ratio gold nanorod growth is further complicated by the intentional addition of Ag^+ to help control the aspect ratio. Even though we have the ability to accurately predict and grow nanorods, the growth mechanism is still not fully understood; there are three dominant theories on how growth might occur but further investigation is needed.[75] Despite this, gold nanorods are heavily used due to their uniformity, ease of synthesis, improved near-field electric field intensity, and tunable far-field optical properties.

Table 1.1. A brief overview of common gold nanoparticle wet chemical synthesis techniques.

Shape	Reagents required	Size	Surface charge
Spheres[78]	CTAB, $HAuCl_4$, ascorbic acid, CTAB-stabilized seed	30 – 40 nm	Positive
Cubes[78,79]	CTAB, $HAuCl_4$, ascorbic acid, CTAB-stabilized seed	> 40 nm	Positive
Spheres[71,72]	Citrate, $HAuCl_4$	10 – 120 nm	Negative
Rods[76,77]	CTAB, $HAuCl_4$, $AgNO_3$, citrate-stabilized or CTAB-stabilized seed, ascorbic acid	12 nm wide, 15 – 100 nm long	Positive
Rods[80]	CTAB, $HAuCl_4$, $AgNO_3$, CTAB-stabilized seed, hydroquinone, NaOH	12 nm wide, 50 - 120 nm long	Positive
Stars[81,82]	$HAuCl_4$, HEPES buffer, NaOH	10 – 65 nm branches	Negative
Plates[83,84]	$HAuCl_4$, KI, CTAC, ascorbic acid, NaOH	45 – 120 nm	Positive
Au/Ag cages[85]	Ethylene glycol, $AgNO_3$, $HAuCl_4$, polyvinylpyrrolidone, Na_2S	45 – 100 nm	Neutral/Negative

A brief overview of several gold nanoparticle structures and the reagents needed to synthesize them is provided in Table 1.1. The ability to manufacture such a diverse group of

nanostructures from simple chemical reagents has helped this field garner a great deal of attention and interest. Depending on the application, certain geometries can be highly sought after for characteristics such as high enhancement factor, tunable LSPR, or a specific surface chemistry. A representative TEM image of CTAB-stabilized gold nanoparticles is shown in Figure 1.8. As shown, the monodispersity is reasonably high, however, small spheroidal nanoparticles and anisotropic nanoparticles are observed throughout deposited sample. Techniques such as oxidative etching and size-exclusion centrifugation have been developed to help eliminate these impurities.[83,84,86]

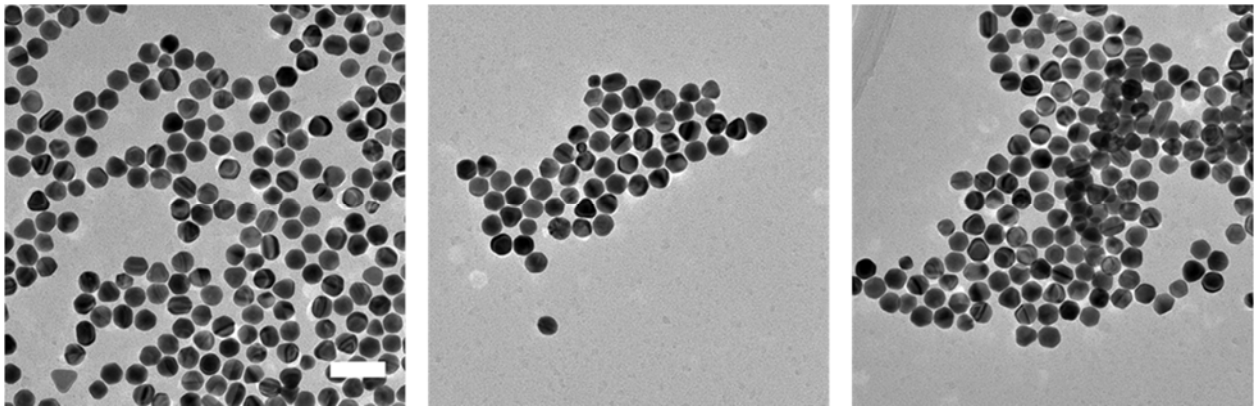

Figure 1.8. Representative transmission electron micrograph of CTAB-stabilized gold nanospheres. Scale bar: 100 nm.

The outlook for gold nanoparticle growth is positive with new high-yield synthetic procedures being developed each year. Continually improving the quality of nanostructures will improve the reliability of SERS-based measurements.

1.9 Recent applications of SERS

Numerous reports have demonstrated the utility of SERS nanoprobes for biological imaging and chemical sensing applications within recent years. As the field matures, researchers have been especially interested in developing SERS probes and substrates capable of quantitative

detection of analyte molecules. The ability to amplify the molecular signature more than one-million times is an extremely attractive feature that has helped maintain interest in SERS. With advances in optical instrumentation and nanofabrication techniques, SERS is on the cusp of becoming one of the foremost molecularly specific detection modalities.

Researchers first demonstrated *in vivo* usage of SERS nanoprobes by injecting the probes into the bloodstream of mice models from which the probes with conjugated antibodies were shown to collect in the tumor mass and detected using Raman spectroscopy.[22] More recently, multimodal magnetic-SERS-photoacoustic nanoparticles were used to help determine tumor margins of glioblastoma in mice models; brain tissue sections were carefully resected until the probe signal could no longer be detected.[87,88] This technique is rapid and allows the surgeon to quickly make decisions about how much tissue to remove and could be vital for saving patients.

In terms of biological imaging, a great deal of work must be accomplished before we are likely to see the usage of plasmonic nanostructures used for both *in vitro* and *in vivo* systems. In terms of *in vitro* imaging, the concern for toxicity and the ultimate fate of the nanoparticle is not a hindrance; however, for *in vivo* systems, researchers have to complete additional work demonstrating that the long-term fate of nanoparticles and its interaction with the organs such as the liver and kidneys will not cause damage.[17,18,21,24] Many of these problems apply to other types of nanomaterials such as quantum dots. Not only are semiconductor quantum dots composed of hazardous heavy metals but they also are so small that they have generally been regarded as being toxic to many biological systems. Nonetheless, the effects of gold nanoparticles in biological systems is not limited to toxicity but also physiological processes such as cell metabolism.[89]

SERS has found extensive usage in chemical sensing. Researchers have used SERS to investigate the pigments and structure of paintings using nondestructive SERS probes to gain historical insight.[90] A technique called shell-isolated nanoparticle-enhanced Raman spectroscopy (SHINERS)[91] was developed to demonstrate the ability of SERS to detect pesticides on fruit. Multilayered structures consisting of metal-dielectric layers have also been developed and shown to yield excellent sensitivities.[41,92] Year after year researchers continually refine the wet chemical synthesis and self-assembly of nanostructures such that improved chemical sensing is possible. For example, highly symmetric gold nanostars were demonstrated to have a consistent number of peaks and edge lengths.[93] In terms of self-assembly, researchers have demonstrated up to millimeter scale superlattices produced from aqueous solutions of nanoparticles.[94]

In order to better design SERS nanostructures, researchers have been trying to accurately model the optical properties of nanogap structures using nonlocal dielectric functions. Nonlocal dielectric functions are spatially varying functions that attempt to take into account effects such as quantum tunneling that could occur in nanostructures that have fused or are separated by a small distance.[95–98] Taking into account nonlinear effects in plasmonic nanostructures remains a challenging prospect, however. Many of these challenges arise from our treatment of nanostructures as classical or semi-classical entities using electrodynamic theory. To properly model these nanostructures, one must consider the quantum mechanics and use numerical techniques such as density functional theory.[39,99]

Ultimately, the promise of gold nanoparticles, plasmonics, and highly sensitive chemical sensing using SERS is promising but there remains a great deal of work from both the materials, optical, and chemistry side as well as biological concerns that all need to be addressed before nanoparticles will fully develop for commercial or medical usage.

1.10 Dissertation overview

In this dissertation, the rational design, synthesis, characterization, and application of SERS nanoparticles to biological imaging and chemical sensing will be discussed. SERS is an extremely popular and multidisciplinary field because of its potential as an emerging analytical technique for highly sensitive molecular detection. Scientists, engineers, and physicians have all worked on a wide variety of topics that fundamentally harness the surface-enhancement effect. This dissertation highlights many of the multidisciplinary aspects of SERS by combining computation, experimental design, nanomaterial synthesis, and spectroscopic imaging. As already discussed, Chapter 1 is a brief overview of the current state of the art in the field and contains background theory about the origins of SERS and plasmonic nanoparticles.

In Chapter 2, we will discuss a computational study investigating the optical properties of silver nanowires coated with varying degrees of silica. We found that patchy silica versus a uniform layer of silica can significantly alter the far-field and near-field optical properties of nanowires. Two main contributors to this effect are distortion of the localized electric field as a result of a change in the dielectric medium surrounding the nanowire and the relative positioning of the grown silica. There remain numerous challenges to precise positioning of silica clusters on the surface of nanowires; however, it has been previously experimentally shown that it is possible to grow a patchy layer of silica rather than a uniform layer in the solution phase.

Chapter 3 describes a crucial study in the stability of optical probes. For the first time, we investigated the stability of electrostatically bound Raman-active reporter molecules for colloidal solutions of nanoparticles encapsulated in polyelectrolyte layers. A combined electromagnetic and diffusion model was designed to explain the observation of loss of signal over a period of approximately one month. This study illustrates the importance of characterizing the long-term

stability of optical probes. Especially for *in vivo* studies, the stability of the Raman-active reporter molecules is essential; loss of signal could be misinterpreted as a loss of nanoparticles whereas, in this case, the nanoparticles are simply losing the Raman-active reporter molecules to diffusion. Alternative encapsulation methods are discussed and demonstrated to yield significant improvements in stability.

Chapter 4 is a similar study that investigates the preparation and kinetics of ligand exchange on the surface of gold nanoparticles. To date, few investigators have studied the kinetics of ligand exchange on the surface of gold nanoparticles, opting instead to study the kinetics and surface characterization of macroscopic substrates. In this chapter, we demonstrate that the ligand exchange kinetics of aromatic molecules with thiolated functional groups follow a first-order Langmuir adsorption model. Furthermore, the time-dependent spectral features of our colloidal samples provide an ensemble-averaged view of the structural and binding properties of the exchanged molecules. We also argue, in the case of certain ligands, that is it possible to simultaneously monitor the desorption and adsorption of the exchanging ligands. Overall, this study provides a broad overview of how to quickly manufacture and characterize the surface chemistry of optical probes.

Chapter 5 discusses the characterization of peptide-conjugated gold nanoparticles used to target and image the nucleus of cultured breast cells. Raman and infrared microspectroscopy were used to image the samples. The SERS enhancement of these nanoparticles was quite strong and made it easy to image them. The IR spectra of the nanoparticles was heavily obscured by the biological chemical signature of the cells such that is was not possible to directly localize these nanoparticles after they had been endocytosed and collected near the nucleus. The surface chemistry of the nanoparticles was also characterized to confirm the presence of the conjugated

peptide and other surface ligands. Numerical simulations in the mid-infrared were performed to further understand light interaction of small probes.

Chapter 6 is a theoretical investigation of substrate in the mid-infrared. Originating from the experimental study in Chapter 5, we sought to better understand how reflective substrates could influence the resulting mid-infrared spectra. Our simulated results indicate that there are significant spectral differences under certain illumination conditions for gold-coated and low-emissivity glass substrates. Using a theoretical absorber consisting of a series of Lorentzian bands, we show that the absorber thickness, angle of incidence, and type of reflective substrate can all influence the simulated data.

Chapter 7 demonstrates nanoarea electron diffraction of core-shell Au@Ag nanorods. Using both nanoarea electron diffraction and high angle aperture dark-field scanning transmission electron microscopy (HAADF-STEM), we demonstrate that certain long-aspect ratio gold nanorods have internalized twisting and bending. This bending effect is observed as diffraction spot splitting. Interestingly, we observed that the growth of a silver shell on gold nanorods relieves the internal bending and results in relatively sharp facets. This chapter demonstrates the importance of nanoarea electron diffraction as a structural characterization tool for nanostructures.

1.11 References

(1) Ferrari, M. Cancer Nanotechnology: Opportunities and Challenges. *Nat. Rev. Cancer* **2005**, *5*, 161–171.

(2) Freestone, I.; Meeks, N.; Sax, M.; Higgitt, C. The Lycurgus Cup – A Roman Nanotechnology. *Gold Bull.* **2007**, *40*, 270–277.

(3) Cui, Y.; Phang, I. Y.; Hegde, R. S.; Lee, Y. H.; Ling, X. Y. Plasmonic Silver Nanowire Structures for Two-Dimensional Multiple-Digit Molecular Data Storage Application. *ACS Photonics* **2014**, *1*, 631–637.

(4) Goh, X. M.; Zheng, Y.; Tan, S. J.; Zhang, L.; Kumar, K.; Qiu, C.-W.; Yang, J. K. W. Three-Dimensional Plasmonic Stereoscopic Prints in Full Colour. *Nat. Commun.* **2014**, *5*.
(5) Tan, S. J.; Zhang, L.; Zhu, D.; Goh, X. M.; Wang, Y. M.; Kumar, K.; Qiu, C.-W.; Yang, J. K. W. Plasmonic Color Palettes for Photorealistic Printing with Aluminum Nanostructures. *Nano Lett.* **2014**, *14*, 4023–4029.
(6) Huang, Y.-W.; Chen, W. T.; Tsai, W.-Y.; Wu, P. C.; Wang, C.-M.; Sun, G.; Tsai, D. P. Aluminum Plasmonic Multicolor Meta-Hologram. *Nano Lett.* **2015**, *15*, 3122–3127.
(7) Park, H. I.; Lee, S.; Lee, J. M.; Nam, S. A.; Jeon, T.; Han, S. W.; Kim, S. O. High Performance Organic Photovoltaics with Plasmonic-Coupled Metal Nanoparticle Clusters. *ACS Nano* **2014**, *8*, 10305–10312.
(8) Mubeen, S.; Lee, J.; Lee, W.; Singh, N.; Stucky, G. D.; Moskovits, M. On the Plasmonic Photovoltaic. *ACS Nano* **2014**, *8*, 6066–6073.
(9) Zhou, W.; Gao, X.; Liu, D.; Chen, X. Gold Nanoparticles for in Vitro Diagnostics. *Chem. Rev.* **2015**.
(10) Vo-Dinh, T.; Liu, Y.; Fales, A. M.; Ngo, H.; Wang, H.-N.; Register, J. K.; Yuan, H.; Norton, S. J.; Griffin, G. D. SERS Nanosensors and Nanoreporters: Golden Opportunities in Biomedical Applications. *Wiley Interdiscip. Rev. Nanomed. Nanobiotechnol.* **2015**, *7*, 17–33.
(11) Kim, T.; Zhou, R.; Mir, M.; Babacan, S. D.; Carney, P. S.; Goddard, L. L.; Popescu, G. White-Light Diffraction Tomography of Unlabelled Live Cells. *Nat. Photonics* **2014**, *8*, 256–263.
(12) Saar, B. G.; Freudiger, C. W.; Reichman, J.; Stanley, C. M.; Holtom, G. R.; Xie, X. S. Video-Rate Molecular Imaging in Vivo with Stimulated Raman Scattering. *Science* **2010**, *330*, 1368–1370.
(13) Pezacki, J. P.; Blake, J. A.; Danielson, D. C.; Kennedy, D. C.; Lyn, R. K.; Singaravelu, R. Chemical Contrast for Imaging Living Systems: Molecular Vibrations Drive CARS Microscopy. *Nat. Chem. Biol.* **2011**, *7*, 137–145.
(14) Fernandez, D. C.; Bhargava, R.; Hewitt, S. M.; Levin, I. W. Infrared Spectroscopic Imaging for Histopathologic Recognition. *Nat. Biotechnol.* **2005**, *23*, 469–474.
(15) Mahou, P.; Zimmerley, M.; Loulier, K.; Matho, K. S.; Labroille, G.; Morin, X.; Supatto, W.; Livet, J.; Debarre, D.; Beaurepaire, E. Multicolor Two-Photon Tissue Imaging by Wavelength Mixing. *Nat. Methods* **2012**, *9*, 815–818.
(16) van de Linde, S.; Heilemann, M.; Sauer, M. Live-Cell Super-Resolution Imaging with Synthetic Fluorophores. *Annu. Rev. Phys. Chem.* **2012**, *63*, 519–540.
(17) Derfus, A. M.; Chan, W. C. W.; Bhatia, S. N. Probing the Cytotoxicity of Semiconductor Quantum Dots. *Nano Lett.* **2004**, *4*, 11–18.
(18) Hauck, T. S.; Anderson, R. E.; Fischer, H. C.; Newbigging, S.; Chan, W. C. W. In Vivo Quantum-Dot Toxicity Assessment. *Small* **2010**, *6*, 138–144.
(19) Chan, W. C. .; Maxwell, D. J.; Gao, X.; Bailey, R. E.; Han, M.; Nie, S. Luminescent Quantum Dots for Multiplexed Biological Detection and Imaging. *Curr. Opin. Biotechnol.* **2002**, *13*, 40–46.
(20) Richards-Kortum, R.; Sevick-Muraca, E. Quantitative Optical Spectroscopy for Tissue Diagnosis. *Annu. Rev. Phys. Chem.* **1996**, *47*, 555–606.
(21) Chou, L. Y. T.; Chan, W. C. W. Nanotoxicology: No Signs of Illness. *Nat. Nanotechnol.* **2012**, *7*, 416–417.

(22) Qian, X.; Peng, X.-H.; Ansari, D. O.; Yin-Goen, Q.; Chen, G. Z.; Shin, D. M.; Yang, L.; Young, A. N.; Wang, M. D.; Nie, S. In Vivo Tumor Targeting and Spectroscopic Detection with Surface-Enhanced Raman Nanoparticle Tags. *Nat. Biotech.* **2008**, *26*, 83–90.
(23) Thakor, A. S.; Jokerst, J.; Zavaleta, C.; Massoud, T. F.; Gambhir, S. S. Gold Nanoparticles: A Revival in Precious Metal Administration to Patients. *Nano Lett.* **2011**, *11*, 4029–4036.
(24) Lewinski, N.; Colvin, V.; Drezek, R. Cytotoxicity of Nanoparticles. *Small* **2008**, *4*, 26–49.
(25) Dreaden, E. C.; Alkilany, A. M.; Huang, X.; Murphy, C. J.; El-Sayed, M. A. The Golden Age: Gold Nanoparticles for Biomedicine. *Chem. Soc. Rev.* **2012**, *41*, 2740–2779.
(26) Maier, S. A. *Plasmonics: Fundamentals and Applications*; Springer, 2007.
(27) Cai, W.; Shalaev, V. *Optical Metamaterials: Fundamentals and Applications*; Springer: New York, 2009.
(28) Bohren, C. F.; Huffman, D. R. *Absorption and Scattering of Light by Small Particles*; Wiley, 2007.
(29) Palik, E. D. *Handbook of Optical Constants of Solids*; Academic Press, 1998.
(30) Johnson, P. B.; Christy, R. W. Optical Constants of the Noble Metals. *Phys. Rev. B* **1972**, *6*, 4370–4379.
(31) Kerker, M. *The Scattering of Light and Other Electromagnetic Radiation*; Academic Press, 1969.
(32) Raman, C. V.; Krishnan, K. S. A New Type of Secondary Radiation. *Nature* **1928**, *121*, 501.
(33) Fleischmann, M.; Hendra, P. J.; McQuillan, A. J. Raman Spectra of Pyridine Adsorbed at a Silver Electrode. *Chem. Phys. Lett.* **1974**, *26*, 163–166.
(34) McQuillan, A. J. The Discovery of Surface-Enhanced Raman Scattering. *Notes Rec. R. Soc.* **2009**, *63*, 105–109.
(35) Jeanmaire, D. L.; Van Duyne, R. P. Surface Raman Spectroelectrochemistry: Part I. Heterocyclic, Aromatic, and Aliphatic Amines Adsorbed on the Anodized Silver Electrode. *J. Electroanal. Chem. Interfacial Electrochem.* **1977**, *84*, 1–20.
(36) Nie, S.; Emory, S. R. Probing Single Molecules and Single Nanoparticles by Surface-Enhanced Raman Scattering. *Science* **1997**, *275*, 1102–1106.
(37) Kneipp, K.; Wang, Y.; Kneipp, H.; Perelman, L. T.; Itzkan, I.; Dasari, R. R.; Feld, M. S. Single Molecule Detection Using Surface-Enhanced Raman Scattering (SERS). *Phys. Rev. Lett.* **1997**, *78*, 1667–1670.
(38) Le Ru, E. C.; Etchegoin, P. G. Quantifying SERS Enhancements. *MRS Bull.* **2013**, *38*, 631–640.
(39) Moskovits, M. Persistent Misconceptions Regarding SERS. *Phys. Chem. Chem. Phys.* **2013**, *15*, 5301–5311.
(40) Schatz, G. C.; Van Duyne, R. P. *Electromagnetic Mechanism of Surface-Enhanced Spectroscopy*; Wiley, 2002; Volume 1 Theory and Instrumentation.
(41) Kodali, A. K.; Llora, X.; Bhargava, R. Optimally Designed Nanolayered Metal-Dielectric Particles as Probes for Massively Multiplexed and Ultrasensitive Molecular Assays. *Proc. Natl. Acad. Sci.* **2010**, *107*, 13620–13625.
(42) McMahon, J. M.; Henry, A.-I.; Wustholz, K. L.; Natan, M. J.; Freeman, R. G.; Duyne, R. P. V.; Schatz, G. C. Gold Nanoparticle Dimer Plasmonics: Finite Element Method Calculations of the Electromagnetic Enhancement to Surface-Enhanced Raman Spectroscopy. *Anal. Bioanal. Chem.* **2009**, *394*, 1819–1825.

(43) Liao, P. F.; Wokaun, A. Lightning Rod Effect in Surface Enhanced Raman Scattering. *J. Chem. Phys.* **1982**, *76*, 751–752.
(44) Sivapalan, S. T.; DeVetter, B. M.; Yang, T. K.; Schulmerich, M. V.; Bhargava, R.; Murphy, C. J. Surface-Enhanced Raman Spectroscopy of Polyelectrolyte-Wrapped Gold Nanoparticles in Colloidal Suspension. *J. Phys. Chem. C* **2013**, *117*, 10677–10682.
(45) Rycenga, M.; Kim, M. H.; Camargo, P. H. C.; Cobley, C.; Li, Z.-Y.; Xia, Y. Surface-Enhanced Raman Scattering: Comparison of Three Different Molecules on Single-Crystal Nanocubes and Nanospheres of Silver †. *J. Phys. Chem. A* **2009**, *113*, 3932–3939.
(46) Xu, H.; Aizpurua, J.; Käll, M.; Apell, P. Electromagnetic Contributions to Single-Molecule Sensitivity in Surface-Enhanced Raman Scattering. *Phys. Rev. E* **2000**, *62*, 4318–4324.
(47) Valley, N.; Greeneltch, N.; Van Duyne, R. P.; Schatz, G. C. A Look at the Origin and Magnitude of the Chemical Contribution to the Enhancement Mechanism of Surface-Enhanced Raman Spectroscopy (SERS): Theory and Experiment. *J. Phys. Chem. Lett.* **2013**, *4*, 2599–2604.
(48) Fang, Y.; Seong, N.-H.; Dlott, D. D. Measurement of the Distribution of Site Enhancements in Surface-Enhanced Raman Scattering. *Science* **2008**, *321*, 388–392.
(49) van Dijk, T.; Sivapalan, S. T.; DeVetter, B. M.; Yang, T. K.; Schulmerich, M. V.; Murphy, C. J.; Bhargava, R.; Carney, P. S. Competition between Extinction and Enhancement in Surface-Enhanced Raman Spectroscopy. *J. Phys. Chem. Lett.* **2013**, *4*, 1193–1196.
(50) Sivapalan, S. T.; Devetter, B. M.; Yang, T. K.; van Dijk, T.; Schulmerich, M. V.; Carney, P. S.; Bhargava, R.; Murphy, C. J. Off-Resonance Surface-Enhanced Raman Spectroscopy from Gold Nanorod Suspensions as a Function of Aspect Ratio: Not What We Thought. *ACS Nano* **2013**, *7*, 2099–2105.
(51) Tan, T.; Tian, C.; Ren, Z.; Yang, J.; Chen, Y.; Sun, L.; Li, Z.; Wu, A.; Yin, J.; Fu, H. LSPR-Dependent SERS Performance of Silver Nanoplates with Highly Stable and Broad Tunable LSPRs Prepared through an Improved Seed-Mediated Strategy. *Phys. Chem. Chem. Phys.* **2013**, *15*, 21034.
(52) Le Ru, E. C.; Galloway, C.; Etchegoin, P. G. On the Connection between Optical Absorption/extinction and SERS Enhancements. *Phys. Chem. Chem. Phys.* **2006**, *8*, 3083.
(53) Shriver, D. F.; Dunn, J. B. R. The Backscattering Geometry for Raman Spectroscopy of Colored Materials. *Appl. Spectrosc.* **1974**, *28*, 319–323.
(54) DeVetter, B. M.; Mukherjee, P.; Murphy, C. J.; Bhargava, R. Measuring Binding Kinetics of Aromatic Thiolated Molecules with Nanoparticles *via* Surface-Enhanced Raman Spectroscopy. *Nanoscale* **2015**, *7*, 8766–8775.
(55) Mie, G. Beiträge Zur Optik Trüber Medien, Speziell Kolloidaler Metallösungen. *Ann. Phys.* **1908**, *330*, 377–445.
(56) Jin, J.-M. *Theory and Computation of Electromagnetic Fields*; Wiley, 2010.
(57) Khlebtsov, N. G. T-Matrix Method in Plasmonics: An Overview. *J. Quant. Spectrosc. Radiat. Transf.* **2013**, *123*, 184–217.
(58) Draine, B. T.; Flatau, P. J. Discrete-Dipole Approximation for Scattering Calculations. *J. Opt. Soc. Am. A* **1994**, *11*, 1491.
(59) Flatau, P. J.; Draine, B. T. Fast Near Field Calculations in the Discrete Dipole Approximation for Regular Rectilinear Grids. *Opt. Express* **2012**, *20*, 1247–1252.
(60) Khoury, C. G.; Norton, S. J.; Vo-Dinh, T. Plasmonics of 3-D Nanoshell Dimers Using Multipole Expansion and Finite Element Method. *ACS Nano* **2009**, *3*, 2776–2788.

(61) Lesina, A. C.; Vaccari, A.; Berini, P.; Ramunno, L. On the Convergence and Accuracy of the FDTD Method for Nanoplasmonics. *Opt. Express* **2015**, *23*, 10481.
(62) Atkinson, A. L.; McMahon, J. M.; Schatz, G. C. FDTD Studies of Metallic Nanoparticle Systems. In *Self Organization of Molecular Systems*; Russo, N.; Antonchenko, V. Y.; Kryachko, E. S., Eds.; Springer Netherlands: Dordrecht, 2009; pp. 11–32.
(63) García de Abajo, F. J.; Howie, A. Retarded Field Calculation of Electron Energy Loss in Inhomogeneous Dielectrics. *Phys. Rev. B* **2002**, *65*, 115418.
(64) Hohenester, U.; Trügler, A. MNPBEM – A Matlab Toolbox for the Simulation of Plasmonic Nanoparticles. *Comput. Phys. Commun.* **2012**, *183*, 370–381.
(65) Hohenester, U. Simulating Electron Energy Loss Spectroscopy with the MNPBEM Toolbox. *Comput. Phys. Commun.* **2014**, *185*, 1177–1187.
(66) Waxenegger, J.; Trügler, A.; Hohenester, U. Plasmonics Simulations with the MNPBEM Toolbox: Consideration of Substrates and Layer Structures. *Comput. Phys. Commun.* **2015**, *193*, 138–150.
(67) Jin, J. *The Finite Element Method in Electromagnetics*; 3rd ed.; Wiley-IEEE: New York, 2014.
(68) Jackson, J. D. *Classical Electrodynamics*; 3rd ed.; Wiley, 1998.
(69) Hage, J. I.; Greenberg, J. M.; Wang, R. T. Scattering from Arbitrarily Shaped Particles: Theory and Experiment. *Appl. Opt.* **1991**, *30*, 1141–1152.
(70) Faraday, M. The Bakerian Lecture: Experimental Relations of Gold (and Other Metals) to Light. *Philos. Trans. R. Soc. Lond.* **1857**, *147*, 145–181.
(71) Turkevich, J.; Stevenson, P. C.; Hillier, J. A Study of the Nucleation and Growth Processes in the Synthesis of Colloidal Gold. *Discuss. Faraday Soc.* **1951**, *11*, 55–75.
(72) Kimling, J.; Maier, M.; Okenve, B.; Kotaidis, V.; Ballot, H.; Plech, A. Turkevich Method for Gold Nanoparticle Synthesis Revisited. *J. Phys. Chem. B* **2006**, *110*, 15700–15707.
(73) Schulz, F.; Homolka, T.; Bastús, N. G.; Puntes, V.; Weller, H.; Vossmeyer, T. Little Adjustments Significantly Improve the Turkevich Synthesis of Gold Nanoparticles. *Langmuir* **2014**, *30*, 10779–10784.
(74) Engelbrekt, C.; Jensen, P. S.; Sørensen, K. H.; Ulstrup, J.; Zhang, J. Complexity of Gold Nanoparticle Formation Disclosed by Dynamics Study. *J. Phys. Chem. C* **2013**, *117*, 11818–11828.
(75) Lohse, S. E.; Murphy, C. J. The Quest for Shape Control: A History of Gold Nanorod Synthesis. *Chem. Mater.* **2013**, *25*, 1250–1261.
(76) Jana, N. R.; Gearheart, L.; Murphy, C. J. Wet Chemical Synthesis of High Aspect Ratio Cylindrical Gold Nanorods. *J. Phys. Chem. B* **2001**, *105*, 4065–4067.
(77) Nikoobakht, B.; El-Sayed, M. A. Evidence for Bilayer Assembly of Cationic Surfactants on the Surface of Gold Nanorods. *Langmuir* **2001**, *17*, 6368–6374.
(78) Sau, T. K.; Murphy, C. J. Room Temperature, High-Yield Synthesis of Multiple Shapes of Gold Nanoparticles in Aqueous Solution. *J. Am. Chem. Soc.* **2004**, *126*, 8648–8649.
(79) Wu, X.; Ming, T.; Wang, X.; Wang, P.; Wang, J.; Chen, J. High-Photoluminescence-Yield Gold Nanocubes: For Cell Imaging and Photothermal Therapy. *ACS Nano* **2009**, *4*, 113–120.
(80) Vigderman, L.; Zubarev, E. R. High-Yield Synthesis of Gold Nanorods with Longitudinal SPR Peak Greater than 1200 Nm Using Hydroquinone as a Reducing Agent. *Chem. Mater.* **2013**, *25*, 1450–1457.

(81) Dam, D. H. M.; Culver, K. S. B.; Odom, T. W. Grafting Aptamers onto Gold Nanostars Increases *in Vitro* Efficacy in a Wide Range of Cancer Cell Types. *Mol. Pharm.* **2014**, *11*, 580–587.
(82) Xie, J.; Lee, J. Y.; Wang, D. I. C. Seedless, Surfactantless, High-Yield Synthesis of Branched Gold Nanocrystals in HEPES Buffer Solution. *Chem. Mater.* **2007**, *19*, 2823–2830.
(83) Chen, L.; Ji, F.; Xu, Y.; He, L.; Mi, Y.; Bao, F.; Sun, B.; Zhang, X.; Zhang, Q. High-Yield Seedless Synthesis of Triangular Gold Nanoplates through Oxidative Etching. *Nano Lett.* **2014**, *14*, 7201–7206.
(84) O'Brien, M. N.; Jones, M. R.; Brown, K. A.; Mirkin, C. A. Universal Noble Metal Nanoparticle Seeds Realized Through Iterative Reductive Growth and Oxidative Dissolution Reactions. *J. Am. Chem. Soc.* **2014**, *136*, 7603–7606.
(85) Skrabalak, S. E.; Au, L.; Li, X.; Xia, Y. Facile Synthesis of Ag Nanocubes and Au Nanocages. *Nat. Protoc.* **2007**, *2*, 2182–2190.
(86) Steinigeweg, D.; Schütz, M.; Salehi, M.; Schlücker, S. Fast and Cost-Effective Purification of Gold Nanoparticles in the 20–250 Nm Size Range by Continuous Density Gradient Centrifugation. *Small* **2011**, *7*, 2443–2448.
(87) Kircher, M. F.; Zerda, A. de la; Jokerst, J. V.; Zavaleta, C. L.; Kempen, P. J.; Mittra, E.; Pitter, K.; Huang, R.; Campos, C.; Habte, F.; *et al.* A Brain Tumor Molecular Imaging Strategy Using a New Triple-Modality MRI-Photoacoustic-Raman Nanoparticle. *Nat. Med.* **2012**, *18*, 829–834.
(88) Karabeber, H.; Huang, R.; Iacono, P.; Samii, J. M.; Pitter, K.; Holland, E. C.; Kircher, M. F. Guiding Brain Tumor Resection Using Surface-Enhanced Raman Scattering Nanoparticles and a Hand-Held Raman Scanner. *ACS Nano* **2014**, *8*, 9755–9766.
(89) Chen, N.; Wang, H.; Huang, Q.; Li, J.; Yan, J.; He, D.; Fan, C.; Song, H. Long-Term Effects of Nanoparticles on Nutrition and Metabolism. *Small* **2014**, *10*, 3603–3611.
(90) Frano, K. A.; Mayhew, H. E.; Svoboda, S. A.; Wustholz, K. L. Combined SERS and Raman Analysis for the Identification of Red Pigments in Cross Sections from Historic Oil Paintings. *Analyst* **2014**, *139*, 6450–6455.
(91) Li, J. F.; Huang, Y. F.; Ding, Y.; Yang, Z. L.; Li, S. B.; Zhou, X. S.; Fan, F. R.; Zhang, W.; Zhou, Z. Y.; Wu, D. Y.; *et al.* Shell-Isolated Nanoparticle-Enhanced Raman Spectroscopy. *Nature* **2010**, *464*, 392–395.
(92) Lim, D.-K.; Jeon, K.-S.; Hwang, J.-H.; Kim, H.; Kwon, S.; Suh, Y. D.; Nam, J.-M. Highly Uniform and Reproducible Surface-Enhanced Raman Scattering from DNA-Tailorable Nanoparticles with 1 nm Interior Gap. *Nat. Nano* **2011**, *6*, 452–460.
(93) Niu, W.; Chua, Y. A. A.; Zhang, W.; Huang, H.; Lu, X. Highly Symmetric Gold Nanostars: Crystallographic Control and Surface-Enhanced Raman Scattering Property. *J. Am. Chem. Soc.* **2015**, *137*, 10460–10463.
(94) Hamon, C.; Novikov, S.; Scarabelli, L.; Basabe-Desmonts, L.; Liz-Marzán, L. M. Hierarchical Self-Assembly of Gold Nanoparticles into Patterned Plasmonic Nanostructures. *ACS Nano* **2014**, *8*, 10694–10703.
(95) McMahon, J. M.; Gray, S. K.; Schatz, G. C. Calculating Nonlocal Optical Properties of Structures with Arbitrary Shape. *Phys. Rev. B* **2010**, *82*, 035423.
(96) McMahon, J. M.; Gray, S. K.; Schatz, G. C. Optical Properties of Nanowire Dimers with a Spatially Nonlocal Dielectric Function. *Nano Lett.* **2010**, *10*, 3473–3481.

(97) Hohenester, U. Quantum Corrected Model for Plasmonic Nanoparticles: A Boundary Element Method Implementation. *Phys. Rev. B* **2015**, *91*, 205436.
(98) Mortensen, N. A.; Raza, S.; Wubs, M.; Søndergaard, T.; Bozhevolnyi, S. I. A Generalized Non-Local Optical Response Theory for Plasmonic Nanostructures. *Nat. Commun.* **2014**, *5*, 3809.
(99) Chulhai, D. V.; Jensen, L. Plasmonic Circular Dichroism of 310- and α-Helix Using a Discrete Interaction Model/Quantum Mechanics Method. *J. Phys. Chem. A* **2015**, *119*, 5218–5223.

CHAPTER 2

COMPUTATIONAL STUDY OF THE SURFACE-ENHANCED RAMAN SCATTERING FROM SILICA-COATED SILVER NANOWIRES

2.1 Introduction

Inelastic light scattering, or Raman scattering, from molecules is an exceedingly rare process with cross sections on the order of 10^{-30} cm^2/molecule, roughly 14 orders of magnitude smaller than that of fluorescence.[1] Historically, Raman scattering's inherently weak cross sections limited its usage as an analytical technique due to the exceptionally weak signal. A major effort to enhance the signal first presented itself in 1974 when researchers inadvertently discovered a phenomenon now called surface-enhanced Raman scattering (SERS). The researchers discovered that when pyridine molecules were adsorbed to roughened silver electrodes its Raman signal mysteriously increased.[2] It was later determined that the nanoscale features present on roughened noble metal surfaces support the propagation of surface plasmon polaritons and can subsequently enhance the Raman scattering cross section of nearby molecules.[3] In 1997, two reports of single-molecule sensitivities using SERS were published.[1,4] In both cases, molecules were placed in the rough crevices between silver nanoparticles, resulting in extraordinarily high enhancement. The past decade has seen an exponential growth of publications discussing both the fundamental aspects of SERS and numerous, innovative methods for chemical and biological sensing.[5]

Surface enhancement occurs when molecules are placed near the surface of plasmonically active nanostructures. Noble metals (typically gold or silver) exhibit a localized

---

surface plasmon resonance (LSPR), in the visible portion of the electromagnetic spectrum, when excited with light. The LSPR is a coherent oscillation of conduction band electrons that generates an evanescent electric field near the nanostructure's surface. Noble metals have optical properties that satisfy the resonance conditions necessary to support an LSPR. Specifically, the resonance conditions require that the complex permittivity ($\varepsilon = \varepsilon' + i\varepsilon''$) of the material have minimal loses ($\varepsilon'' \sim 0$) and a negative real component ($\varepsilon' < 0$).[6] Within the last decade or so, the wet chemical synthesis of plasmonic nanostructures has improved such that the community is now able to reliably and routinely synthesize nanostructures with tunable LSPR maxima such as nanorods[7] and nanowires,[8] among others.[9]

The rational design of SERS nanostructures requires consideration of the mechanisms that lead to surface-enhancement of the Raman scattering cross sections of analyte molecules. Researchers have established two primary mechanisms for explaining enhancement in SERS. The first and by far more dominant mechanism is called electromagnetic enhancement (EE). EE originates from the evanescent fields surrounding oscillating or propagating surface plasmons and is tunable by changing parameters such as the composition, geometry, or roughness of the nanostructure. The second, and minor, mechanism is called chemical enhancement (CE) and is likely due to a combination of energy transfer and resonance between the plasmonic surface and analyte molecules.[10] Due to the dominant magnitude of EE as well as difficulty in understanding and modeling CE, theoretical reports investigating the maximization of enhancement neglect CE and focus on EE. EE may be modeled *via* electromagnetic simulation tools and can be combined with optimization algorithms to rationally design optimal nanostructures.[11] Additional effort is being placed on modeling nanostructures by combining electromagnetic and quantum effects.[12] The EE factor, *G*, is mathematically related to the local electric field:

$G = |\mathbf{E}_{loc}(\omega)|^2|\mathbf{E}_{loc}(\omega - \delta\omega)|^2$, where ω is the excitation frequency and $\delta\omega$ is the Stokes shifted frequency that is dependent on the vibrational frequencies of the analyte. In general, the Stokes shift of interest is minimal such that a good approximation can be made to state that SERS is dependent on the fourth power of the local field: $G \approx |\mathbf{E}_{loc}(\omega)|^4$.

Plasmonic nanoparticles are typically treated analytically within the quasi-static approximation. The quasi-static approximation assumes the incident electric field over the entire nanoparticle is constant; this implies that the nanoparticle and surrounding media with electric potential ϕ may be described *via* Laplace's equation ($\nabla^2\phi = 0$), making the mathematics straightforward and computationally inexpensive. The analytical form of the quasi-static approximation, however, is limited to simple geometries (spheres, ellipsoids). Nanowires cannot be accurately described with the quasi-static approximation because the dimensions of the nanowire are on the same order of magnitude or even larger than the illumination source. Rather than trying to model the field distributions of nanowires analytically, researchers use computational electromagnetic techniques to visualize and understand the fields surrounding them. Techniques such as the finite difference time domain (FDTD) method,[13] the finite element method (FEM),[14] T-matrix,[15] and the boundary element method (BEM)[16] have been applied to nanoplasmonic structures. Here, we choose to use a commercial FEM software package, COMSOL Multiphysics, to model the EE and field distribution of silver nanowires. FEM's particular advantage is that it is able to accurately solve for the local electric field near the surface of the metal due to its inherent non-cubic mesh grid.[14] Furthermore, COMSOL's ability to solve for field distributions in three dimensions allows for us to accurately model anisotropic nanostructures.

Anisotropic nanostructures such as nanorods and nanowires consisting of gold or silver yield higher SERS intensities than equivalent surface area spherical nanoparticles. The usual explanation for this is that areas of increased radii of curvature induce "hot-spots" of electric fields at their tips by concentrating the optical fields through what is called the "lightning rod" effect of SERS.[17] Molecules placed at areas of concentrated fields will be greatly enhanced through the EE mechanism. Our previous experimental results indicated that colloidal patchy silica silver nanowires yield a higher SERS intensity than fully coated or uncoated silver nanowires.[18] We examine this unusual result *via* electromagnetic modeling in order to learn if the junction between a metal and a dielectric like silica can provide an unexpected type of SERS hot-spot.

2.2 Results and discussion

All simulations were performed using a commercial finite element method (FEM) software package, COMSOL Multiphysics v4.3a. The three-dimensional scattering domain consisted of a cylindrical scattering boundary condition surrounding the scatterer. Optical constants were obtained from Johnson and Christy[19] and used without any phenomenological corrections. The nanowire is assumed to be cylindrical with hemispherical end-caps having a total length ℓ and diameter d. Nanowire dimensions and silica coatings configurations were based on our previous experimental work.[18] We assume a nanowire of diameter 30 nm and varying lengths (200 nm, 500 nm, and 1000 nm), following typical parameters from the previous study. The scatterer is assumed to be submerged in pure water (n = 1.33 + 0i). Furthermore, the silver nanowire was illuminated with a uniform plane wave (633 nm) and polarized to excite the longitudinal LSPR, unless specified otherwise. Silica beads were created through the geometric intersection of perpendicular silica spheres (of diameter 30 nm) placed 15 nm from the nanowire

surface. Furthermore, the silica material was modeled with a relative permittivity of $\varepsilon = 4.5 + 0i$. Mesh density was adjusted for each individual scatterer and refined until a convergent solution was obtained.

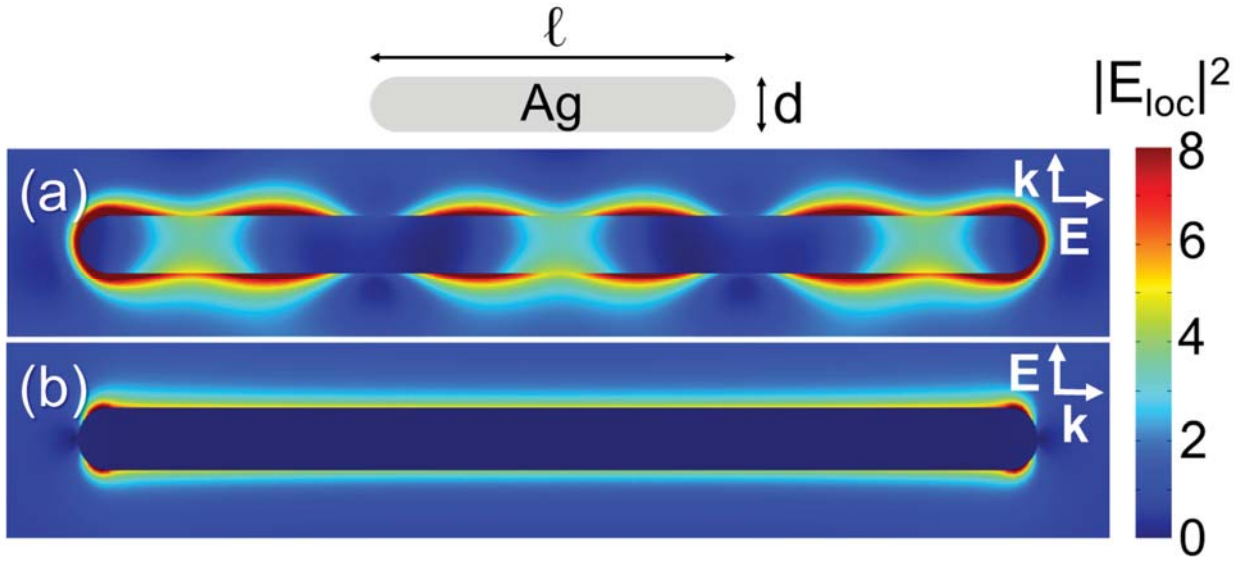

Figure 2.1. Finite element method (FEM) simulation of incident light ($\lambda = 633$ nm) on a silver nanowire ($\ell = 500$ nm, d = 30 nm) suspended in water ($n = 1.33$). (a) Plane wave light polarized such that the longitudinal mode is excited and (b) transverse mode excited.

Unlike nanorods and nanoparticles, nanowires exhibit higher-order modes due to their relatively significant dimensions with respect to the illumination wavelength. Figure 2.1 shows the local field intensity ($|\mathbf{E}_{loc}|^2$) of a silver nanowire ($\ell = 500$ nm, d = 30 nm) illuminated with a plane wave. As shown, the longitudinal surface plasmon resonance excites multiple modes along the entire length of the nanowire. As the dimensions of the nanowire increases, higher-order modes become more prevalent and the nanowire begins to lose some of its plasmonic activity along the longitudinal axis. The following results assume a longitudinal excitation as a limiting case due to the relative strength of the longitudinal versus transverse modes.

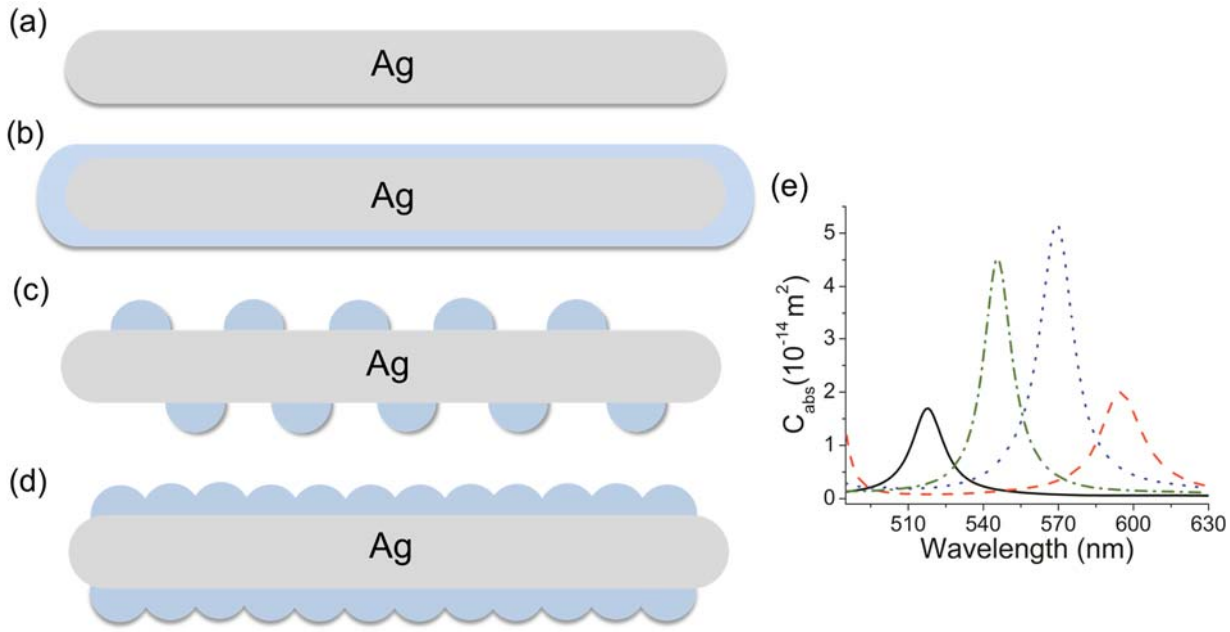

Figure 2.2. Schematic representation of the investigated silver nanowire configurations. (a) uncoated silver, (b) completely formation of silica coating a silver nanowire, (c) sparsely coated silver nanowire, (d) densely coated silver nanowire. All silica spheres were modeled with a radius of 15 nm and (e) absorption cross section C_{abs} of each configuration (ℓ = 200 nm, d = 30 nm) under longitudinally polarized light near the excitation wavelength; solid line (black) – uncoated silver; dash-dotted line (green) – sparsely coated silver; dotted line (blue) – densely coated silver; dashed line (red) – completely coated silver.

To study the effect of patchy silica-coated silver nanowires, we considered four different configurations of silica coatings, as shown in Figure 2.2. The investigated dimensions and configurations were based on our previous experimental work.[18] Silica coating is typically performed through the addition of a silane such as 3-mercaptopropyltrimethoxysilane (MPTMS) to an aqueous suspension of nanowires. As a result of thiol's strong affinity to metals, silver thiolate bonds will form on the surface of the nanowire. Nanometer-scale thick silica is grown through the addition of sodium silicate. As we have previously discussed,[18] thiolated Raman-active molecules compete with MPTMS for the silver surface and can result in patchy silica coatings if low concentrations of sodium silicate are added. Our simulation assumes that the thiolated molecules are immediately adjacent to the metallic surface. Additionally, we assume

that aggregates and metallic hot-spots are negligible or non-existent. For experimental studies, aggregates in solution can lead unreliable results because the signal intensity is heavily dependent on the positioning of the analyte molecule as well as the distance between metal surfaces. Aggregates concentrate the local electric field by several orders of magnitude but we currently lack the precision to reliably fabricate sub-nanometer features in wet chemistry. A framework for understanding signals recorded from suspensions of particles, using an effective medium theory, is then available to extrapolate results from single nanowires to ensemble measurements.[20,21]

Table 2.1. Simulation results of two different aspect ratios of patchy silica silver nanowires. A factor **ξ** characterizes the predicted relative enhancement.

Length (d)	Diameter (h)	Configuration	ξ
200 nm	30 nm	Uncoated	7.54
		Complete	29.2
		Sparse	9.65
		Dense	15.8
1000 nm	30 nm	Uncoated	5.98
		Complete	6.09
		Sparse	4.61
		Dense	9.23

To evaluate the differences in electromagnetic enhancement of the four configurations of silica-coated silver nanowires, we define a relative enhancement factor: $\xi = \frac{\iint |\mathbf{E}_{\text{loc}}|^4 dS}{\iint dS}$, where integration is evaluated over the entire silver nanowire surface. Two cases are considered; the

first is a silver nanowire of diameter d = 30 nm and length ℓ = 200 nm; the second is a silver nanowire of diameter d = 30 nm and length ℓ = 1000 nm (Table 2.1). In both cases, 30 nm diameter silica beads coat the silver nanowire for the sparse and dense configurations (see Figure 2.2). The fully coated silver nanowire has a 5 nm thick silica coating completely surrounding it.

The finite element method was used to model the extinction of the varying configurations of silica-coated silver nanowires. The absorption and extinction cross sections are expressed as the following:[22]

$$C_{\text{abs}} = k\iiint \text{Im}\{\tilde{n}\}^2 \left|\mathbf{E}(\mathbf{r}')\right|^2 d^3r' \tag{2.1}$$

$$C_{\text{ext}} = -k\,\text{Im}\left\{\iiint (\tilde{n}^2 - 1)\mathbf{E}(\mathbf{r}')\cdot\mathbf{E}^*_{\text{inc}}(\mathbf{r}')\,\text{d}^3\,r'\right\} \tag{2.2}$$

In this case, k corresponds to the wavevector, $\tilde{n}$ is a ratio between the frequency-dependent index of refraction of silver and the index of refraction of water ($\tilde{n} = n_{\text{Ag}}(\omega)/n_{\text{H}_2\text{0}}$). The incident electric field $\mathbf{E}_{\text{inc}}$ is assumed to be a time harmonic plane wave. Sub-micron and nanoscale silver scatterers can exhibit multiple resonances in the ultraviolet-visible spectrum; therefore, we focus on the shift in the localized surface plasmon resonance nearest the laser excitation wavelength (633 nm).

In case 1 (ℓ = 200 nm) we find that complete silica coverage of the nanowire results in the highest predicted enhancement with a nearly 4× higher ξ-factor than an uncoated silver nanowire. In contrast, case 2 (ℓ = 1000 nm) indicates that a densely coated silica nanowire will yield a higher ξ-factor, but only with an increase of ~1.5× compared to uncoated silver nanowires. Case 2 has less dramatic changes in enhancement, possibly because the plasmonic activity for longer nanowires is weaker. Varying degrees of silica will red-shift the LSPR

because the local dielectric environment around the nanowire changes. In case 2, further, the LSPR is far away enough from the excitation wavelength that small changes in the optical properties of the nanowire do not significantly impact the enhancement.

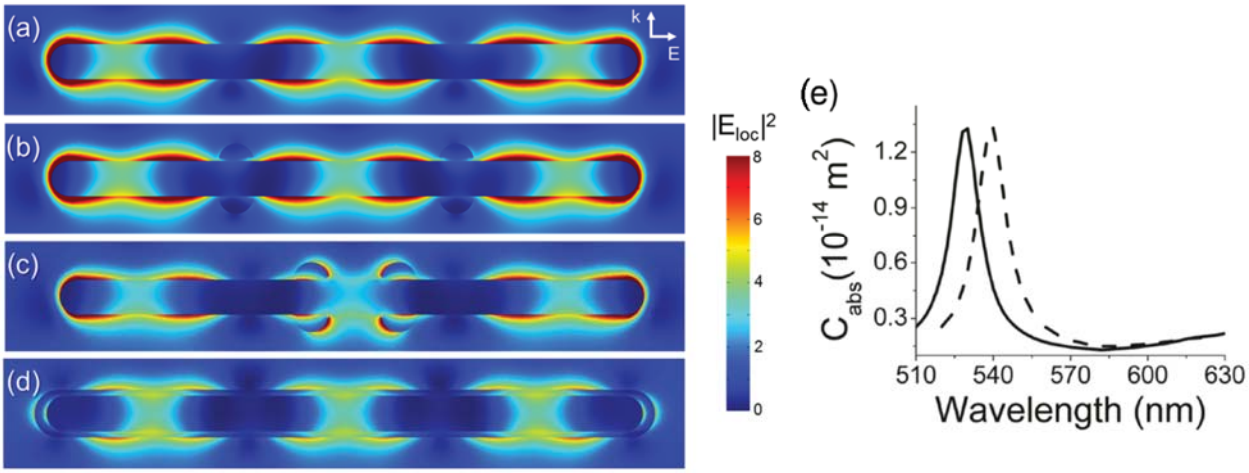

Figure 2.3. Local electric field intensities of silver nanowires (ℓ = 500 nm, d = 30 nm) demonstrating the distortion of the electric field. (a) Uncoated ξ = 21.8, (b) four silica beads placed at the electric field minima ξ = 21.7, (c) four silica beads placed at center maxima ξ = 0.55, (d) 5 nm thick silica surrounding the entire nanowire ξ = 6.93, and (e) absorption cross-section C_{abs} of configuration (b) – solid line and (c) – dashed line.

A non-uniform silica coating distorts the electric field around the nanowire surface and modifies the relative enhancement. As shown in Figure 2.3, several configurations of silica coatings were investigated for a 500 nm long silver nanowire. An uncoated silver nanowire is depicted in Figure 2.3(a) with an enhancement ξ = 21.8. In Figure 2.3(b), four silica beads (with a diameter of 30 nm) were placed at electric field minima and have a negligible effect on enhancement. Conversely, in Figure 2.3(c) the silica beads were placed at electric field maxima and heavily distort the electric field at the surface, reducing the enhancement to ξ = 0.55, nearly 40× less than that of uncoated silver. The shift in LSPR as a function of the location of silica beads in Figure 2.3(b) and 2.3(c) was calculated to be ~10 nm. In Figure 2.3(d) complete surface coverage of 5 nm thick silica is shown to partially distort the surface field. These results are in

agreement with the work of Mahmoud and coworkers[23] who found that silver nanocubes are sensitive to anisotropic changes in the surrounding dielectric medium. In this respect, patchy silica-coated silver nanowires are predicted to have differences in enhancement as compared to uncoated or fully coated nanostructures. The positions of the silica patches are shown to be crucial for changes in enhancement and understanding these is essential to understanding whether patchy silica coatings can enhance or reduce the capability of coated nanowire sensors. The results also provide impetus for new synthesis schemes to obtain designed composites at the nanoscale.

2.3 Conclusion

In this chapter we investigated the electromagnetic enhancement of silica coated silver nanowires using the finite element method. Computational techniques elucidate the properties of plasmonic nanostructures without the need for developing complex analytic solutions that are limited to specific geometries or materials properties and dimensions. Our results indicate shorter aspect ratio silver nanowires are more likely to be affected by differences in silica coating. We attribute this observation to the relative position of the longitudinal LSPR with respect to the laser excitation wavelength as well as the increased plasmonic activity of shorter aspect ratio nanowires. Additionally, silica on the surface of the nanowire can distort the local electric field, which is strongly dependent on the position of the silica coating. In this sense, silica coating has some limited ability enhance sensing by modifying electric fields, but will require the development of precise and controlled synthesis schemes to realize the advantages of patchy nanowires. With the appropriate consideration of the LSPR and silica configuration it may be possible to engineer nanowires with higher enhancements for SERS applications.

2.4 References

(1) Nie, S.; Emory, S. R. Probing Single Molecules and Single Nanoparticles by Surface-Enhanced Raman Scattering. *Science* **1997**, *275*, 1102–1106.
(2) Fleischmann, M.; Hendra, P. J.; McQuillan, A. J. Raman Spectra of Pyridine Adsorbed at a Silver Electrode. *Chem. Phys. Lett.* **1974**, *26*, 163–166.
(3) Moskovits, M. How the Localized Surface Plasmon Became Linked with Surface-Enhanced Raman Spectroscopy. *Notes Rec. R. Soc.* **2012**, *66*, 195–203.
(4) Kneipp, K.; Wang, Y.; Kneipp, H.; Perelman, L. T.; Itzkan, I.; Dasari, R. R.; Feld, M. S. Single Molecule Detection Using Surface-Enhanced Raman Scattering (SERS). *Phys. Rev. Lett.* **1997**, *78*, 1667–1670.
(5) Sharma, B.; Frontiera, R. R.; Henry, A.-I.; Ringe, E.; Van Duyne, R. P. SERS: Materials, Applications, and the Future. *Mater. Today* **2012**, *15*, 16–25.
(6) Novotny, L.; Hecht, B. *Principles of Nano-Optics*; 2nd ed.; Cambridge University Press, 2011.
(7) Jana, N. R.; Gearheart, L.; Murphy, C. J. Seed-Mediated Growth Approach for Shape-Controlled Synthesis of Spheroidal and Rod-like Gold Nanoparticles Using a Surfactant Template. *Adv. Mater.* **2001**, *13*, 1389–1393.
(8) Wiley, B.; Sun, Y.; Xia, Y. Synthesis of Silver Nanostructures with Controlled Shapes and Properties. *Acc. Chem. Res.* **2007**, *40*, 1067–1076.
(9) Sun, Y.; Xia, Y. Shape-Controlled Synthesis of Gold and Silver Nanoparticles. *Science* **2002**, *298*, 2176–2179.
(10) Moskovits, M. Persistent Misconceptions Regarding SERS. *Phys. Chem. Chem. Phys.* **2013**, *15*, 5301–5311.
(11) Kodali, A. K.; Llora, X.; Bhargava, R. Optimally Designed Nanolayered Metal-Dielectric Particles as Probes for Massively Multiplexed and Ultrasensitive Molecular Assays. *Proc. Natl. Acad. Sci.* **2010**, *107*, 13620–13625.
(12) McMahon, J. M.; Gray, S. K.; Schatz, G. C. Calculating Nonlocal Optical Properties of Structures with Arbitrary Shape. *Phys. Rev. B* **2010**, *82*, 035423.
(13) Atkinson, A. L.; McMahon, J. M.; Schatz, G. C. FDTD Studies of Metallic Nanoparticle Systems. In *Self Organization of Molecular Systems*; Russo, N.; Antonchenko, V. Y.; Kryachko, E. S., Eds.; Springer Netherlands: Dordrecht, 2009; pp. 11–32.
(14) Khoury, C. G.; Norton, S. J.; Vo-Dinh, T. Plasmonics of 3-D Nanoshell Dimers Using Multipole Expansion and Finite Element Method. *ACS Nano* **2009**, *3*, 2776–2788.
(15) Khlebtsov, N. G. T-Matrix Method in Plasmonics: An Overview. *J. Quant. Spectrosc. Radiat. Transf.* **2013**, *123*, 184–217.
(16) Myroshnychenko, V.; Carbó-Argibay, E.; Pastoriza-Santos, I.; Pérez-Juste, J.; Liz-Marzán, L. M.; García de Abajo, F. J. Modeling the Optical Response of Highly Faceted Metal Nanoparticles with a Fully 3D Boundary Element Method. *Adv. Mater.* **2008**, *20*, 4288–4293.
(17) Liao, P. F.; Wokaun, A. Lightning Rod Effect in Surface-Enhanced Raman Scattering. *J. Chem. Phys.* **1982**, *76*, 751–752.
(18) Murph, S. E. H.; Murphy, C. J. Patchy Silica-Coated Silver Nanowires as SERS Substrates. *J. Nanoparticle Res.* **2013**, *15*, 1–14.
(19) Johnson, P. B.; Christy, R. W. Optical Constants of the Noble Metals. *Phys. Rev. B* **1972**, *6*, 4370–4379.

(20) Sivapalan, S. T.; DeVetter, B. M.; Yang, T. K.; Schulmerich, M. V.; Bhargava, R.; Murphy, C. J. Surface-Enhanced Raman Spectroscopy of Polyelectrolyte-Wrapped Gold Nanoparticles in Colloidal Suspension. *J. Phys. Chem. C* **2013**, *117*, 10677–10682.
(21) Sivapalan, S. T.; Devetter, B. M.; Yang, T. K.; van Dijk, T.; Schulmerich, M. V.; Carney, P. S.; Bhargava, R.; Murphy, C. J. Off-Resonance Surface-Enhanced Raman Spectroscopy from Gold Nanorod Suspensions as a Function of Aspect Ratio: Not What We Thought. *ACS Nano* **2013**, *7*, 2099–2105.
(22) Hage, J. I.; Greenberg, J. M.; Wang, R. T. Scattering from Arbitrarily Shaped Particles: Theory and Experiment. *Appl. Opt.* **1991**, *30*, 1141–1152.
(23) Mahmoud, M. A.; Chamanzar, M.; Adibi, A.; El-Sayed, M. A. Effect of the Dielectric Constant of the Surrounding Medium and the Substrate on the Surface Plasmon Resonance Spectrum and Sensitivity Factors of Highly Symmetric Systems: Silver Nanocubes. *J. Am. Chem. Soc.* **2012**, *134*, 6434–6442.

CHAPTER 3

OBSERVATION OF MOLECULAR DIFFUSION IN POLYELECTROLYTE-WRAPPED SURFACE-ENHANCED RAMAN SCATTERING NANOPROBES

3.1 Introduction

Chemical sensing using surface-enhanced Raman spectroscopy (SERS) has recently exploded in popularity as wet chemical nanosynthesis techniques, especially related to surface control, have evolved.[1–3] A technique called layer-by-layer (LbL) polyelectrolyte wrapping has been used in recent years for a diverse set of surface control applications ranging from drug delivery,[4] biomimetic sensors,[5] and biofilms for medical implants.[6] LbL offers multiple advantages in terms of practical sensing including facile, precise, and robust control over nanoparticle surface chemistry. With LbL, it is straightforward to modify the surface chemistry and charge of hydrophilic nanoparticles with the incubation of polyelectrolyte containing solutions with minimal preparation.[7] Nanoparticles are easily functionalized with reactive moieties and reacted with biomolecules or fluorescent tags for sensing applications. Additionally, LbL-wrapped nanoparticles resist aggregation in both polar and non-polar solvents through steric effects, making them a valuable tool for improving colloidal nanoparticle stability.[8] LbL-wrapping is a major advance in terms of nanomaterial surface control and will continue to be an important tool for biological sensing due to the chemical and optical complexity of the tissue microenvironment.

The incorporation of specific optical reporter molecules into plasmonic nanostructures is necessary to accomplish SERS sensing. Optical reporter molecules typically consist of

---

fluorophores or other heavily conjugated molecules with delocalized π-electrons electrostatically bound near the nanoparticle surface. Encapsulation of reporter molecules is necessary upon exposure to harsh ionic environments or biological systems where the molecules are likely to leach into the environment. Currently, a variety of techniques are employed for this purpose. The most popular technique involves the encapsulation of Raman-active molecules into silica layers grown around metallic nanoparticles. This process is based off the Stöber method in which silica is formed *via* the condensation of tetraethyl orthosilicate (TEOS) or sodium silicate onto a nanoparticle surface bearing poly(ethylene glycol) (PEG) or silane ligands.[9,10] While silica is effective at molecular encapsulation, its growth is prone to variability, requires organic solvents, and is time consuming. Furthermore, it is difficult to spatially localize vitrified molecules with respect to their distance from the metallic surface, which is a critical factor in determining SERS activity.

LbL encapsulation of reporter molecules is an emerging technique that addresses many crucial aspects in the design of SERS nanoprobes. In this technique, reporter molecules are electrostatically bound to an oppositely charged polyelectrolyte wrapped around the nanoparticle surface. After a short incubation period, additional layers of polyelectrolyte may be wrapped around the nanoparticle, effectively trapping the reporter molecule in a soft template of polymer. LbL-wrapping, in contrast to silica coating, is straightforward, reproducible, and requires minimal characterization during the wrapping stages. Design flexibility involving factors such as porosity, coating density, and conformation of the bound polyelectrolyte are possible through tuning the pH, salt concentration, molecular weight of the polyelectrolyte, and electrolytic strength. Furthermore, each polyelectrolyte multilayer adds an additional thickness of ~1.5 nm, from which it is possible to approximately localize the trapped molecules.[7] We have previously

demonstrated this technique,[11,12] illustrating its robustness as a preparation method for SERS nanoprobes.

In this chapter, we investigated the long-term storage and stability of SERS nanoprobes in the form of polyelectrolyte-wrapped gold nanoparticles. Predicting and understanding the SERS signal intensity over long periods of time under a variety of environmental conditions is essential for the design of SERS nanoprobes intended for biological sensing applications. Numerous reports investigating the formation and control over layer deposition of polyelectrolyte multilayers have yet to explore the signal stability of polyelectrolyte encapsulated reporter molecules. Unlike drug delivery studies with intentionally porous or degradable films, SERS nanoprobes are designed to maintain their structure and chemical signature over an indefinite period of time without noticeable signal loss. We maximized the reproducibility of our measurements and mimicked the optical environmental conditions of a tissue-based measurement by performing all Raman measurements in-suspension with near-infrared laser excitation. Near-IR excitation exploits the so-called "optical window" (600 – 1000 nm) where tissue absorbs less light, increasing penetration depth.[13,14] Suspension-based measurements within a finite path length cuvette ensured proper accounting for the anticipated optical effects between SERS and light extinction in tissue measurements.[11,15] Nanoprobe stability was investigated by storing aliquoted samples at 4 °C, room temperature, and physiological temperature (37 °C) for a period of 5 weeks. SERS measurements were performed periodically during this period to assess changes in signal. To further investigate the stability and lifetime of our nanoprobes, we also studied chemically cross-linked polyelectrolyte layers and thiolated molecules.

3.2 Experimental

Materials. Cetyltrimethylammonium bromide (CTAB, > 99%), sodium borohydride ($NaBH_4$, > 99.99%), ~15,000 g/mol poly(acrylic acid, sodium salt) (PAA), ~15,000 g/mol poly(allylamine hydrochloride) (PAH), 5,5'-dithiobis(2-nitrobenzoic acid) (DTNB, > 98%), ascorbic acid (> 99%), 5,000 g/mol methyl ether poly(ethylene glycol) thiol (mPEG-SH), glutaraldehyde (EM grade 8% in H_2O), bovine serum albumin (BSA, > 96%), and methylene blue (MB, > 82%) were purchased from Sigma-Aldrich and used without further purification. All glassware was cleaned with aqua regia (3:1 HCl:HNO_3) and rinsed multiple times with 18 MΩ-cm water.

Characterization. Holey carbon transmission electron micrograph (TEM) sample grids were purchased from Pacific Grid-Tech. Samples were prepared by drying 10 μL of solution onto each grid. The size distribution was verified by examining at least 100 particles per grid using ImageJ analysis software. ζ-potential measurements were performed on a Brookhaven ZetaPALS instrument. Electronic absorption spectra were recorded with a GE GeneQuant 1300 spectrophotometer. Centrifugation was performed using a Thermo Scientific Sorvall Legend X1 centrifuge with a swinging bucket configuration.

Raman measurements. Raman spectra were measured using a Horiba LabRAM Confocal Raman microscope with the laser line configured to an excitation wavelength of 785 nm. All measurements were performed with a 1 cm path length quartz cuvette and an incident power of ~14 mW in a reflection collection geometry. Integration time was varied between 10 and 20 seconds, depending on the concentration of individual nanoparticle solutions, with a spectral resolution of 10 cm^{-1}. Samples were stored at 4 °C, room temperature (~22 °C), or 37 °C. All samples were allowed to equilibrate to room temperature before Raman measurements were performed.

Nanosphere synthesis. Gold nanospheres were first prepared by synthesizing seed using a modified protocol intended for nanocube synthesis.[16] Under vigorous magnetic stirring 0.25 mL $HAuCl_4$ (0.01 M) and 7.5 mL CTAB (0.1 M) were mixed. To this solution, freshly prepared, ice-cold 0.6 mL (0.01 M) $NaBH_4$ was added. The solution immediately turned from yellow to light brown. The seed was kept at room temperature for a minimum of one hour to fully hydrolyze any remaining $NaBH_4$. Gold nanospheres were synthesized in 40 mL batches consisting of 6.4 mL CTAB (0.1 M), 0.8 mL $HAuCl_4$ (0.01 M), and 32 mL of H_2O. To this solution, 3.8 mL of ascorbic acid (0.1 M) was added and turned the solution colorless. The seed was diluted 2× and 20 μL was added. The solution slowly turned pink and after 30 minutes turned red. Centrifugation was performed twice at 5,000 × g for 60 minutes to remove excess surfactant.

Polyelectrolyte wrapping of gold nanospheres. Aqueous **s**tock solutions of PAA and PAH were prepared at a concentration of 10 mg/mL (containing 1 mM NaCl). To 30 mL of gold nanospheres, at the as-synthesized concentration, 6 mL of PAA or PAH stock were added along with 3 mL of 10 mM NaCl. To the first layer of PAA, 500 μL of 1 mM methylene blue (dissolved in methanol) was added and allowed to complex for 1 hour. After each step, the nanoparticle solutions were centrifuged at 3,000 × g for 1 hour to remove excess reagents. The BSA layer was formed by adding 500 μL of 1 wt. % BSA to the suspension and allowing it to react for 2 hours at room temperature. This corresponds to a ~2000× molar excess of BSA to nanoparticles. Immediately afterwards, the solution was dialyzed in 4 L of water with a 100,000 g/mol membrane for 48 hours. The water was changed multiple times to ensure complete removal of unbound reagents. A highly concentrated stock solution was made such that aliquots were taken and diluted into the appropriate buffer for each experiment. PAA and PAH

layers have weak Raman scattering cross sections as compared to methylene blue. All samples were stored in 15 mL polypropylene conical tubes pre-treated with 1 wt. % BSA solution to minimize sticking of nanoparticles to the tube. Measurements were performed in triplicate and each solution was adjusted to a concentration of 0.15 nM.

Thiol coating of gold nanospheres. To 40 mL of as-synthesized gold nanospheres, 5 mL of 1 mM mPEG-SH was added dropwise and under sonication. Immediately following mPEG-SH addition 2 mL of 1 mM DTNB was added. Note that the DTNB was adjusted to a pH 7 – 7.4 to facilitate water solubility. The solution was allowed to complex overnight and then centrifuged at 4,200 × g for 1 hour. The supernatant was discarded and the pellet was re-suspended to 3 mL and 500 μL of 1 wt. % BSA was added. Dialysis with a 100,000 g/mol membrane was performed in 4 L of water over 48 hours.

PAH crosslinking. Twice purified gold nanospheres were diluted to a volume of 30 mL. To fabricate the core-shell structure, 6 mL of PAA solution was added along with 3 mL of 10 mM NaCl and allowed to sit for 1 hour. The solution was then centrifuged at 4,800 × g for 1 hour. Following purification of PAA, 1 mL of 750 μM of methylene blue (in methanol) was added. After 1 hour, the solution was centrifuged at 4,800 × g for 1 hour to remove excess dye. The solution was suspended in 30 mL of H_2O and 6 mL of PAH stock was added with 3 mL of 10 mM NaCl. Finally the solution was centrifuged again at 4,000 × g for 1 hour and re-suspended in H_2O to obtain an optical density of 4. A solution consisting of 1 mL of 8% glutaraldehyde was added and allowed to react for 2 hours at 4 °C. Purification was performed against a 3,500 g/mol dialysis membrane for 48 hours in 4 L of water to remove excess reagents. Raman measurements were performed on aliquots of this solution at a concentration of 0.25 nM.

Finite element method calculations. Finite element method calculations were performed using COMSOL Multiphysics v4.3b with the RF and Chemical Reaction Engineering modules. Diffusion of methylene blue through polyelectrolyte layers was modeled with an impermeable boundary around a gold core of diameter 40 nm. A spherical shell 5 nm thick coated the gold core to represent the CTAB and PAA layer. Methylene blue was assumed to have a 2 nm thick layer with a uniform distribution equating to 3000 molecules based off our previously experimental work.[12] A 5 nm shell surrounded the methylene blue layer to account for the PAA/PAH/BSA layers.

3.3 Results and discussion

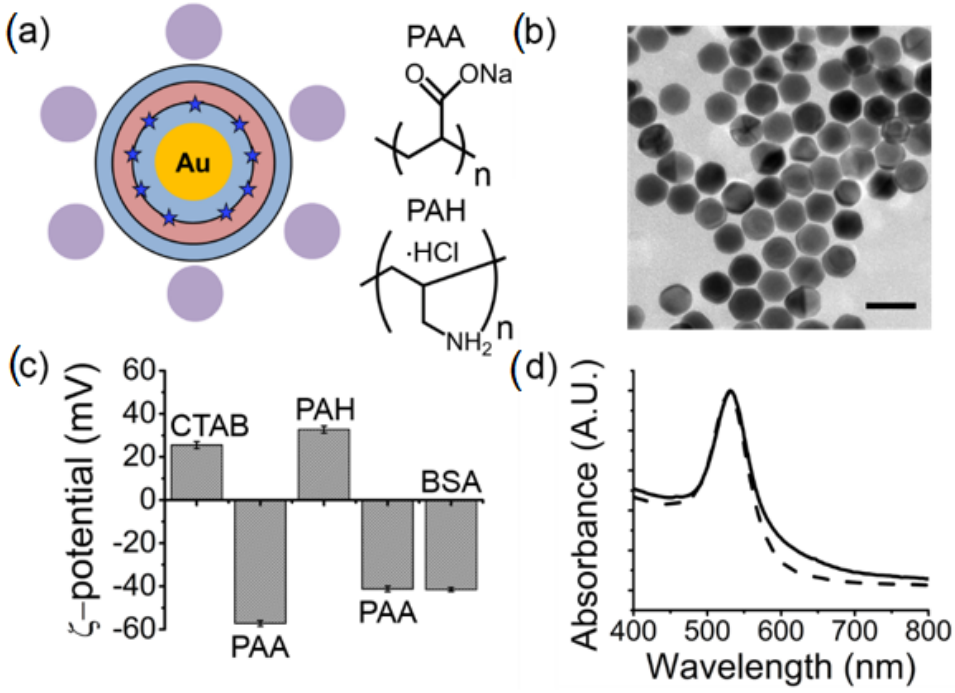

Figure 3.1. (a) Schematic of prepared gold nanospheres with alternating layers of PAA (light blue shell), PAH (red shell), and methylene blue (blue stars). To prevent aggregation in highly ionic solutions, BSA (purple circles) was bound to the outer layer. (b) Transmission electron micrograph of gold nanospheres. Scale bar: 50 nm. (c) Representative ζ-potential for each surface coating in the synthesis. (d) Electronic absorption spectra of CTAB-stabilized gold nanospheres (dotted line) compared to polyelectrolyte-wrapped nanospheres (solid line).

SERS nanoprobes were fabricated by wrapping alternating layers of weakly anionic poly(acrylic acid, sodium salt) (PAA) and cationic poly(allylamine hydrochloride) (PAH) around gold nanospheres stabilized with cetyltrimethylammonium bromide (CTAB) surfactant. As shown in Figure 3.1(a), cationic optical reporter molecules (methylene blue) were encapsulated electrostatically between the first layer of PAA and subsequent layers of polyelectrolyte and bovine serum albumin (BSA). Protein-induced flocculation was prevented by wrapping a final layer of PAA around the nanostructure before the addition of BSA. Bioconjugation studies typically use BSA to quench excess reactive sites on antibody-conjugated nanoparticles as well as to prevent non-specific binding to "sticky" cell receptors *in vitro*. Here, BSA serves dual purposes. First, BSA stabilizes nanoparticles in highly ionic solutions such as phosphate buffered saline, which is a common buffer used in cell culture and mimics the environment found in tissue. Second, all nanoparticles exposed to whole blood or serum will immediately develop a protein corona in which proteins dynamically associate and dissociate from the surface. Researchers continue to intensely study the effects of the protein corona both *in vitro* and *in vivo* as it can have significant unavoidable consequences on biocompatibility, renal clearance, and targeting capabilities.[17] The synthesized nanostructures were characterized with transmission electron microscopy (TEM) and ζ-potential. At room temperature all samples displayed stable electronic absorption spectra for > 5 weeks. This robust method provides some design guidance in terms of the spatial localization of the reporter molecules. We anticipate that the reporter molecules will be located approximately 4 nm from the metallic surface.[7]

Quantification of surface-enhancement is often a source of confusion and contention. A major source of contention originates from the mechanism of surface-enhancement itself. Molecules obeying Raman selection rules exhibit enhancement through a combination of the

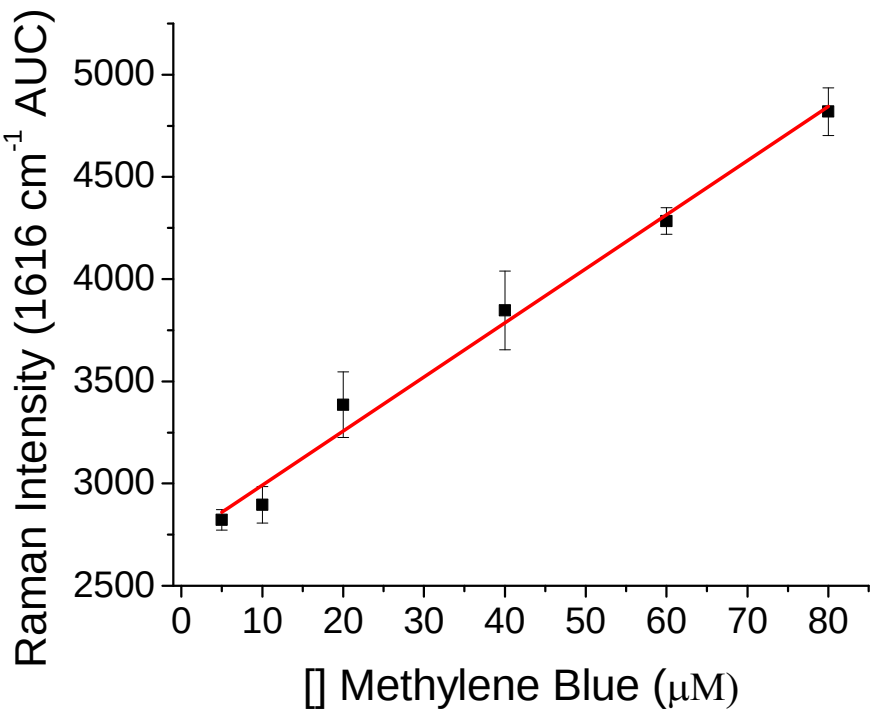

Figure 3.2. Spontaneous Raman calibration curve of aqueous methylene blue from 5 – 80 μM. The equation of the line was determined through linear regression to be: $y = 26.5x + 2730$.

commonly attributed chemical and electromagnetic enhancement effects of SERS. The electromagnetic enhancement effect is generally regarded as the dominant mechanism; although, this remains an active area of research.[18,19] Quantification is further confused by the mechanics of calculating enhancement factors. Recently, Le Ru and Etchegoin discussed mathematical and interpretative errors made in the first two reports on single-molecule SERS where enhancement factors (EFs) of 10^{14} were reported.[18] The propagation of these errors in comparison to fluorescence cross sections resulted in numerous subsequent reports claiming similar results. In many of these studies, the EF was empirically determined from the following equation: $\mathrm{EF} = \frac{N_{\mathrm{Raman}} I_{\mathrm{SERS}}}{N_{\mathrm{SERS}} I_{\mathrm{Raman}}}$, where N_{Raman} and I_{Raman} are the number of molecules in the focal volume and its corresponding spontaneous Raman intensity. Likewise, N_{SERS} and I_{SERS} correspond to the

number of probed molecules bound to the nanoparticles and their corresponding SERS intensity. We approach the quantification of SERS enhancement in a slightly different manner.[12] Aqueous MB standards were prepared ranging in concentration from 5 – 80 μM. A linear calibration curve was developed, as shown in Figure 3.2. All data was quantified at the ν (C-C) ring stretching vibration at 1616 cm^{-1}.[20] Based on the calibration curve and SERS intensity of each sample (normalized to incident laser power), an equivalent spontaneous Raman signal may be calculated. The Raman equivalent signal corresponds to the equivalent concentration of MB molecules required to produce the same spontaneous Raman signal intensity as the probed solution. With this technique no assumptions of molecular coverage are necessary.

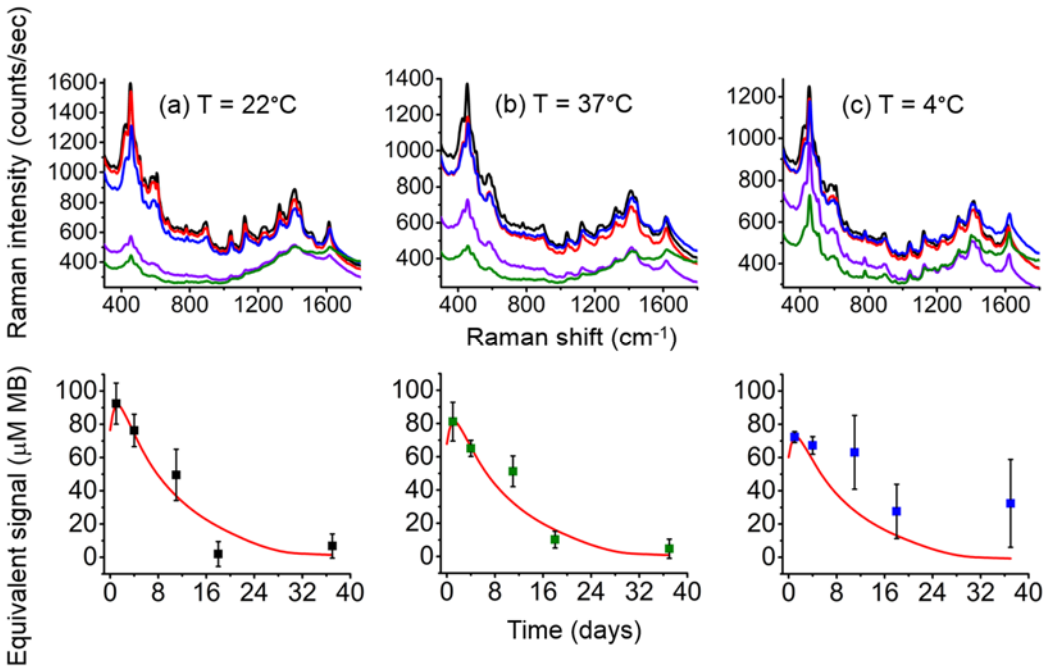

Figure 3.3. Above: SERS spectra of LbL-wrapped nanospheres; Day 1, black; Day 4, red; Day 11, blue; Day 18, purple; Day 37, green. Samples were stored at (a) 22 °C, (b) 37 °C, and (c) 4 °C. Below: Predicted signal intensity (red line) and the experimental spontaneous Raman equivalent signal quantified at the 1616 cm^{-1} band. All samples were normalized to 0.15 nM.

Using a spontaneous Raman quantification technique, we investigated the signal stability of the nanoprobes described in Figure 3.1a over the course of 5 weeks. Triplicate aliquots of

solutions were stored at room temperature (~22 °C), 37 °C, and 4 °C. As shown in Figure 3.3, the spectral features tend to change and decay as time progresses. Samples stored at 4 °C, while having the largest variation in signal, maintained their spectral shape better than samples stored at warmer temperatures. Intuitively, the diffusion of molecules through polyelectrolyte layers is expected to be linearly related to temperature, *i.e.*, analogous to the Stokes-Einstein relationship. After 5 weeks of storage, several samples were centrifuged to concentrate the nanoparticles into pellets. We calculated that a 3 mL solution of 0.15 nM nanoparticles should release approximately 5 μM of reporter molecules. The supernatant was extracted and we found that it did not contain a micromolar quantity of dye molecules, indicating that a fraction of the methylene blue molecules were trapped away from the metallic surface but not free in solution. To understand this process and determine if diffusion can be ascribed as a major cause of the loss of signal, we carried out modeling. The first part of our model involves the temporal prediction of the diffusion of the reporter molecules through the polyelectrolyte layers. The second part relates the concentration to the electromagnetic enhancement factor, thereby producing a total predicted intensity.

Neglecting the effects of concentration due to the low loading and charge, diffusion through polyelectrolyte layers was assumed to be constant and modeled using Fick's second law of diffusion, as shown in Figure 3.4:

$$\frac{\partial C(x,t)}{\partial t} = \mathrm{D}\,\frac{\partial^2 C(x,t)}{\partial x^2} \tag{3.1}$$

where D is the diffusion coefficient and C is the concentration as a function of position, x, and time, t. Equation (3.1) was solved using the finite element method with an impermeable

boundary condition at the surface of the gold core, a uniform distribution of methylene blue, and an enforced concentration of zero at the edge of the BSA-water interface. The latter boundary

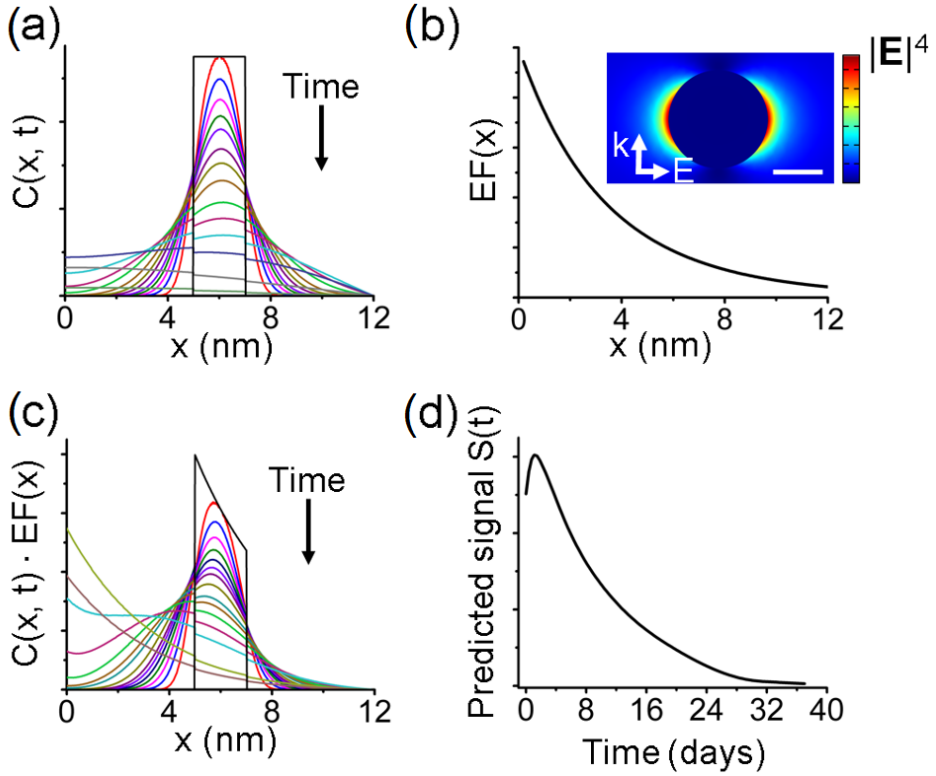

Figure 3.4. (a) Concentration profile as a function of time with a diffusion coefficient of $D = 10^{-18}$ cm^2/s. (b) Calculated electromagnetic enhancement factor (EF) for a 40 nm gold nanosphere as a function of distance from the surface. Inset: Gold nanosphere illustrating a dipolar plasmon resonance. Scale bar: 20 nm. (c) Calculated profile of EF and concentration. (d) Predicted signal intensity $S(t)$.

condition is justified as diffusion within the solution would be much faster than diffusion in the polyelectrolyte layers. Mathematically, the boundary conditions may be stated as:

$$\frac{\partial C(x,t)}{\partial x} = 0, \quad x \le 0\,\text{nm} \tag{3.2}$$

$$C(x,t) = C_0, \quad 5\,\text{nm} \le x \le 7\,\text{nm}, \quad t \le 0 \tag{3.3}$$

$$C(x,t) = 0, \quad x \ge 12\,\text{nm} \tag{3.4}$$

where C_0 corresponds to the initial distribution of molecules uniformly positioned within a 2 nm thick layer. Furthermore, the model conserved flux across these three regions: $\frac{\partial C_1}{\partial x} = \frac{\partial C_2}{\partial x}$ and $\frac{\partial C_2}{\partial x} = \frac{\partial C_3}{\partial x}$ with a fixed coefficient $k = \frac{C_1}{C_2} = \frac{C_2}{C_3} = 0.9.$ The diffusion coefficient was determined by simulating concentration versus time with a range of values from $D = 10^{-16}$ to 6×10^{-18} cm^2/s, as shown in Figure 3.5. After an approximate match was identified, the simulated signal was compared to the experimental data to further optimize the result. We found that a diffusion coefficient of $D = 10^{-18}$ cm^2/s provided the most appropriate fit. It should be noted that the value of D is calculated under the assumption of specific boundary conditions, *i.e.,* zero concentration at the particle boundary. It is likely that some methylene blue is trapped within the particle and at its surface, resulting in a smaller concentration gradient than the one assumed in our model that would lead to a lower value of D being estimated. Under these constraints, the value of D should be used to impute a loss of signal rather than a loss of concentration.

The second portion of our model incorporates the ability of a plasmonic nanoparticle to surface-enhance the chemical signature of nearby molecules from the metallic surface. For a spherical plasmonic nanosphere, a dipolar evanescent electric field is generated when illuminated with a plane wave. The local electric field $\mathbf{E}_{loc}$ dictates the degree of enhancement approximately by $|\mathbf{E}_{loc}|^4$. Under the assumption of a quasi-static electric field, a nanoparticle's enhancement factor (EF) decays as EF $\propto 1/(a + d)^{12}$, where a is the radius of the nanoparticle and d is the distance of the molecule from the surface.[21] Thus, the signal relies heavily on the position of the molecule. The product of enhancement and concentration is shown in Figure 3.4(c) as a function of time. The predicted signal, *S(t),* was calculated by the following:

$$S(t) = \int \mathrm{EF}(x)C(x,t)\mathrm{d}x \tag{3.5}$$

Reporter molecules are predicted to diffuse both toward and away from the metallic core. As a result, signal intensity is bolstered by molecules diffusing closer to the nanoparticle surface. The

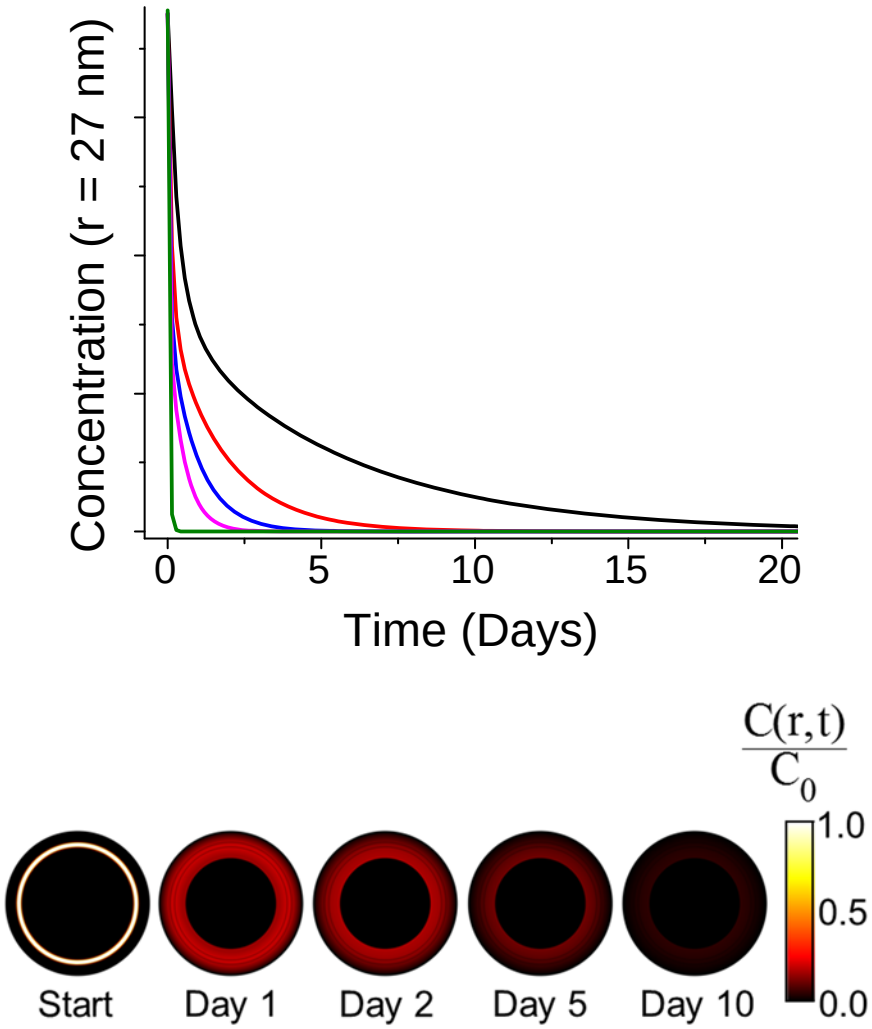

Figure 3.5. Top: Calculated diffusion of methylene blue through polyelectrolyte layers with varying diffusion coefficients; black, $D = 1 \times 10^{-18}$ cm^2/s; red, 3×10^{-18} cm^2/s; blue, 6×10^{-18} cm^2/s; pink, 1.1×10^{-17} cm^2/s; green, 1×10^{-16} cm^2/s. Bottom: Modeled concentration profile of LbL-wrapped nanostructure ($D = 1 \times 10^{-18}$ cm^2/s) with an impermeable boundary at the gold-polyelectrolyte interface and an infinite sink at the BSA-water interface. In this initial model, flux was not conserved across the three regions (polyelectrolyte-MB, MB, MB-polyelectrolyte), resulting in a rapid decay in signal intensity.

diffusion coefficient was empirically determined from our data. In a previous study, Chung and Rubner experimentally determined the diffusion coefficient for methylene blue in alternating layers of PAA and PAH on substrates to be on the order of 10^{-14} – 10^{-16} cm^2/s, depending on pH and buffer conditions.[22] Klitzing and Möhwald recorded a diffusion coefficient on the order of 10^{-15} cm^2/s for the diffusion of rhodamine through polyelectrolyte films.[23] In our case, the diffusion coefficient was smaller by two to three orders of magnitude. Numerous factors could contribute to the discrepancy including the presence of a negatively charged outer BSA layer, ionic strength, buffer conditions, or the binding affinity of polyelectrolyte layers around gold nanoparticles versus glass substrates. It should also be noted that there have been some reports describing the non-Fickian behavior of small molecule diffusion through polyelectrolytes as a result of swelling and electrostatic effects.[24,25]

Typically, the design of SERS nanoprobes using encapsulation methods seek to minimize diffusion. While simple encapsulation in a multilayer system can be a facile route, it results in a limited shelf life due to these effects. Hence, we explored a strategy to reduce diffusion by gelling the outermost polymer layer and imparting much greater stability to the nanoprobe's

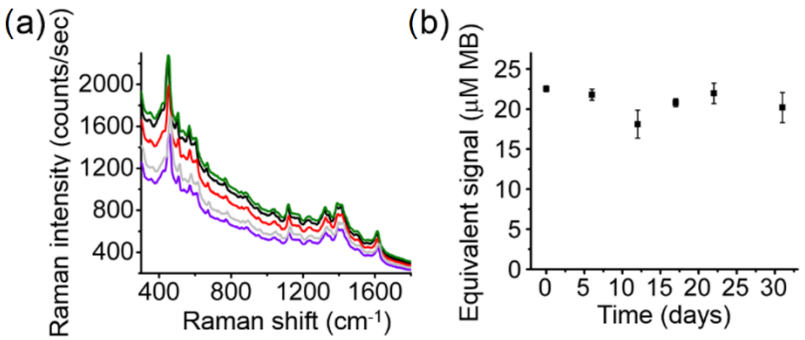

Figure 3.6. Methylene blue molecules were electrostatically encapsulated between PAA and PAH layers. Aliphatic amines from the PAH layer were chemically crosslinked and stored at 4 °C to help prevent diffusion. (a) SERS spectra of glutaraldehyde crosslinked nanoparticles. Day 1, black; Day 6, red; Day 12, blue; Day 17, purple; Day 22, green; Day 31, grey. (b) Quantification of SERS intensity in terms of equivalent spontaneous Raman signal of methylene blue.

SERS intensity over long periods of time.

As shown in Figure 3.6, chemical crosslinking was investigated as a method for minimizing undesirable diffusion of optical reporter molecules. An amine reactive crosslinker (glutaraldehyde) was added in molar excess to a solution consisting of LbL-encapsulated nanostructures (PAA + MB + PAH). Glutaraldehyde crosslinked available aliphatic amines on the terminal PAH layer. We observed that after a 2 hour incubation period, LbL-glutaraldehyde nanoparticles were stable and did not show signs of aggregation as measured by electronic absorption spectroscopy. In Figure 3.6, we show that crosslinked nanoparticles are significantly less susceptible to diffusion-dominated signal loss. As described in Figure 3.7, crosslinked samples stored at 4 °C were more stable than samples stored at room temperature.

Crosslinking of the outer polyelectrolyte layer likely improves the outer shell stability of the nanoparticle and decreases pore size such that the reporter molecules do not as readily

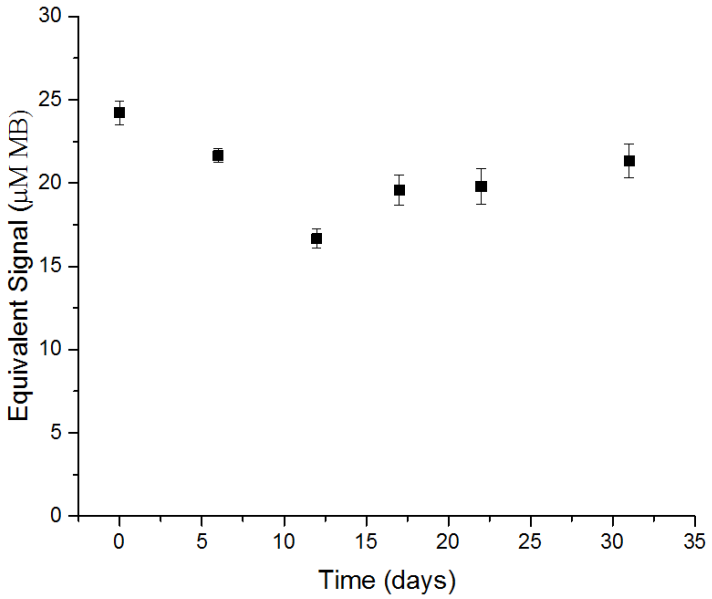

Figure 3.7. Spontaneous Raman equivalent signal of chemically crosslinked PAA+MB+PAH nanostructures stored at room temperature. Minimal loss of signal is observed over the storage period.

diffuse. DLS was used to verify the size distribution after multiple weeks of storage, as shown in Figure 3.8. The porosity and conformation of polyelectrolyte layers bound to gold nanoparticles is difficult to ascertain due to inherent variability in individual nanoparticles and the sheer

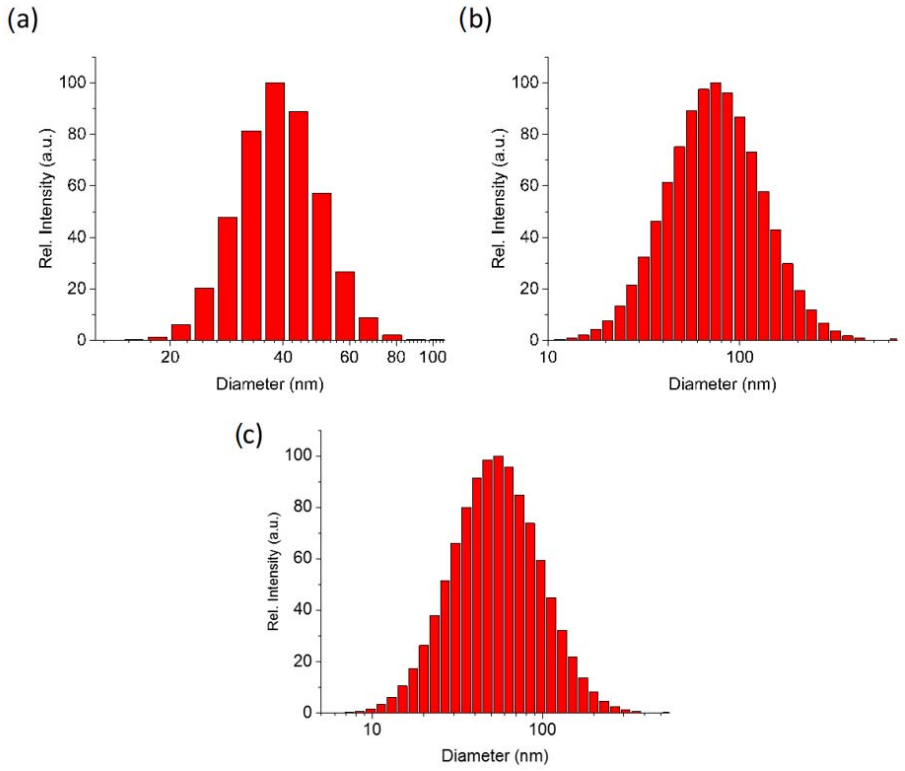

Figure 3.8. Dynamic light scattering data (a) before and (b) after functionalization of gold nanospheres with a polyelectrolyte coating and BSA stored for a period of more than 5 weeks at room temperature. (c) Dynamic light scattering results of glutaraldehyde crosslinked sample after > 5 weeks of storage at room temperature.

quantity of particles in solution. To date, polyelectrolyte-based studies have focused on the characterization of polyelectrolyte multilayer thin films bound to substrates. Researchers have shown results demonstrating that changes in a solution's pH can affect porosity. In fact, when washing with acidic solutions (pH = 2.4), the porosity of PAA/PAH films is greatly increased.[26] It has also been demonstrated that exposure of PAA/PAH films to pure water can increase the surface roughness of bound polyelectrolytes.[27] By exploiting tunability in porosity, it may also

be possible to design versatile drug delivery systems. In addition to porosity, the diffusive properties of polyelectrolyte-wrapped nanoparticles has led to their use as drug delivery platforms,[4,25] where control of the diffusion of small molecules is desirable. Our experimental and theoretical results indicate diffusive-like behavior in polyelectrolyte multilayers, which is necessary for tuning the release profile in terms of drug delivery and is, of course, likely to be crucial in the design of multifunctional theranostic particles.

While the previous discussion has focused on nanoprobes that were electrostatically trapped by LbL assembly, another route to effective SERS sensing is by way of passivating optical reporter molecules at the surface of the nanoparticle. Thiolated molecules were used to investigate the stability of non-diffusive, covalently bound Raman molecules. Thiol has a strong affinity for metals such as gold and forms a covalent gold-thiolate bond.[28] To investigate signal stability we used Ellman's Reagent or 5,5'-dithiobis(2-nitrobenzoic acid) (DTNB), which has a strong symmetric NO_2 stretch at 1333 cm^{-1}.[29] Upon reduction, the disulfide bond readily cleaves into two 5-thio-nitrobenzoic acid (TNB) molecules. Figure 3.9 shows that nanoprobes were prepared with a mixed layer of methyl ether poly(ethylene glycol) thiol (mPEG-SH) and TNB. A layer of BSA was adsorbed to the outermost layer to mimic the polyelectrolyte configuration. ζ-potential measurements verified that each synthetic step was successful. Samples were prepared in triplicate and stored at identical temperatures as the polyelectrolyte-wrapped nanoparticles. Figure 3.9(c) shows representative Raman spectra (normalized to laser power) of TNB-PEG coated nanoparticles stored for more than 5 weeks at room temperature. Throughout the storage period the spectral features exhibit only slight variations. Spontaneous Raman equivalents, as shown in Figure 3.10, were computed using a spontaneous Raman calibration curve of aqueous DTNB (ranging from 5 to 15 mM) with an adjusted pH of 7. Due to the strength of the gold-

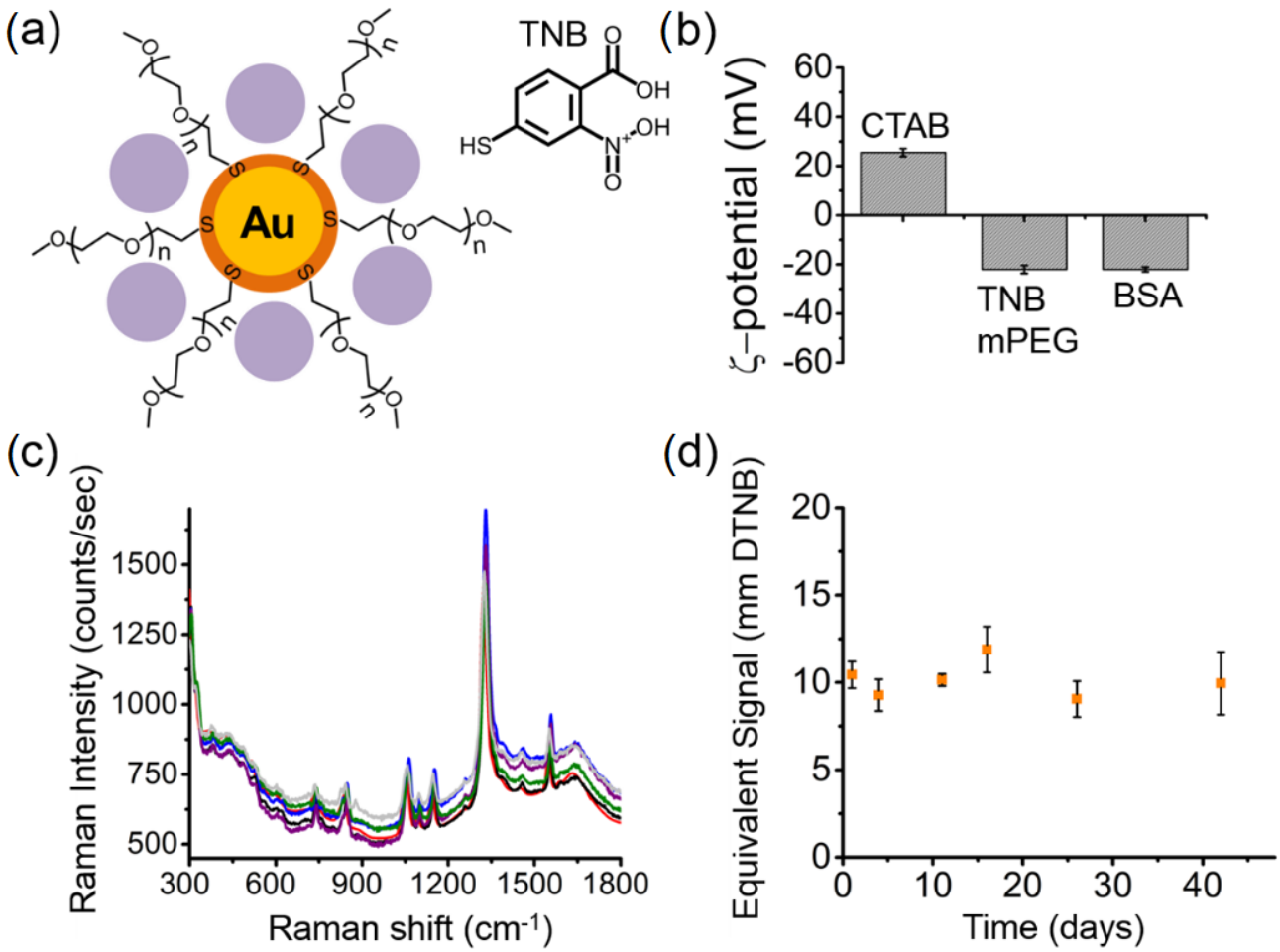

Figure 3.9. (a) Schematic of 5-thio-nitrobenzoic acid (orange shell) and methyl ether poly(ethylene glycol) thiol (TNB-PEG) coated nanoparticles with adsorbed BSA (purple spheres). (b) ζ-potential measurements of each synthetic step. (c) Representative Raman spectra of TNB-PEG coated nanoparticle. Day 1, black; Day 4, red; Day 11, blue; Day 16, purple; Day 26, green; Day 42, grey. (d) Spontaneous Raman equivalent of TNB-PEG nanoparticles in terms of mM of DTNB.

thiolate bond, TNB-PEG coated nanoparticles were less susceptible to signal loss over time. As expected, the storage considerations for thiolated Raman reporters are less crucial than LbL nanostructures.

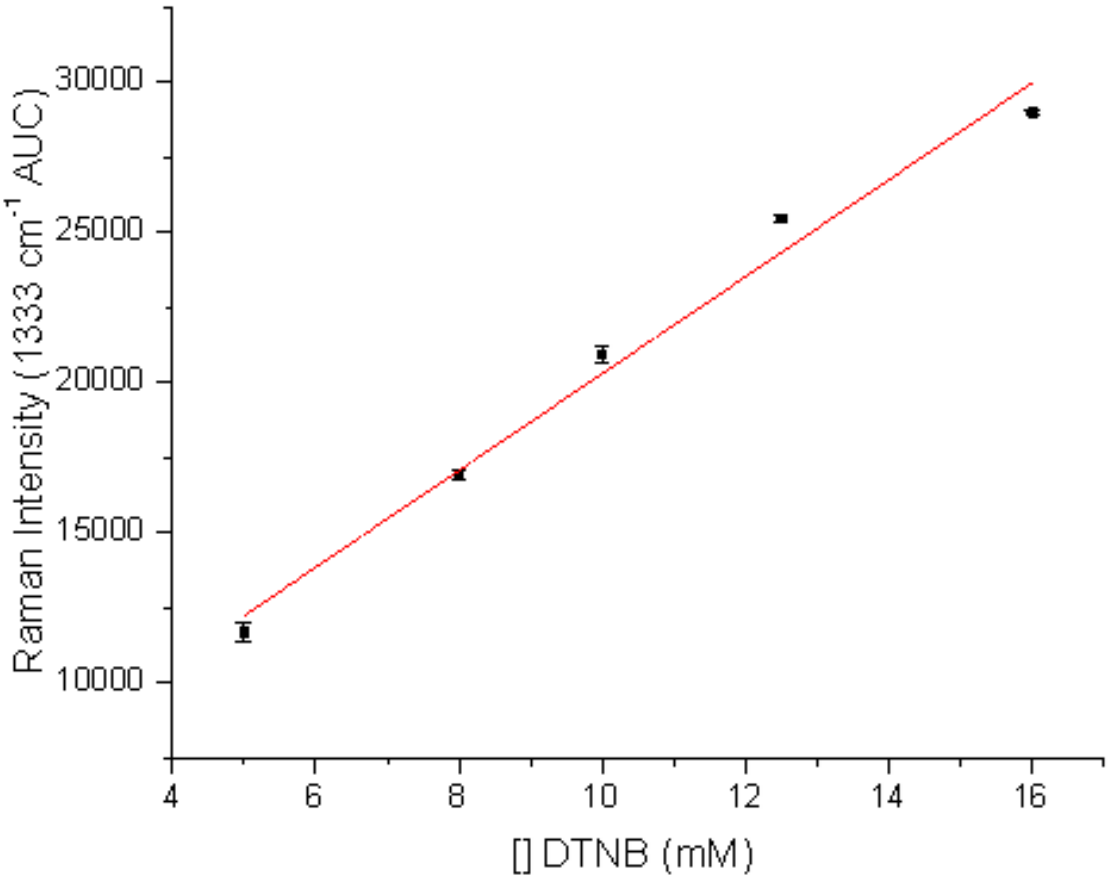

Figure 3.10. Spontaneous Raman calibration curve of aqueous DTNB from 5 – 16 mM. The equation of the line was determined through linear regression to be: $y = 1612x + 4179$.

3.4 Conclusion

Careful consideration of electrostatically encapsulated optical reporter molecules for SERS nanoprobes is critical. In this chapter, we investigated the signal stability of SERS nanoprobes using polyelectrolyte LbL wrapping to encapsulate reporter molecules. We found that polyelectrolyte-wrapped samples stored at colder temperatures (4 °C) are more likely to maintain their spectral signature. Samples stored at room temperature and 37 °C were more likely to exhibit strong diffusion effects over the course of 5 weeks. A diffusion coefficient of 10^{-18} cm^2/s was derived by fitting our experimental data to a diffusion/electromagnetic enhancement model. To overcome signal degradation of SERS nanoprobes, chemical

crosslinking of a polyelectrolyte-wrapped nanoparticle is sufficient. We find that storage of crosslinked samples at 4 °C is best for long-term usage. Alternatively, stronger covalent gold-thiolate bonds also prevent reporter molecule diffusion; however, thiolated molecules are typically limited in availability and expensive.

3.5 References

(1) Sharma, B.; Frontiera, R. R.; Henry, A.-I.; Ringe, E.; Van Duyne, R. P. SERS: Materials, Applications, and the Future. *Mater. Today* **2012**, *15*, 16–25.
(2) Lohse, S. E.; Murphy, C. J. The Quest for Shape Control: A History of Gold Nanorod Synthesis. *Chem. Mater.* **2013**, *25*, 1250–1261.
(3) Moskovits, M. Persistent Misconceptions Regarding SERS. *Phys. Chem. Chem. Phys.* **2013**, *15*, 5301–5311.
(4) Huang, J.; Jackson, K. S.; Murphy, C. J. Polyelectrolyte Wrapping Layers Control Rates of Photothermal Molecular Release from Gold Nanorods. *Nano Lett.* **2012**, *12*, 2982–2987.
(5) Fakhrullin, R. F.; Lvov, Y. M. "Face-Lifting" and "Make-Up" for Microorganisms: Layer-by-Layer Polyelectrolyte Nanocoating. *ACS Nano* **2012**, *6*, 4557–4564.
(6) Hammond, P. T. Engineering Materials Layer-by-Layer: Challenges and Opportunities in Multilayer Assembly. *AIChE J.* **2011**, *57*, 2928–2940.
(7) Gole, A.; Murphy, C. J. Polyelectrolyte-Coated Gold Nanorods: Synthesis, Characterization and Immobilization. *Chem. Mater.* **2005**, *17*, 1325–1330.
(8) Alkilany, A. M.; Thompson, L. B.; Murphy, C. J. Polyelectrolyte Coating Provides a Facile Route to Suspend Gold Nanorods in Polar Organic Solvents and Hydrophobic Polymers. *ACS Appl. Mater. Interfaces* **2010**, *2*, 3417–3421.
(9) Fernández-López, C.; Mateo-Mateo, C.; Álvarez-Puebla, R. A.; Pérez-Juste, J.; Pastoriza-Santos, I.; Liz-Marzán, L. M. Highly Controlled Silica Coating of PEG-Capped Metal Nanoparticles and Preparation of SERS-Encoded Particles. *Langmuir* **2009**, *25*, 13894–13899.
(10) Doering, W. E.; Nie, S. Spectroscopic Tags Using Dye-Embedded Nanoparticles and Surface-Enhanced Raman Scattering. *Anal. Chem.* **2003**, *75*, 6171–6176.
(11) Sivapalan, S. T.; Devetter, B. M.; Yang, T. K.; van Dijk, T.; Schulmerich, M. V.; Carney, P. S.; Bhargava, R.; Murphy, C. J. Off-Resonance Surface-Enhanced Raman Spectroscopy from Gold Nanorod Suspensions as a Function of Aspect Ratio: Not What We Thought. *ACS Nano* **2013**, *7*, 2099–2105.
(12) Sivapalan, S. T.; DeVetter, B. M.; Yang, T. K.; Schulmerich, M. V.; Bhargava, R.; Murphy, C. J. Surface-Enhanced Raman Spectroscopy of Polyelectrolyte-Wrapped Gold Nanoparticles in Colloidal Suspension. *J. Phys. Chem. C* **2013**, *117*, 10677–10682.
(13) Hilderbrand, S. A.; Weissleder, R. Near-Infrared Fluorescence: Application to in Vivo Molecular Imaging. *Curr. Opin. Chem. Biol.* **2010**, *14*, 71–79.
(14) Helmchen, F.; Denk, W. Deep Tissue Two-Photon Microscopy. *Nat. Methods* **2005**, *2*, 932–940.

(15) van Dijk, T.; Sivapalan, S. T.; DeVetter, B. M.; Yang, T. K.; Schulmerich, M. V.; Murphy, C. J.; Bhargava, R.; Carney, P. S. Competition between Extinction and Enhancement in Surface-Enhanced Raman Spectroscopy. *J. Phys. Chem. Lett.* **2013**, *4*, 1193–1196.
(16) Wu, X.; Ming, T.; Wang, X.; Wang, P.; Wang, J.; Chen, J. High-Photoluminescence-Yield Gold Nanocubes: For Cell Imaging and Photothermal Therapy. *ACS Nano* **2009**, *4*, 113–120.
(17) Tenzer, S.; Docter, D.; Kuharev, J.; Musyanovych, A.; Fetz, V.; Hecht, R.; Schlenk, F.; Fischer, D.; Kiouptsi, K.; Reinhardt, C.; et al. Rapid Formation of Plasma Protein Corona Critically Affects Nanoparticle Pathophysiology. *Nat. Nanotechnol.* **2013**, *8*, 772–781.
(18) Le Ru, E. C.; Etchegoin, P. G. Quantifying SERS Enhancements. *MRS Bull.* **2013**, *38*, 631–640.
(19) Xu, H.; Aizpurua, J.; Käll, M.; Apell, P. Electromagnetic Contributions to Single-Molecule Sensitivity in Surface-Enhanced Raman Scattering. *Phys. Rev. E* **2000**, *62*, 4318–4324.
(20) Naujok, R. R.; Duevel, R. V.; Corn, R. M. Fluorescence and Fourier Transform Surface-Enhanced Raman Scattering Measurements of Methylene Blue Adsorbed onto a Sulfur-Modified Gold Electrode. *Langmuir* **1993**, *9*, 1771–1774.
(21) Le Ru, E. C.; Etchegoin, P. G. *Principles of Surface-Enhanced Raman Spectroscopy and Related Plasmonic Effects*; Elsevier: Boston, 2009.
(22) Chung, A. J.; Rubner, M. F. Methods of Loading and Releasing Low Molecular Weight Cationic Molecules in Weak Polyelectrolyte Multilayer Films. *Langmuir* **2002**, *18*, 1176–1183.
(23) Klitzing, R. v.; Möhwald, H. A Realistic Diffusion Model for Ultrathin Polyelectrolyte Films. *Macromolecules* **1996**, *29*, 6901–6906.
(24) Burke, S. E.; Barrett, C. J. pH-Dependent Loading and Release Behavior of Small Hydrophilic Molecules in Weak Polyelectrolyte Multilayer Films. *Macromolecules* **2004**, *37*, 5375–5384.
(25) Berg, M. C.; Zhai, L.; Cohen, R. E.; Rubner, M. F. Controlled Drug Release from Porous Polyelectrolyte Multilayers. *Biomacromolecules* **2006**, *7*, 357–364.
(26) Kim, S.; Kim, Y.; Ko, Y.; Cho, J. Electrochemical Sensors Based on Porous Nanocomposite Films with Weak Polyelectrolyte-Stabilized Gold Nanoparticles. *J. Mater. Chem.* **2011**, *21*, 8008–8013.
(27) Fery, A.; Schöler, B.; Cassagneau, T.; Caruso, F. Nanoporous Thin Films Formed by Salt-Induced Structural Changes in Multilayers of Poly(acrylic Acid) and Poly(allylamine). *Langmuir* **2001**, *17*, 3779–3783.
(28) Häkkinen, H. The Gold-Sulfur Interface at the Nanoscale. *Nat. Chem.* **2012**, *4*, 443–455.
(29) Varsányi, G. *Assignments for Vibrational Spectra of Seven Hundred Benzene Derivatives*; Wiley, 1974.

CHAPTER 4

MEASURING BINDING KINETICS OF AROMATIC THIOLATED MOLECULES WITH NANOPARTICLES *VIA* SURFACE-ENHANCED RAMAN SPECTROSCOPY

4.1 Introduction

Precise control over nanoscale features has produced many exciting advances in electronic, photonic, and biomedical devices over the last two decades.[1–3] Integral to these advances has been the realization that control over the surface chemistries of both macroscopic substrates and nanoscopic probes is crucial for the development of new and existing nanotechnologies. Molecules containing thiol (R-SH) moieties are particularly well-suited for engineering surface chemistries due to the covalent nature of metal-sulfur bonds (~130 kJ/mol for Au–S).[4] Researchers have demonstrated thiol's ubiquitous nature through applications such as the preparation and functionalization of plasmonic nanocrystals,[5] semiconductor quantum dots,[6] and self-assembled monolayers.[7] Rigorous investigation of the metal-thiolate bond is essential for the development of nanotechnologies with unprecedented surface control.

For biological sensing applications, gold nanoparticles are commonly synthesized in aqueous wet chemistry with stabilizing ligands including polyvinylpyrrolidone (PVP), citrate, cetyltrimethylammonium bromide (CTAB), and cetyltrimethylammonium chloride (CTAC). Most notably, the surfactant CTAB can have growth directing properties leading to the formation of anisotropic nanostructures such as gold nanorods and gold nanoplates.[8] The relative strength of the bond between the stabilizing ligands and the gold surface affects our ability to functionalize nanoparticles for biological sensing applications.

In highly ionic tissue microenvironments consisting of proteins and varying degrees of pH, it is especially important to have complete control over the probe's surface chemistry. For example, nanoprobes are often coated in thiolated polyethylene glycol in order to increase circulation time and biocompatibility by partially masking probes from proteins found in biological tissues and serum.[5] Bifunctionalized polyethylene glycol molecules with reactive functional groups, such as carboxylic acid, are frequently coupled to proteins, aptamers, or other biomolecules for targeting applications.[9,10] Unlike electrostatically bound reporter molecules, covalently bound reporter molecules are not susceptible to diffusion and are significantly more reliable for long-term biological studies. In a similar vein, the efficiency of ligand exchange of thiolated polyethylene glycol is heavily dependent on the original stabilizing ligand,[11] with CTAB being recognized as the most difficult ligand to replace. Therefore, consideration of the as-synthesized stabilizing ligand for successful ligand exchange is essential.

Self-assembled monolayers (SAMs) were one of the earliest and most common techniques for controlling surface chemistry and fabricating nanopatterned substrates. SAMs form when free gas or liquid phase molecules spontaneously arrange as they adsorb to a surface. A popular choice for SAMs is alkanethiols; alkanethiols contain a thiol head group, which readily chemisorbs to gold, and an alkyl chain. The strength of the metal-thiolate bond makes thiol bearing molecules invaluable for applications involving metallic substrates. The structure and kinetics of alkanethiol SAM formation have been heavily characterized using diverse surface analysis techniques such as scanning tunneling microscopy, x-ray diffraction, atomic force microscopy, vibrational spectroscopy, and theoretically *via* density functional theory.[7,12] It is well established that alkanethiol SAM formation essentially follows the Langmuir isotherm.[13–15]

The Langmuir isotherm assumes monolayer coverage, noninteracting adsorbed molecular species, uniform binding sites, and may be described by:

$$\theta = \frac{KC}{1 + KC} \tag{4.1}$$

where K is a constant, C is the concentration of the adsorbed species, and θ is fractional surface coverage. Understanding the kinetics of metal-thiolate bond formation is essential for rapidly manufacturing SAMs. To date, the majority of studies investigating thiol kinetics have focused on flat macroscopic substrate SAM formation.[12–14] Advances in the control over surface morphology of colloidal nanoparticles, however, has brought about renewed interest in thiolate bond formation as applied to nanostructures.

In this chapter, we investigated the kinetics of gold-thiolate bond formation on colloidal gold nanoparticles with the intention of elucidating the design parameters necessary to successfully prepare optical nanoprobes for biological sensing applications. The ligand exchange process was characterized by monitoring the surface-enhanced Raman scattering (SERS) intensity of vibrational modes corresponding to specific thiolated Raman-active molecules. Whereas other techniques such as UV/vis absorption spectroscopy have been used to monitor time-dependent changes in the localized surface plasmon resonance during nanoparticle aggregation and gold-thiolate bond formation,[16] Raman spectroscopy's inherent chemical specificity allowed us to monitor both the changing surface chemistry and structural properties of the dynamically forming ligand shell. In order to prepare biologically relevant nanoprobes, we ensured that all Raman-active molecules were water soluble to maintain stability of the nanoparticles. Our results were compared with a theoretical model that predicted the effect of ensemble absorption and scattering of light during propagation through a turbid media.

SERS is a highly sensitive, chemically specific sensing modality that is well suited for studying the kinetics of gold-thiolate formation on nanoparticles. To date, however, only a few studies have specifically investigated the kinetics of ligand exchange on gold nanoparticles using SERS. One such study investigated ligand exchange using citrate-stabilized gold nanoparticles dispersed in dimethylformamide (DMF).[17] This study primarily used reporter molecules with limited water solubility, making aggregation effects a larger concern. Additionally, the toxicity of DMF and the extra purification steps required to remove DMF makes these probes undesirable for rapid manufacturing. A different research group used time-dependent SERS and a ratiometric technique to quantify ligand exchange on simultaneously aggregating gold nanoparticles.[18] This technique, however, relies on the generation of hot-spots, which can lead to unreproducible results due to uncertainty in the position of the molecular analyte with respect to the metal-metal junction. Additionally, it is impossible to fully decouple ligand exchange kinetics from aggregation kinetics using this approach. We also discuss ligand exchange kinetics and the design parameters necessary to prepare unaggregated, water soluble gold nanoparticles for biological sensing applications.

4.2 Theory

The chemisorption of alkanethiol molecules to gold nanoparticles generally follows a first-order Langmuir adsorption model and is described by the following:[14]

$$\theta(t - t_0) = A(1 - e^{-k_{obs}(t-t_0)}) \tag{4.2}$$

where θ is the fractional surface coverage, A is a constant dependent on the association or dissociation constants of the adsorption reaction, k_{obs} is the rate constant, and t_0 is a time delay factor added to account for the time required to mix the solution after the introduction of Raman

reporter molecules. We assumed the binding characteristics of gold-thiolate bonds are similar in both aromatic thiolated reporter molecules and alkanethiol molecules such that the first-order Langmuir adsorption model will appropriately describe chemisorption during ligand exchange. Furthermore, only colloidal nanoparticle measurements performed in a backscattering collection geometry were considered, as illustrated by Figure 4.1.

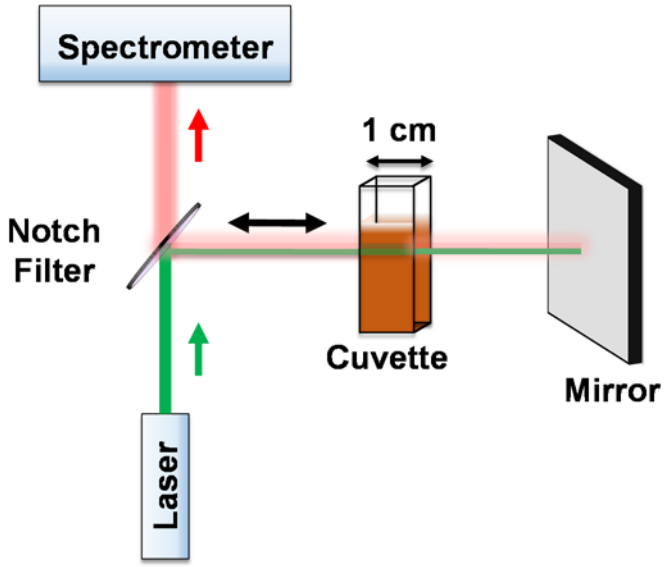

Figure 4.1. Schematic of backscattering collection geometry using a 1 cm path length cuvette. Raman scattered light was directed to a grating spectrometer after a holographic notch filter removed undesired Rayleigh scattered light.

The kinetics of gold-thiolate bond formation were monitored using SERS. SERS, as has been discussed extensively,[19] operates on two distinct enhancement mechanisms: chemical enhancement and electromagnetic enhancement. Chemical enhancement is a weak effect and likely arises from a combination of resonances between the metal-molecule complex, deformation in the molecular polarizability, and electron charge transfer between molecules and the plasmonic surface.[20,21] In contrast, the stronger electromagnetic enhancement effect originates from the collective oscillation of the electron gas under resonant excitation. As a

limiting case, we only consider electromagnetic enhancement because it is a more useful design parameter and is several orders of magnitude stronger than chemical enhancement.

A selection rule for Raman spectroscopy is that the molecular polarizability must temporally deform or distort under excitation. The intensity of Raman scattered light may be described by three multiplicative terms. First, for molecular ensembles, the Raman scattering intensity is related to the number of molecules *N* present in the sampling volume and a factor $|\chi|^2$ where χ is the susceptibility of individual molecules. Because the susceptibility described here is related to the first-order Taylor expansion of molecular polarizability, the selection rule is satisfied. To accurately describe the Raman scattering intensity of molecules bound near the surface of a single plasmonic nanoparticle, a second term called the electromagnetic enhancement $G(\omega,\omega_0)$ is necessary. Here, ω corresponds to the Stokes shifted frequency of scattered light and ω_0 corresponds to the excitation frequency. The third and final term is crucial for plasmonic nanoparticle ensembles and is proportional to the Beer-Lambert law, which describes the exponential decay of light due to absorption and scattering (extinction) in turbid media. Therefore, the scattering intensity $I(\omega,\omega_0)$ as it propagates through a sample of thickness *b* may be defined as the following:[22,23]

$$I(\omega,\omega_0) = N|\chi|^2 G(\omega,\omega_0)\int_0^b dz\, e^{-zc[\varepsilon(\omega)+\varepsilon(\omega_0)]} \tag{4.3}$$

where *c* is the nanoparticle concentration and ε is the corresponding molar extinction coefficient.

To calculate the intensity of Raman scattering and kinetics of chemisorption, we first assumed spherical gold nanoparticles under the quasi-static approximation. Therefore, the electromagnetic enhancement is given by:[24]

$$G(\omega,\omega_0) = \left|\left[1+2g(\omega)\right]\left[1+2g(\omega_0)\right]\right|^2 \tag{4.4}$$

where g is the Clausius-Mossotti relation, $g=(m^2-1)/(m^2+2)$, and m is the ratio of the refractive index of gold to the refractive index of the surrounding media (water, n_0 = 1.33). Frequency-dependent optical constants for gold were obtained from Johnson and Christy.[25] The extinction cross section was calculated from the following:[26]

$$C_{\text{ext}} = 4k\pi a^3 \,\text{Im}\left\{\frac{m^2-1}{m^2+2}\right\} + \frac{8}{3}(ka)^4 \pi a^2 \left|\frac{m^2-1}{m^2+2}\right|^2 \tag{4.5}$$

where a is the radius of the nanoparticle and k is the wavevector ($k=2\pi n_0/\lambda_{ex}$) of the excitation light in the surrounding media.

We have previously demonstrated the importance of the Beer-Lambert law in calculating the Raman scattering intensity of nanoparticle ensembles.[22] Although the spontaneous Raman scattering intensity is intrinsically linear with respect to nanoparticle concentration, we have shown a nonlinear response due to optical extinction at higher nanoparticle concentrations. Incorporating the Beer-Lambert law with electromagnetic enhancement results in the following expression:[22]

$$R(\omega,\omega_0,c) = R_0 G(\omega,\omega_0)\frac{1-e^{-bn_0c[\varepsilon(\omega)+\varepsilon(\omega_0)]}}{n_0\varepsilon(\omega)+n_0\varepsilon(\omega_0)} \tag{4.6}$$

where R_0 is a constant dependent on the laser beam profile and the molecular Raman scattering cross section (*i.e.*, $N|\chi|^2$). From Equation 4.6, it is apparent that nanoparticle concentration is responsible for the extinction of $R(\omega,\omega_0,c)$ and thus the nonlinear dependence is clear. It is

possible, as a result, to optimize the concentration of nanoparticles in solution to obtain a maximal signal based on the extinction coefficient and path length.

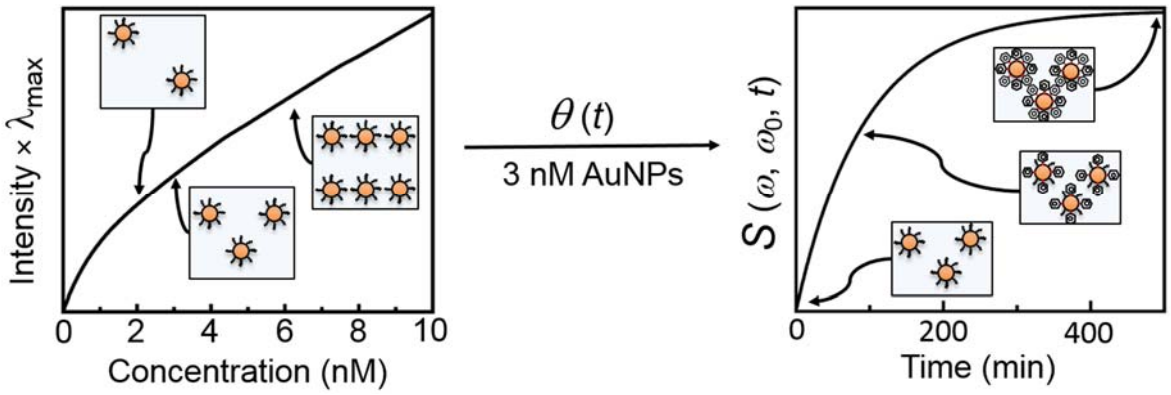

Figure 4.2. As illustrated by the Beer-Lambert law, the intensity of propagated light through turbid media decays exponentially. This intensity is a function of nanoparticle concentration as described by $R(\omega, \omega_0, c)$. Variation of (Intensity × λ_{max}) with nanoparticle concentration is depicted on the left. A threshold concentration (3 nM and path length b = 1 cm) of nanoparticles was chosen as an idealized model. The number of adsorbed molecules $p(t)$ varied according to the first-order adsorption model $\theta(t)$ (k_{obs} = 0.01 min^{-1}, t_0 = 0 min) and was applied to the function $S(\omega,\omega_0,t)$, as shown on the right.

Ligand exchange kinetics may be described by modifying $R(\omega,\omega_0,t)$ to account for the adsorption of Raman-active reporter molecules as a function of time.[23] For non-resonant reporter molecules such as 2-thio-5-nitrobenzoic acid (TNB), the molar extinction (13,600 M^{-1}cm^{-1} at 412 nm)[27] is negligible in comparison with the molar extinction of gold nanoparticles (10^9 M^{-1}cm^{-1} at ~525 nm), such that we may neglect the extinction caused by these molecules even when they are added in molar excess. Thus, the kinetic equation to model the adsorption of molecules to colloidal nanoparticles with a fixed nanoparticle concentration is given by:[23]

$$S(\omega,\omega_0,t) = S_0 G(\omega,\omega_0)\frac{p(t)}{c}\frac{1-e^{-bn_0c[\varepsilon(\omega)+\varepsilon(\omega_0)]}}{n_0\varepsilon(\omega)+n_0\varepsilon(\omega_0)} \tag{4.7}$$

where S_0 is a constant dependent on the laser beam profile and molecular Raman scattering cross section and $p(t)$ is the concentration of bound molecules. The time dependence of $S(\omega,\omega_0,t)$ was calculated by applying a first-order Langmuir adsorption model with parameters $k_{obs} = 0.01$ min^{-1} and $t_0 = 0$ min. In Figure 4.2, the intensity grows as a function of time for a fixed nanoparticle concentration of 3 nM. The effect described by $R(\omega,\omega_0,c)$ is a nonlinear response with nanoparticle concentration as predicted by Beer's law. When the turbidity of a solution (nanoparticle concentration) increases, light propagating through that solution decays exponentially. In contrast, for a constant nanoparticle concentration, the time-varying adsorption of weakly scattering molecules will have a linear response as described by $S(\omega,\omega_0,t)$. This model provides confidence that it is possible to monitor the linear response of gold-thiolate bond formation in colloidal suspension.

4.3 Results and discussion

We first synthesized 18 nm gold nanoparticles using the boiling citrate method. Monodispersity, shape, and size were verified through a combination of transmission electron microscopy (TEM), UV/vis spectroscopy, and dynamic light scattering (DLS) measurements. Citrate-stabilized gold nanoparticles are particularly attractive because of the relative ease in which the citrate ligands may be exchanged. Ellman's reagent or 5,5′-dithiobis-(2-nitrobenzoic acid) (DTNB) is a common Raman-active reporter molecule. DTNB's disulfide bond readily cleaves and forms 2-thio-5-nitrobenzoic acid (TNB) when dissolved in water at pH ~ 7. This may be may monitored by measuring its absorbance at 412 nm.[28] As shown in Figure 4.3, ligand exchange was initiated by the introduction of aqueous TNB into a solution of gold nanoparticles.

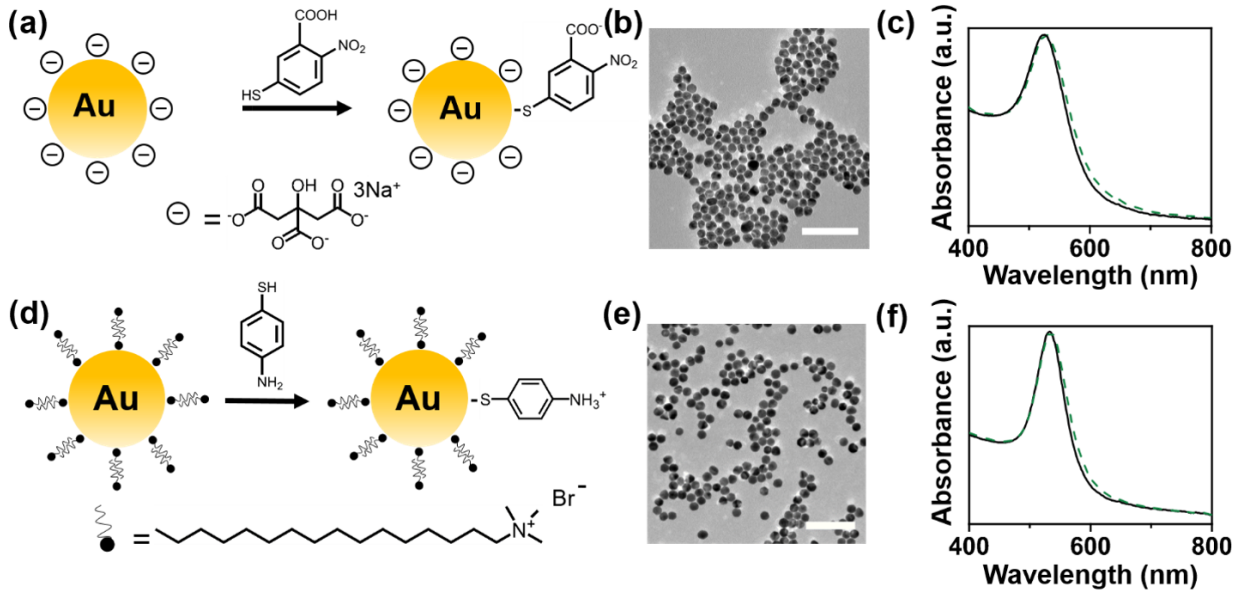

Figure 4.3. Schematic of the ligand exchange process. (a) Ligand exchange of citrate with TNB and (b) ligand exchange of CTAB with 4-ATP. Transmission electron micrograph of (c) citrate-stabilized (scale bar: 100 nm) and (d) CTAB-stabilized (scale bar: 200 nm) nanoparticles. UV/vis spectra of (e) citrate-stabilized and (f) CTAB-stabilized nanoparticles before (solid line) and 2 weeks after ligand exchange (dashed line).

After ligand exchange was complete, each sample was stored at room temperature to ensure stability. Figure 4.3 shows that there was no evidence of aggregation or coalescence. Nanoparticle stability was further assessed by measuring ζ-potential and DLS. Before ligand exchange, the citrate-stabilized nanoparticles had a ζ-potential of -29.0 ± 6.5 mV. After ligand exchange, the nanoparticles had a ζ-potential of -13.0 ± 2.1 mV, indicating electrostatic stabilization in suspension. DLS data is shown in Figure 4.4.

Ligand exchange of 4-aminothiophenol (4-ATP) molecules was also performed on 40 nm gold nanospheres stabilized with CTAB. Whereas CTAB is notoriously difficult to remove from gold nanorods, CTAB is readily removed from the highly faceted gold nanosphere surface.

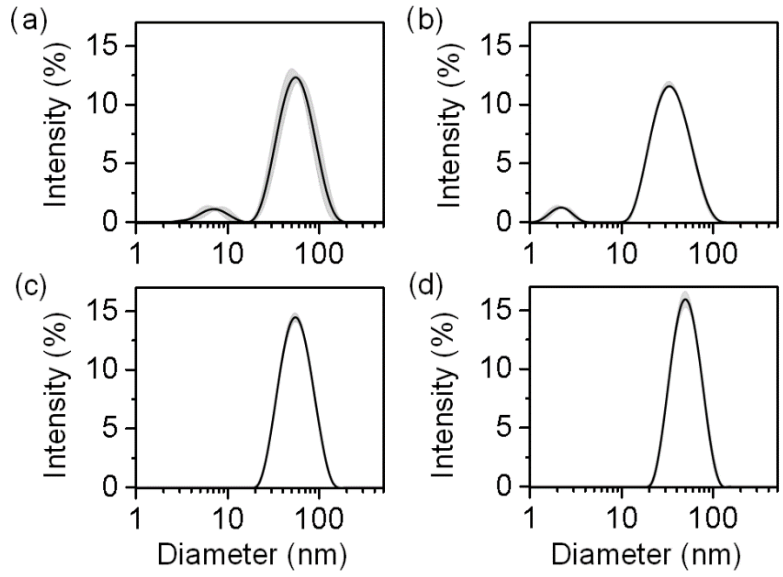

Figure 4.4. Dynamic light scattering (DLS) of (a) citrate-stabilized gold nanoparticles, (b) gold nanoparticles with DTNB stored for 2 weeks at room temperature, (c) gold nanoparticles stabilized with CTAB, and (d) gold nanoparticles replaced with 4-ATP and stored for 2 weeks at room temperature. Shaded area corresponds to the standard deviation of the measurements.

We verified that the nanoparticles were stable before and after ligand exchange using UV/vis spectroscopy and ζ-potential/DLS. The ζ-potential before ligand exchange was 40.4 ± 1.1 mV and the ζ -potential after ligand exchange was 41.1 ± 2.9 mV. Likewise, the DLS data showed no significant change in the size distribution of nanoparticles before and after exchange.

The kinetics of gold-thiolate bond formation were measured after introducing Raman-active reporter molecules TNB and 4-ATP into citrate-stabilized and CTAB-stabilized gold nanoparticle suspensions, respectively. Before introduction of reporter molecules, we adjusted the nanoparticle concentration such that the ratio of the number of available binding sites to the number of molecules was equivalent for both TNB/citrate and 4-ATP/CTAB solutions. Coverage density calculations were based on the assumption that TNB has a molecular footprint of 0.26 nm^2/molecule and 4-ATP has a molecular footprint of 0.20 nm^2/molecule.[29,30] Molecules

were added in molar excess such that approximately 10^5 – 10^6 molecules per binding site were available before chemisorption took place.

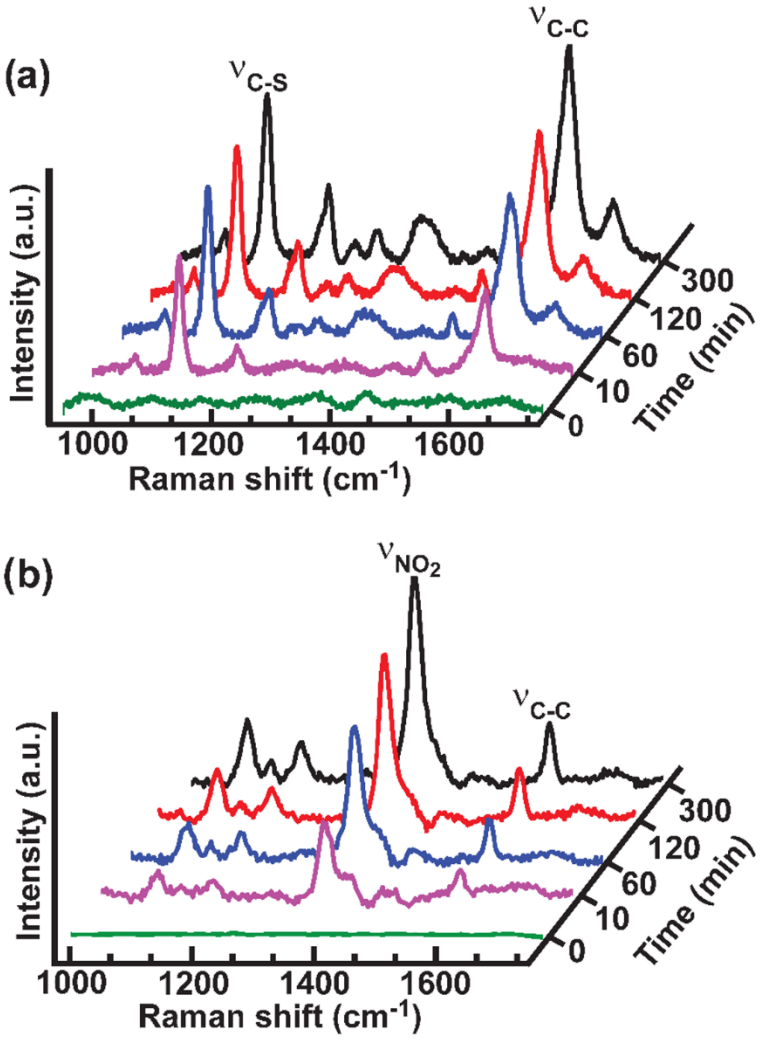

Figure 4.5. Kinetic SERS spectra of representative samples illustrating the growth of vibrational modes during ligand exchange of (a) CTAB with 4-ATP and (b) citrate with TNB. Reporter molecules were added immediately after t = 0 min.

The inherent chemical specificity of Raman spectroscopy allows simultaneous monitoring of the growth of multiple vibrational modes during ligand exchange. In Figure 4.5, the kinetic SERS spectra of 4-ATP chemisorbed to gold nanoparticles is shown. Although CTAB-stabilized gold nanoparticles have an Au-Br band at 174 cm^{-1},[31] it was not possible to

quantify the desorption of CTAB from spherical gold nanoparticles because the band immediately disappeared after introduction of 4-ATP. In contrast, we were able to monitor partial desorption of CTAB from gold nanorods when using a 785 nm excitation laser; however, this effect is likely due to the higher density and affinity for CTAB on the nanorod surface rather than a wavelength dependent effect. The exceedingly weak signature of the Au–S bands at 240 and 480 cm^{-1} in colloidal measurements[32] made it challenging to directly measure the formation of gold-thiolate bonds using SERS. Instead, we monitored the time-dependent growth of stronger vibrational modes, which is correlated to the formation of gold-thiolate bonds as the molecules interact with the gold nanoparticle surface and displace electrostatically bound stabilizing ligands.

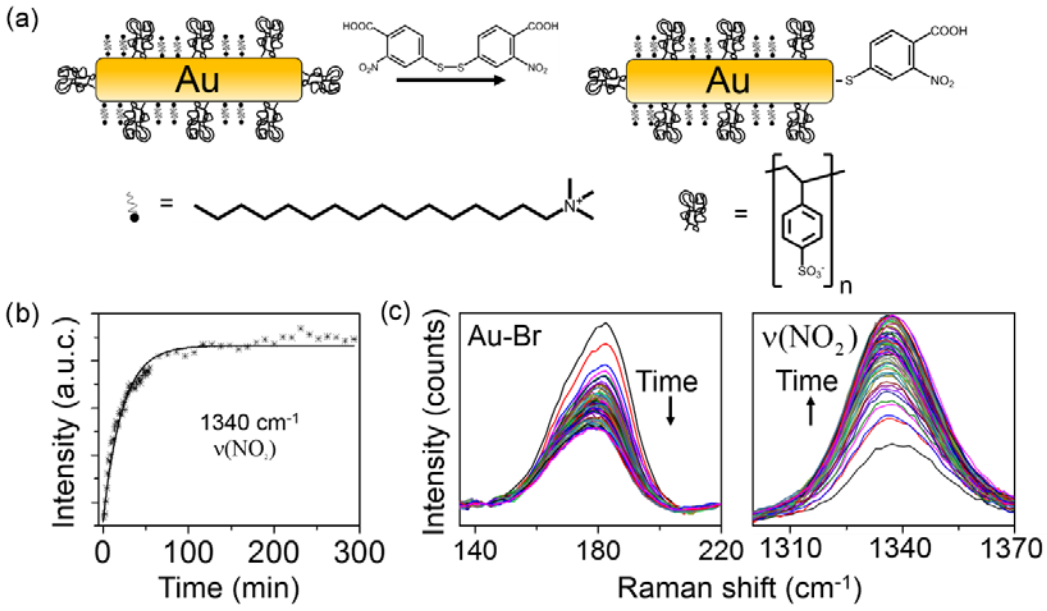

Figure 4.6. (a) Schematic of ligand exchange of CTAB and poly(styrene sulfonate) (PSS) with TNB on gold nanorods. (b) First-order Langmuir adsorption model fit to the ν(NO2) mode. (c) Decay of the ν(Au-Br) mode (left) and growth of the ν(NO2) mode (right) during ligand exchange. The excitation wavelength was 785 nm.

We found that it was necessary to perform additional steps on CTAB-stabilized gold

nanorods in order to have successful ligand exchange occur. In order for successful ligand exchange to occur on gold nanorods, it was necessary to remove additional CTAB using an iterative process of washing the nanorods in chloroform, adding poly(styrene sulfonate) (PSS), and centrifugation. We were unable to completely remove all CTAB ligands, as shown in Figure 4.6.

Previously, we demonstrated that SERS intensity varies nonlinearly with concentrations in colloidal suspensions of nanoparticles due to the competing mechanisms of optical extinction and electromagnetic enhancement.[22] Equation 4.7 shows that the time-varying molecular adsorption component, $p(t)$, linearly varies with intensity. To verify this prediction, we performed ligand exchange experiments and measured the growth of vibrational modes as a function of time. As shown in Figure 4.7, the relative growth of bands were measured by computing an intensity ratio (area of band immediately after reporter molecule injection to area of band at the end of the measurement). We found the behavior of each band to be consistent across samples. For example, the non-fundamental mixed vibrational mode ν(C-C) + β(C-H) at 1357 cm^{-1} grew nearly twice that of the ν(C-S) and ν(C-C) vibrational modes. Certain modes, especially ν(C-S), were mostly insensitive to the number of molecules adsorbed to the nanoparticles (intensity ratio of 1.53 $\pm$ 0.22), likely because this mode has an intrinsically large Raman scattering cross section and how the molecules orient themselves with respect to the surface.

Our results indicate that the chemisorption of TNB and 4-ATP may accurately be described by the first-order Langmuir adsorption model. Fitting of the experimental data to the first-order Langmuir adsorption model for the stretching modes ν(C-C) (for 4-ATP) and

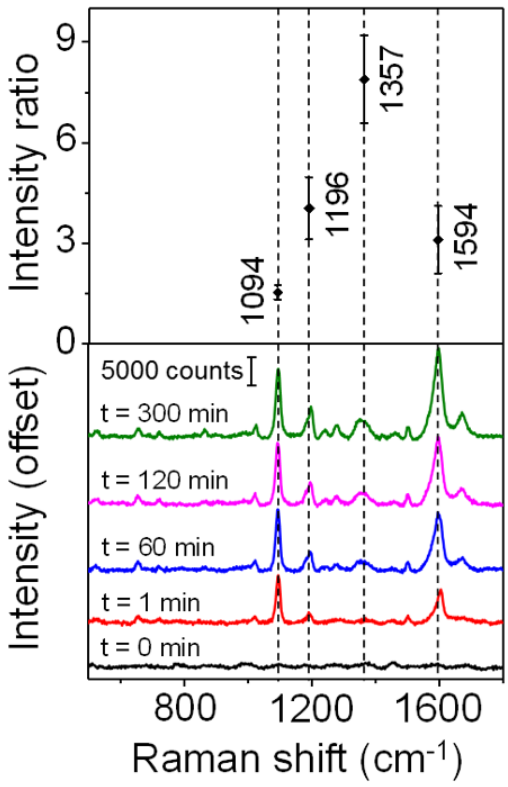

Figure 4.7. Kinetic SERS spectra of the exchange of 4-ATP (25 μL of 10 mM 4-ATP added to 2.0 mL of 3.0 nM gold nanoparticles) with CTAB on gold nanoparticles. The excitation wavelength was λ_{ex} = 633 nm with a 15 second integration time. An intensity ratio (area at *t* = 1 min to steady-state final area) was calculated to illustrate the growth of active vibrational modes. Error bars correspond to a 95% confidence interval.

$\nu(NO_2)$ (for TNB) are shown in Tables 4.1 and 4.2. We found that the average rate constant k_{obs} for both citrate and CTAB-stabilized gold nanoparticles was ~0.01 min^{-1} and, based on the data, we expect 90% surface coverage to be obtained approximately 4 hours after introduction of the Raman-active reporter molecules. Our results agree well with thiol adsorption kinetics on 3.3 nm gold nanoparticles as monitored by *in situ* time-resolved x-ray absorption fine structure (XAFS) where researchers measured a rate constant of 0.0132 min^{-1}.[33] They attributed a faster adsorption event during the first 20 minutes of measurement to adsorption on edges and corners. We did not

observe this event, possibly due to size differences between our nanoparticles and a lack differences in available defect sites. Other techniques such as x-ray photoelectron

Table 4.1. First-order Langmuir adsorption model fit to the Raman band corresponding to the vibrational stretching mode ν (NO_2) at 1340 cm^{-1}. Measurements were performed in a fused silica cuvette with 2 mL of nanoparticle solution and a concentration of 9.4 nM.

DTNB (10 mM)	k_{obs} (min^{-1})	A (a.u.)
25 μL	0.0117	1.10×10^5
50 μL	0.00725	7.56×10^4
100 μL	0.0141	1.46×10^5
200 μL	0.0129	1.87×10^5
Mean	0.011 ± 0.003	$1.3 \times 10^5 \pm 0.5 \times 10^5$

Table 4.2. First-order Langmuir adsorption model fit to the Raman band corresponding to the vibrational stretching mode ν (C-C) at 1594 cm^{-1}. Measurements were performed in a fused silica cuvette with 2 mL of nanoparticle solution and a concentration of 3.0 nM.

4-ATP (10 mM)	k_{obs} (min^{-1})	A (a.u.)
25 μL	0.0100	3.78×10^5
50 μL	0.0131	3.43×10^5
100 μL	0.0125	3.78×10^5
200 μL	0.0109	3.80×10^5
Mean	0.012 ± 0.002	$3.7 \times 10^5 \pm 0.2 \times 10^5$

spectroscopy (XPS) have been used to quantify the ligand exchange and density of thiolated molecules on gold nanoparticles surfaces.[34] For the purpose of monitoring the dynamics of nanoparticle surface chemistry in solution, XPS is not an ideal technique because it requires that the sample consist of dried nanoparticle films.

The surface-area-to-volume ratio plays a huge role in the efficiency and speed of gold-thiolate formation. One of the most intriguing aspects of nanoscience is the modified

characteristics of nanomaterials with respect to bulk materials. Researchers often observe that SAMs can take anywhere from 12 – 24 hours to form on clean, flat gold substrates.[35] For simplicity, if we assume a 1 μm^2 rectangular laser spot size illuminating a flat gold substrate, that same laser can probe 2000 nanoparticles in a 1 cm path length at a concentration of 3 nM. Given that the surface-area-to-volume ratio of the nanoparticles probed in our experiments is on the order of 10^8, we see that colloidal measurements offer huge advantages over interrogating flat surfaces. With this experimental setup, it also possible to probe fast kinetics. By reducing the

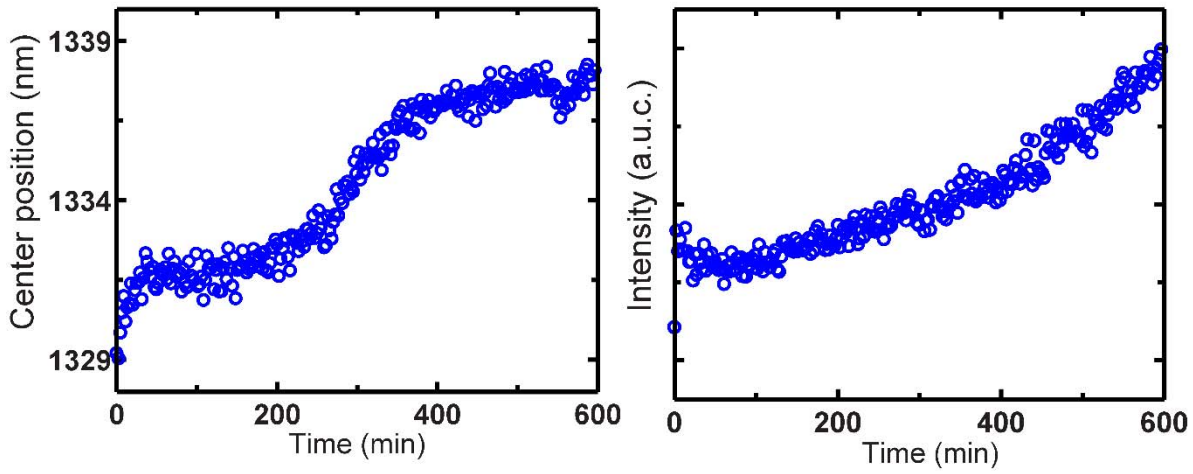

Figure 4.8. Kinetic data of DTNB (10 mM) added to a gold substrate. The substrate was cleaned with 3:1 concentrated 18 M H_2SO_4 to 30% H_2O_2 before addition. We observe that even after 600 minutes of acquisition time, the intensity (evaluated at $\nu(NO_2)$) is still growing.

integration time, we can probe fewer nanoparticles on a shorter time scale and investigate effects that occur rapidly. For example, we achieved an acceptable signal-to-noise ratio (~4.8) with an integration time of 50 milliseconds for a monolayer of TNB coated nanoparticles. With a 250 milliseconds integration time, we recorded a signal-to-noise ratio of ~15.7. We chose to investigate ensemble-averaged effects by probing large numbers of nanoparticles. Figure 4.8 illustrates the differences in colloidal *versus* macroscopic substrate measurements. We took a flat gold substrate added DTNB and showed that even after 10 hours of measurements SAM

formation was not complete and minimal structural and orientation information could be obtained. In contrast, the ensemble-averaged kinetic nanoparticle spectra offer a rich array of structural information.

Additionally, the rate constant k_{obs} being insensitive to changes in reporter molecule concentration in both cases indicates that chemisorption of the molecules in molar excess are not controlled by a diffusion-limited process. The invariance in the rate constant across multiple vibrational modes and the consistent demonstration of the Langmuir adsorption profile for each mode indicates that wavelength-dependent optical extinction during chemisorption is negligible. This result matches our theoretical prediction where the Stokes shifted frequency ω is independent of the adsorbed chemical species $p(t)$. The fact that k_{obs} is similar for both processes implies that the stabilizing ligands (citrate, CTAB) have roughly equivalent affinity for gold nanoparticles. Although it has been reported that CTAB ligands have a stronger affinity for gold than citrate ligands, we found that this is only true for gold nanorods, not nanospheres.[11] Gold nanorods present specific facets (*i.e.*, {110}) that more strongly bind to CTA^+ micelles,[31] whereas gold nanospheres are highly faceted in nature and do not have large areas of exclusively {110} surface sites. Conversely, we found that additional purification and preparation steps were necessary to perform ligand exchange on gold nanorods.

Bands of interest were fit to Lorentzian distributions for further analysis. As shown in Figure 4.9, we observed spectral shifting of the center band frequency during chemisorption. Our theoretical model suggests that the intensity $S(\omega,\omega_0,t)$ of each Raman band is shift invariant during this process. In other words, as molecules adsorb to the nanoparticle surface, the band is not expected to shift as a consequence of any optical effects. This result, therefore, suggests that center band frequency shifting is a result of deformation of the molecular polarizability of

adsorbed molecules *via* a metal-molecule complex. Certain bands such as ν(C-S) exhibit minimal band shifting. As shown in Figure 4.6a, the ν(C-C) mode shifted from 1601 cm^{-1} at t = 1 min to a steady-state Raman shift of 1594 cm^{-1}. Similarly, the mode ν(C-C) + β(C-H) began at 1376 cm^{-1} and reached a steady state of 1357 cm^{-1}.

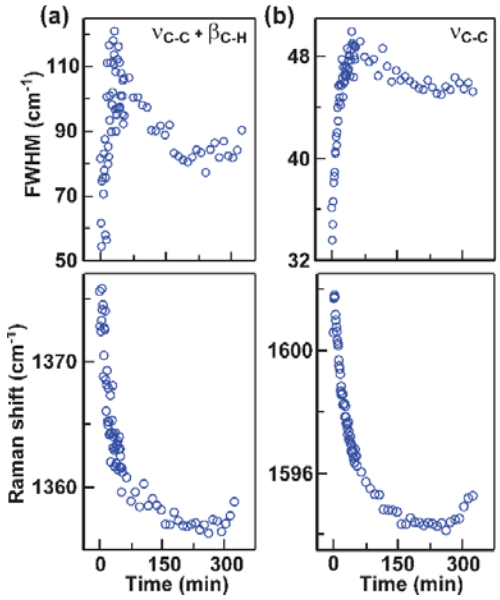

Figure 4.9. Time-dependent change in FWHM (top) and center band frequency (bottom) as determined by fitting to Lorentzian distributions. (a) Mixed mode ν(C-C) + β(C-H) and (b) fundamental mode ν(C-C). This data corresponds to a representative sample (final 4-ATP concentration: 125 μM).

During gold-thiolate bond formation, the full width at half maximum (FWHM) grows and saturates within the first hour of introducing reporter molecules. Subsequently, the FWHM narrows to an intermediate steady-state position. This indicates that the initial molecules are disordered and slowly become more ordered until the majority of stabilizing CTAB ligands have been replaced. This effect is analogous to the formation of a SAM substrate.[35] Blue-shifting of the center band frequency indicates a weakening bond. This is due to ligand-ligand, metal-molecule interactions, and orientation effects during monolayer formation. We are able to gain

much insight from this data regarding the state of the surface chemistry in the nanoparticle ensemble. The initial growth of Raman bands corresponds to molecular adsorption and eventually leads to chemisorption and reorientation of the molecular species on the nanoparticle surface. Because our data corresponds well to the first-order Langmuir adsorption model, we can conclude that the majority of signal arises from the interaction and adsorption of new molecular species rather than molecular reorientation. While molecular reorientation is an important effect, its contribution to the signal intensity is likely minimal, as indicated by our theoretical model where we only assume adsorption increases the signal. That being said, molecular reorientation causes, in part, the shifting we observe in the center band frequency of certain Raman modes. To fully explore the effects of molecular reorientation, new methods such as observing the kinetics of partially ligand exchanged nanoparticles and polarization measurements, beyond the scope of this report are necessary. To further analyze the meaning of blue-shifting during chemisorption, we compared unbound 4-ATP molecules with bound 4-ATP molecules chemisorbed to a SAM of gold nanoparticles.

A self-assembled monolayer of gold nanoparticles on a glass substrate was fabricated to compare the center band frequency of 4-ATP molecules chemisorbed to gold in colloidal suspension *versus* dried substrate. This comparison allows to us monitor the binding strength of the respective thiolated molecules in solution as compared to dried substrates. Treatment of the vibrations of molecules as harmonic oscillators shows that longer Raman shifts correspond to more tightly bound molecules. On dried substrate, ν(C-C) + β(C-H) was not active; however, it was possible to compare ν(C-S) and ν(C-C), as shown in Figure 4.10. The ν(C-S) mode is largely shift invariant and insensitive to the number of bound molecules. Therefore, it is an excellent mode to obtain information about the state of binding. On gold nanoparticles, ν(C-S)

was blue-shifted from that of unbound 4-ATP molecules but red-shifted from the SAM configuration. This indicates that the C-S bond strength in colloidal gold nanoparticles is in

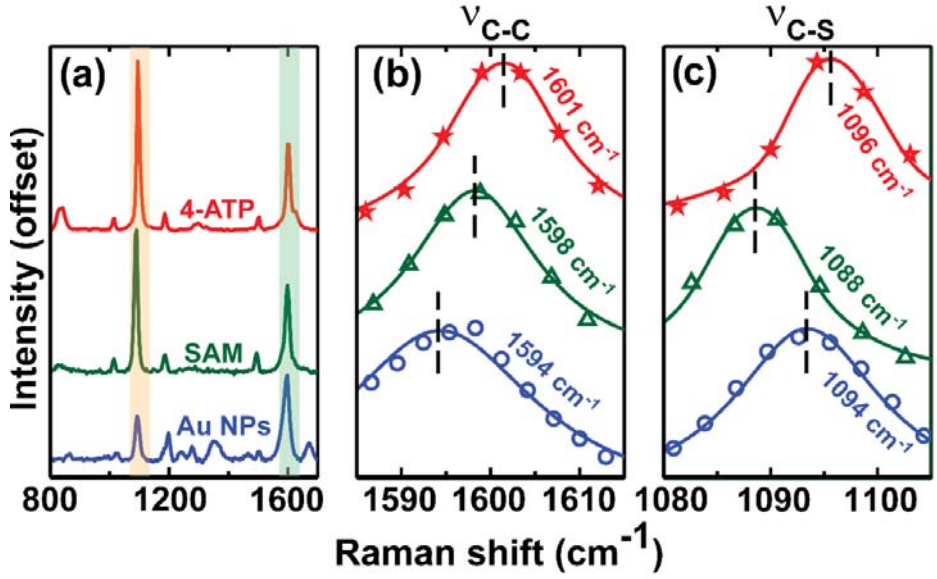

Figure 4.10. (a) Raman spectra of colloidal gold nanoparticles (blue, Au NPs) with chemisorbed 4-ATP, a self-assembled monolayer of gold nanoparticles on glass substrate with chemisorbed 4-ATP (green, SAM), and unbound 4-ATP molecules (red, 4-ATP). The spectra were normalized to the ν(C-C) mode. Lorentzian fit (solid line) and spectral data points for gold nanoparticles (circles), SAM (triangles), and 4-ATP (stars) for (b) ν (C-C) and (c) ν (C-S).

between the SAM and free 4-ATP molecules; the 4-ATP molecules were most tightly bound to the dried substrate. The ν (C-C) mode was blue-shifted from both the unbound and SAM-bound 4-ATP molecules, indicating that there was significant deformation due to bonding in the C-C bonds of the aromatic ring. The blue shift past both the SAM and unbound 4-ATP in this mode may have arisen from the fact that this mode is more sensitive to the number of adsorbed molecules than the ν(C-S) mode. Nonetheless, based on this data we can conclude that gold-thiolate bond formation is occurring without the need for directly measuring Raman modes associated with Au-S vibrations. Additional experiments for measuring the kinetics of colloidal gold to the glass substrate were not performed because our primary interest was in measuring the

binding kinetics and ligand exchange of thiolated molecules to the gold nanoparticle surface in solution. While it is technically possible to measure kinetic macroscopic substrate measurements with our experimental setup, we determined that the best way to prove gold-thiolate formation was to compare the center frequency of certain Raman bands in the colloidal kinetic data to dried substrate measurements.

4.4 Experimental

Materials. Cetyltrimethylammonium bromide (CTAB, >99%), sodium borohydride ($NaBH_4$, >99.99%), trisodium citrate ($Na_3C_6H_5O_7$, >99%), silver nitrate ($AgNO_3$, >99%), tetrachloroauric(III) acid ($HAuCl_4$, >99.999%), 5,5′-dithiobis-(2-nitrobenzoic acid) (DTNB, >95%), polystyrene sulfonate (PSS, 70,000 g/mol), 4-aminothiophenol (4-ATP, >97%), and hydroquinone (1,4-benzenediol, >99%) were purchased from Sigma-Aldrich and used without further purification. Glassware was cleaned with freshly prepared aqua regia (3:1 HCl:HNO_3) and rinsed with 18.2 MΩ-cm water multiple times.

Instrumentation. Raman spectra were acquired using a Horiba LabRAM HR 3D confocal microscope configured with 633 nm (8.5 mW at the sample) and 785 nm (110 mW at the sample) laser lines. A back-illuminated EMCCD (Andor, DU970P) was used for 633 nm experiments and a back-illuminated, deep-depletion CCD (Horiba Synapse) was used for 785 nm experiments. Unless noted otherwise, 633 nm laser excitation was used for Raman measurements. Spectra were acquired with a spectral resolution of 10 cm^{-1}. UV/vis absorption spectra were acquired with a Cary 5G spectrophotometer. Dynamic light scattering and ζ-potential measurements were acquired with a Malvern Zetasizer Nano ZS. Transmission electron microscopy was performed using a JEOL 2100 Cryo transmission electron microscope with an accelerating voltage of 200 kV.

Nanoparticle synthesis. Citrate-stabilized gold nanospheres were synthesized using the boiling citrate method where 97.5 mL of H_2O was mixed with 2.5 mL of 0.01 M $HAuCl_4$. Under magnetic stirring, the solution was heated until boiling at which point 3 mL of 5% w/v citrate solution was added. The solution was allowed to boil for 5 minutes and slowly turned deep red. After cooling down, the solution was centrifuged at 5,250 × *g* for 3 hours to remove excess citrate. CTAB-stabilized gold nanospheres were synthesized using a seed-mediated method as described elsewhere.[36] Gold nanorods were synthesized using a recently developed seed-mediated method with hydroquinone as the reducing agent.[37] To remove bound CTAB from gold nanorods we used a chloroform extraction technique described by Wei and coworkers.[38] Briefly, we took 5 mL of OD 20 gold nanorods in H_2O and added 5 mL of chloroform. The immiscible solvents were rapidly mixed for a minimum of 1 minute to form an emulsion and then centrifuged at 1,000 × *g* for 3 minutes. We then added 0.5 mL of 1% w/v PSS in H_2O and redispersed the pellet. After waiting 2 hours, centrifugation was repeated twice more to remove as much PSS-CTAB as possible. The sample was then centrifuged at 5,000 × *g* for 4 minutes in a 30,000 g/mol-molecular-weight-cutoff centrifuge filter. To the pellet, 1 mL of 1% w/v PSS was added. After 1 hour, the nanoparticles were centrifuged at 5,000 × *g* for 4 minutes and then redispersed in H_2O.

Substrate fabrication. A clean glass slide was functionalized with 10 mM ethanoic (3-aminopropyl)-trimethoxysilane overnight. After rinsing multiple times with ethanol, a solution of citrate-stabilized gold nanoparticles (~4 nm diameter) was deposited on the substrate and allowed to dry for 2 hours. The substrate was rinsed with H_2O multiple times and allowed to air dry. A 10 mM 4-ATP solution (pH = 3) in H_2O was deposited onto the substrate and allowed

to dry before Raman measurements were performed. For unbound 4-ATP measurements, an ethanoic solution of 50 mM 4-ATP was allowed to dry on a clean glass slide.

Kinetic Raman measurements. Solution phase samples (typically, 1.5 – 2 mL) were measured in a backscattering geometry with a 1 cm path length fused silica cuvette. Integration time varied between 10 to 20 seconds, depending on sample concentration. To initiate the kinetic measurements, Raman-active molecules were quickly added to a nanoparticle solution and rapidly mixed for approximately 30 seconds. Measurements began immediately after mixing.

4.5 Conclusion

Monitoring and understanding the kinetics of gold-thiolate bond formation is essential for the preparation of highly stable and robust gold nanoparticles. Covalent gold-thiolate bonds are superior over electrostatically bound molecules because electrostatic bonds are highly susceptible to diffusion and dissociation from the gold surface. Furthermore, maintaining the stability of gold nanoparticles in a variety of harsh ionic environments is critical for quantitative measurements.

Surface-enhanced Raman spectroscopy was used to indirectly monitor the kinetics of gold-thiolate bond formation. As a result of the intrinsic chemical specificity of Raman spectroscopy, it was possible to monitor the state of binding by analyzing the shift in center band frequency and FWHM by fitting a Lorentzian distribution to the collected data. Our results indicate that ligand exchange of citrate-stabilized and CTAB-stabilized gold nanospheres are well approximated by a first-order Langmuir adsorption model and have similar rate constants. Gold nanorods, in contrast, require additional purification steps and are challenging to fully exchange due to residual CTAB. We compared our results to an analytical model combining the

Beer-Lambert law with electromagnetic SERS enhancement. The predictive model shows a linear relationship between chemisorbed molecules and Raman intensity, whereas a time-varying nanoparticle concentration is nonlinear in colloidal suspensions. Our experimental results were in excellent agreement with this model.

4.6 References

(1) Gramotnev, D. K.; Bozhevolnyi, S. I. Nanofocusing of Electromagnetic Radiation. *Nat. Photonics* **2014**, *8*, 13–22.
(2) Atwater, H. A.; Polman, A. Plasmonics for Improved Photovoltaic Devices. *Nat. Mater.* **2010**, *9*, 205–213.
(3) Zhang, Y.; Guo, Y.; Xianyu, Y.; Chen, W.; Zhao, Y.; Jiang, X. Nanomaterials for Ultrasensitive Protein Detection. *Adv. Mater.* **2013**, *25*, 3802–3819.
(4) Tawil, N.; Hatef, A.; Sacher, E.; Maisonneuve, M.; Gervais, T.; Mandeville, R.; Meunier, M. Surface Plasmon Resonance Determination of the Binding Mechanisms of L-Cysteine and Mercaptoundecanoic Acid on Gold. *J. Phys. Chem. C* **2013**, *117*, 6712–6718.
(5) Jokerst, J. V.; Lobovkina, T.; Zare, R. N.; Gambhir, S. S. Nanoparticle PEGylation for Imaging and Therapy. *Nanomed.* **2011**, *6*, 715–728.
(6) Hines, D. A.; Kamat, P. V. Recent Advances in Quantum Dot Surface Chemistry. *ACS Appl. Mater. Interfaces* **2014**, *6*, 3041–3057.
(7) Häkkinen, H. The Gold-Sulfur Interface at the Nanoscale. *Nat. Chem.* **2012**, *4*, 443–455.
(8) Grzelczak, M.; Pérez-Juste, J.; Mulvaney, P.; Liz-Marzán, L. M. Shape Control in Gold Nanoparticle Synthesis. *Chem. Soc. Rev.* **2008**, *37*, 1783–1791.
(9) Qian, X.; Peng, X.-H.; Ansari, D. O.; Yin-Goen, Q.; Chen, G. Z.; Shin, D. M.; Yang, L.; Young, A. N.; Wang, M. D.; Nie, S. In Vivo Tumor Targeting and Spectroscopic Detection with Surface-Enhanced Raman Nanoparticle Tags. *Nat. Biotech.* **2008**, *26*, 83–90.
(10) Chang, Y.-C.; Yang, C.-Y.; Sun, R.-L.; Cheng, Y.-F.; Kao, W.-C.; Yang, P.-C. Rapid Single Cell Detection of Staphylococcus Aureus by Aptamer-Conjugated Gold Nanoparticles. *Sci. Rep.* **2013**, *3*.
(11) Xia, X.; Yang, M.; Wang, Y.; Zheng, Y.; Li, Q.; Chen, J.; Xia, Y. Quantifying the Coverage Density of Polyethylene Glycol Chains on the Surface of Gold Nanostructures. *ACS Nano* **2012**, *6*, 512–522.
(12) Love, J. C.; Estroff, L. A.; Kriebel, J. K.; Nuzzo, R. G.; Whitesides, G. M. Self-Assembled Monolayers of Thiolates on Metals as a Form of Nanotechnology. *Chem. Rev.* **2005**, *105*, 1103–1169.
(13) Berger, R.; Delamarche, E.; Lang, H. P.; Gerber, C.; Gimzewski, J. K.; Meyer, E.; Güntherodt, H.-J. Surface Stress in the Self-Assembly of Alkanethiols on Gold. *Science* **1997**, *276*, 2021–2024.
(14) Karpovich, D. S.; Blanchard, G. J. Direct Measurement of the Adsorption Kinetics of Alkanethiolate Self-Assembled Monolayers on a Microcrystalline Gold Surface. *Langmuir* **1994**, *10*, 3315–3322.

(15) Rouhana, L. L.; Moussallem, M. D.; Schlenoff, J. B. Adsorption of Short-Chain Thiols and Disulfides onto Gold under Defined Mass Transport Conditions: Coverage, Kinetics, and Mechanism. *J. Am. Chem. Soc.* **2011**, *133*, 16080–16091.
(16) Bellino, M. G.; Calvo, E. J.; Gordillo, G. Adsorption Kinetics of Charged Thiols on Gold Nanoparticles. *Phys. Chem. Chem. Phys.* **2004**, *6*, 424–428.
(17) Feng, Y.; Xing, S.; Xu, J.; Wang, H.; Lim, J. W.; Chen, H. Probing the Kinetics of Ligand Exchange on Colloidal Gold Nanoparticles by Surface-Enhanced Raman Scattering. *Dalton Trans.* **2009**, *39*, 349–351.
(18) Zhang, D.; Ansar, S. M. Ratiometric Surface Enhanced Raman Quantification of Ligand Adsorption onto a Gold Nanoparticle. *Anal. Chem.* **2010**, *82*, 5910–5914.
(19) Sharma, B.; Frontiera, R. R.; Henry, A.-I.; Ringe, E.; Van Duyne, R. P. SERS: Materials, Applications, and the Future. *Mater. Today* **2012**, *15*, 16–25.
(20) Valley, N.; Greeneltch, N.; Van Duyne, R. P.; Schatz, G. C. A Look at the Origin and Magnitude of the Chemical Contribution to the Enhancement Mechanism of Surface-Enhanced Raman Spectroscopy (SERS): Theory and Experiment. *J. Phys. Chem. Lett.* **2013**, *4*, 2599–2604.
(21) Moskovits, M. Persistent Misconceptions Regarding SERS. *Phys. Chem. Chem. Phys.* **2013**, *15*, 5301–5311.
(22) van Dijk, T.; Sivapalan, S. T.; DeVetter, B. M.; Yang, T. K.; Schulmerich, M. V.; Murphy, C. J.; Bhargava, R.; Carney, P. S. Competition between Extinction and Enhancement in Surface-Enhanced Raman Spectroscopy. *J. Phys. Chem. Lett.* **2013**, *4*, 1193–1196.
(23) Shriver, D. F.; Dunn, J. B. R. The Backscattering Geometry for Raman Spectroscopy of Colored Materials. *Appl. Spectrosc.* **1974**, *28*, 319–323.
(24) Kerker, M.; Wang, D.-S.; Chew, H. Surface Enhanced Raman Scattering (SERS) by Molecules Adsorbed at Spherical Particles: Errata. *Appl. Opt.* **1980**, *19*, 4159–4174.
(25) Johnson, P. B.; Christy, R. W. Optical Constants of the Noble Metals. *Phys. Rev. B* **1972**, *6*, 4370–4379.
(26) Bohren, C. F.; Huffman, D. R. *Absorption and Scattering of Light by Small Particles*; Wiley, 2007.
(27) Hermanson, G. T. *Bioconjugate Techniques*; 2nd ed.; Academic Press, 2008.
(28) Peng, H.; Chen, W.; Cheng, Y.; Hakuna, L.; Strongin, R.; Wang, B. Thiol Reactive Probes and Chemosensors. *Sensors* **2012**, *12*, 15907–15946.
(29) Küstner, B.; Gellner, M.; Schütz, M.; Schöppler, F.; Marx, A.; Ströbel, P.; Adam, P.; Schmuck, C.; Schlücker, S. SERS Labels for Red Laser Excitation: Silica-Encapsulated SAMs on Tunable Gold/Silver Nanoshells. *Angew. Chem. Int. Ed.* **2009**, *48*, 1950–1953.
(30) Hu, X.; Wang, T.; Wang, L.; Dong, S. Surface-Enhanced Raman Scattering of 4-Aminothiophenol Self-Assembled Monolayers in Sandwich Structure with Nanoparticle Shape Dependence: Off-Surface Plasmon Resonance Condition. *J. Phys. Chem. C* **2007**, *111*, 6962–6969.
(31) Nikoobakht, B.; El-Sayed, M. A. Preparation and Growth Mechanism of Gold Nanorods (NRs) Using Seed-Mediated Growth Method. *Chem. Mater.* **2003**, *15*, 1957–1962.
(32) Kluth, G. J.; Carraro, C.; Maboudian, R. Direct Observation of Sulfur Dimers in Alkanethiol Self-Assembled Monolayers on Au(111). *Phys. Rev. B* **1999**, *59*, R10449–R10452.

(33) Cheng, H.; Yang, L.; Jiang, Y.; Huang, Y.; Sun, Z.; Zhang, J.; Hu, T.; Pan, Z.; Pan, G.; Yao, T.; *et al.* Adsorption Kinetic Process of Thiol Ligands on Gold Nanocrystals. *Nanoscale* **2013**, *5*, 11795–11800.
(34) Torelli, M. D.; Putans, R. A.; Tan, Y.; Lohse, S. E.; Murphy, C. J.; Hamers, R. J. Quantitative Determination of Ligand Densities on Nanomaterials by X-Ray Photoelectron Spectroscopy. *ACS Appl. Mater. Interfaces* **2015**, *7*, 1720–1725.
(35) Vericat, C.; Vela, M. E.; Benitez, G.; Carro, P.; Salvarezza, R. C. Self-Assembled Monolayers of Thiols and Dithiols on Gold: New Challenges for a Well-Known System. *Chem. Soc. Rev.* **2010**, *39*, 1805–1834.
(36) Wu, X.; Ming, T.; Wang, X.; Wang, P.; Wang, J.; Chen, J. High Photoluminescence Yield Gold Nanocubes: For Cell Imaging and Photothermal Therapy. *ACS Nano* **2009**, *4*, 113–120.
(37) Vigderman, L.; Zubarev, E. R. High-Yield Synthesis of Gold Nanorods with Longitudinal SPR Peak Greater than 1200 nm Using Hydroquinone as a Reducing Agent. *Chem. Mater.* **2013**, *25*, 1450–1457.
(38) Leonov, A. P.; Zheng, J.; Clogston, J. D.; Stern, S. T.; Patri, A. K.; Wei, A. Detoxification of Gold Nanorods by Treatment with Polystyrenesulfonate. *ACS Nano* **2008**, *2*, 2481–2488.

CHAPTER 5

NUCLEAR-TARGETED SURFACE-ENHANCED RAMAN SCATTERING NANOPARTICLES

5.1 Introduction

Our need to develop diagnostic imaging techniques ranging from the subcellular-level and single-cell level to the tissue-level require multimodal imaging capabilities. Optical techniques such as surface-enhanced Raman spectroscopy (SERS) offer excellent chemical specificity and spatial resolution but require the use of precisely designed probes with specific targeting and Raman-active molecular signatures.[1] Raman spectroscopy's inherently poor signal can vastly be improved through the use of such probes, allowing for rapid imaging and detection. The highly sensitive SERS signature, however, overwhelms the rich chemical information originating from the cellular structure. In contrast, infrared spectroscopy may be used as a label-free[2] and chemically sensitive imaging technique but has relatively poor spatial resolution as a consequence of the diffraction limit of light as described by the Rayleigh criterion:

$$d = \frac{0.61}{\mathrm{NA}}\lambda \tag{5.1}$$

where d is the minimum resolvable feature, NA is the numerical aperture of the system, and λ is the wavelength of light. Clearly, the longer wavelengths of infrared light (2.5 – 10 μm) have poor spatial resolution with respect to visible light. Regardless, at the single-cell and tissue-level, chemical information obtained from infrared spectroscopy has been shown to be a valuable tool in automated histopathology and characterization of cancer cells.[3–5] Absorption cross sections of molecules are up to a factor of 10^6 higher than Raman scattering cross sections.[4] Whereas label-free Raman spectroscopy suffers from long integration times and often requires per-pixel rasterization of an image, making it a good candidate for imaging dimensionally small areas,

interferometric infrared spectroscopy is well-suited for wide-field imaging of tissue arrays. Here, we investigate and characterize nuclear-targeted gold nanoprobes using both modalities.

In general, SERS can function either an indicator of the chemistry of cellular structures localized within a few nanometers of plasmonic nanoparticles or as a robust contrast agent with pre-programmed molecular signatures determined by binding specific Raman-active molecules to the nanoparticle surface. While only roughly 1 in 10 million incident photons are Raman scattered, SERS can provide enhancement of Raman scattering up to $10^8 – 10^{10}$ orders of magnitude, depending on geometry and material composition.[6] Because it is difficult to precisely place probes in direct contact with a desired protein or cellular structure,[7] researchers often choose to opt for pre-programmed molecular signatures and develop *in vitro* or *in vivo* targeting capabilities.

Infrared spectroscopy requires careful consideration of the sample substrate, the constituents of the sample itself, as well as the method of illumination. Commonly, cells or tissues are placed on inexpensive low-emissivity (low-e) glass rather than expensive and sometimes toxic salt windows. Low-e glass is also convenient to use because it transmits visible light and reflects infrared light allowing for transmissive dark-field optical imaging. In typical FTIR transmission and transflectance measurements, scattering effects such as resonant Mie scattering occur because cells are on the same order of magnitude of the incident light. In most cases scattering is undesirable and corrections exist to help adjust for this when performing quantitative spectroscopic measurements.[8] Individual gold nanoparticles have relatively small scattering cross sections in the infrared; however, targeted nanoparticles applied to biological systems often aggregate and, consequently, a higher degree of scattering. To minimize cellular scattering in infrared spectroscopic measurements, researchers often use attenuated total

reflectance Fourier transform infrared (ATR-FTIR) spectroscopy. ATR-FTIR uses a dielectric of high index of refraction to generate an evanescent wave by total internal reflection and probe the surface layer of a sample.

Here, we investigate endocytosed nuclear-targeted nanoprobes using a combination of electromagnetic simulations, confocal Raman microscopy, and infrared spectroscopy to better understand plasmonic nanoprobes as contrast agents throughout the optical and infrared spectrum. By doing so, we hope to achieve a better understanding of how to engineer and prepare nanoprobe-based samples for characterization from the subcellular level up to the tissue level.

5.2 Theory

Widespread usage of SERS has resulted in numerous chemical and biological studies within the last few years.[1,9] While some disagreement still exists, most researchers describe SERS through two mechanisms: chemical enhancement and electromagnetic enhancement.[6,10] Electromagnetic enhancement is a consequence of the light harvesting nature of plasmonic nanostructures. In other words, resonance of the charge density oscillation of metallic nanostructures leads to strong absorption and scattering of light called the localized surface plasmon resonance (LSPR). Surface-bound molecules interacting with concentrated levels of localized light leads to enhanced Raman scattering. At an incident frequency of light ω_0, electromagnetic enhancement *G* may be described in terms of the local electric field **E** and a Stokes shifted frequency ω_s:

$$G(\omega_0, \omega_s) = \left|\mathbf{E}(\omega_0)\right|^2 \left|\mathbf{E}(\omega_0 - \omega_s)\right|^2 \approx \left|\mathbf{E}(\omega_0)\right|^4 \tag{5.2}$$

where we neglect the Stokes shift because it is relatively small. The second mechanism, chemical enhancement, is still poorly understood but is likely related to metal-molecule resonances and charge transfer.[10,11] We also neglect chemical enhancement because it is difficult to engineer metal-molecule complexes.

Surface-enhanced infrared absorption (SEIRA) spectroscopy is the infrared analog to SERS in which infrared light generates a standing wave within nanostructures or on nanopatterned substrates, leading to an enhanced infrared absorption at certain frequencies of light.[12] In contrast to SERS nanoparticles, patterned SEIRA substrates use rather large feature sizes up to a few microns in length in order to satisfy resonance conditions in the mid-IR. For biological imaging applications, we are typically interested in nanoprobes that have diameters between 30 – 50 nm because they have been shown to exhibit improved cellular uptake and minimal toxicity.[13] At these sizes, the SEIRA effect is exceedingly weak because the LSPR is in the visible region and the nanoprobe's dielectric function behaves as a perfect metal in the infrared. Using electromagnetic simulations we sought to understand the degree of influence SEIRA would have on the infrared spectra for endocytosed nanoprobes. While the illumination wavelength is exceedingly far away from the nanoparticle's plasmon resonance, infrared light can still concentrate near the surface.

In terms of the equivalent electromagnetic enhancement mechanism, the enhancement factor G_{SEIRA} scales as the electric field intensity:[14]

$$G_{\mathrm{SEIRA}} = \left|\mathbf{E}(\omega_0)\right|^2 \tag{5.3}$$

Because SEIRA is an absorptive phenomenon, it is described by an electric field-squared relation rather than an $|\mathbf{E}|^4$ relation like SERS. As a consequence of this relationship, SEIRA enhancement factors are considerable smaller than SERS enhancement factors.

SEIRA and SERS simulations were performed using the boundary element method (BEM) originally formulated for plasmonic nanostructures by F. J. García de Abajo and coworkers.[15] BEM is a method for numerically solving Maxwell's equations across discrete interfaces using an appropriately constructed Green's function and surface integral equations. Application of the appropriate boundary conditions leads to the formulation of surface charges and currents, which may then be used to calculate the electric field and, subsequently, far-field absorption and scattering. The optical constants of all metals were calculated from an empirically derived Drude model and extended into the infrared region, as described elsewhere.[16,17] Plane wave excitation wave assumed for all simulations. We plan to further investigate the effects of plane wave versus evanescent field excitation and substrate effects in a future investigation.

The case of an isolated 40 nm gold nanosphere under three different excitation wavelengths is shown in Figure 5.1. For this case, the surrounding index of refraction was assumed to have an index of refraction of $n = 1.4$.[18] The electric field distribution clearly shows a concentration of light near the nanoparticle surface for excitation wavelengths close to the LSPR (633, 780 nm). More importantly, excitation with a 7200 nm (~1400 cm^{-1}) plane wave exhibits almost an order of magnitude increase of localized light surrounding the nanoparticle ($G_{SEIRA} = 7.5$). While far from the LSPR, the maximum $|\mathbf{E}|^2$ at 7200 nm excitation is only 20% less than the maximum $|\mathbf{E}|^2$ at 780 nm. Mid-infrared spectroscopic measurements are particularly prone to spectral distortions due to scattering. Nanospheres tend to scatter at higher wavenumber and are very sensitive to the surrounding index of refraction. This contribution is likely to have

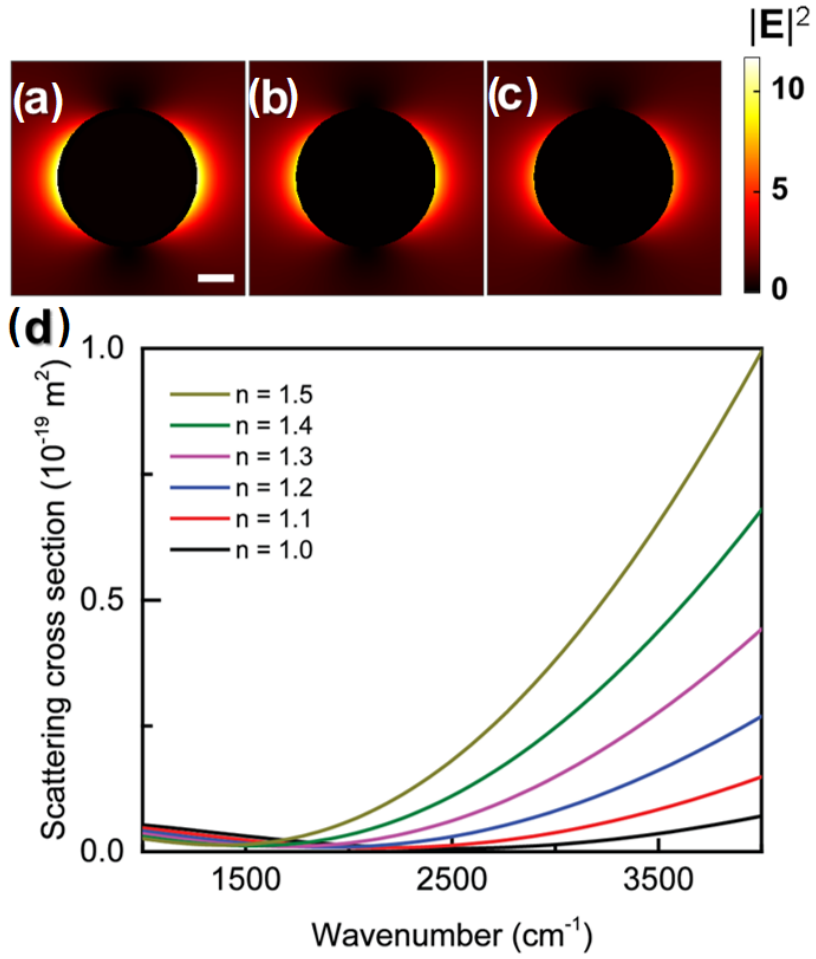

Figure 5.1. Near-field distribution of isolated gold nanospheres (diameter = 40 nm) surrounded in a dielectric medium of n = 1.4 with an excitation wavelength of (a) 633 nm (max $|\mathbf{E}|^2 = 11.6$), (b) 780 nm (max $|\mathbf{E}|^2 = 9.3$), and (c) 7200 nm (max $|\mathbf{E}|^2 = 7.5$). Scale bar: 10 nm. (d) Far-field scattering cross section of an isolated nanosphere surrounded by a dielectric with index of refraction ranging from $n = 1.0 – 1.5$.

its greatest effect on C-H vibrational modes for biological samples. For a single nanosphere the scattering cross section is exceedingly small; however, we experimentally expect large aggregates of nanoparticles, resulting in a greater degree of a scattering. The scattering spectra is sensitive to surrounding dielectric environment. Moreover, our results show that nanoparticles embedded within cellular structure ($n \sim 1.4$) have a higher scattering cross section than isolated nanoparticles in air.

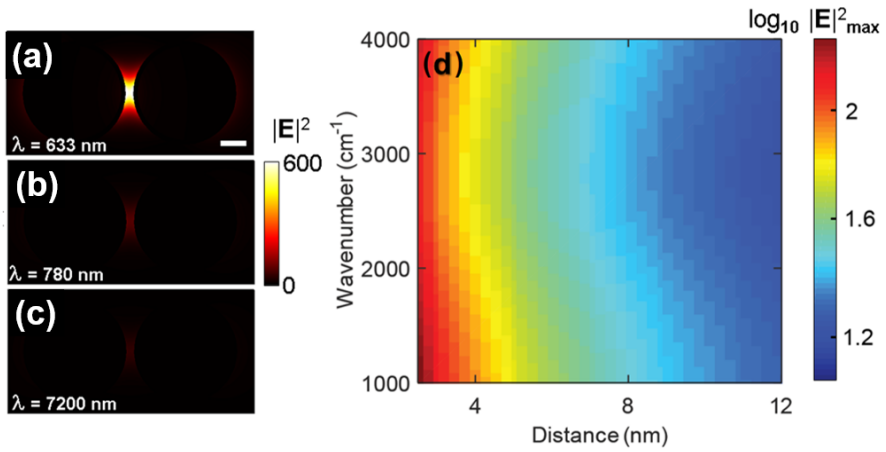

Figure 5.2. Near-field distribution of a dimerized gold nanosphere (diameter = 40 nm, 5 nm gap) at an excitation of (a) 633 nm (max $|\mathbf{E}|^2 = 670$), (b) 780 nm (max $|\mathbf{E}|^2 = 78$), and (c) 7200 nm (max $|\mathbf{E}|^2 = 44$) surrounded by a medium of $n = 1.4$. Scale bar: 10 nm. (d) Electric field intensity for a given wavenumber and separation distance of dimerized gold nanospheres.

In Figure 5.2, the properties of gold nanoparticles at mid-infrared frequencies were calculated for the near- and far-field properties of a dimerized gold nanosphere. Dimers and other higher-order aggregates are a highly studied area of research in SERS because they can greatly enhance the Raman scattering cross section up to single-molecule sensitivities.[19,20] Hot-spots are caused by plasmonic coupling (quantum mechanical tunneling of electrons) between nearby (< 3 nm) metallic surfaces that lead to huge SERS enhancement factors (up to 10 orders of magnitude).[6] Because it is difficult to precisely control molecular positioning and nanometer scale gaps between surfaces, signal variability from hot-spots has somewhat hindered the development of SERS. Excitation near the LSPR (633 nm) results in an intense electric field, as expected. Unlike the isolated sphere case, the maximum $|\mathbf{E}|^2$ at 7200 nm is 40% less than excitation at 780 nm. This indicates that hot-spots between plasmonic surfaces contribute much less to the SEIRA signal as compared to SERS. As a consequence, there is less expectation of aggregates enhancing the infrared spectra. We see that enhancement is wavelength dependent in the mid-infrared and tends to increase for smaller wavenumber.

5.3 Results and discussion

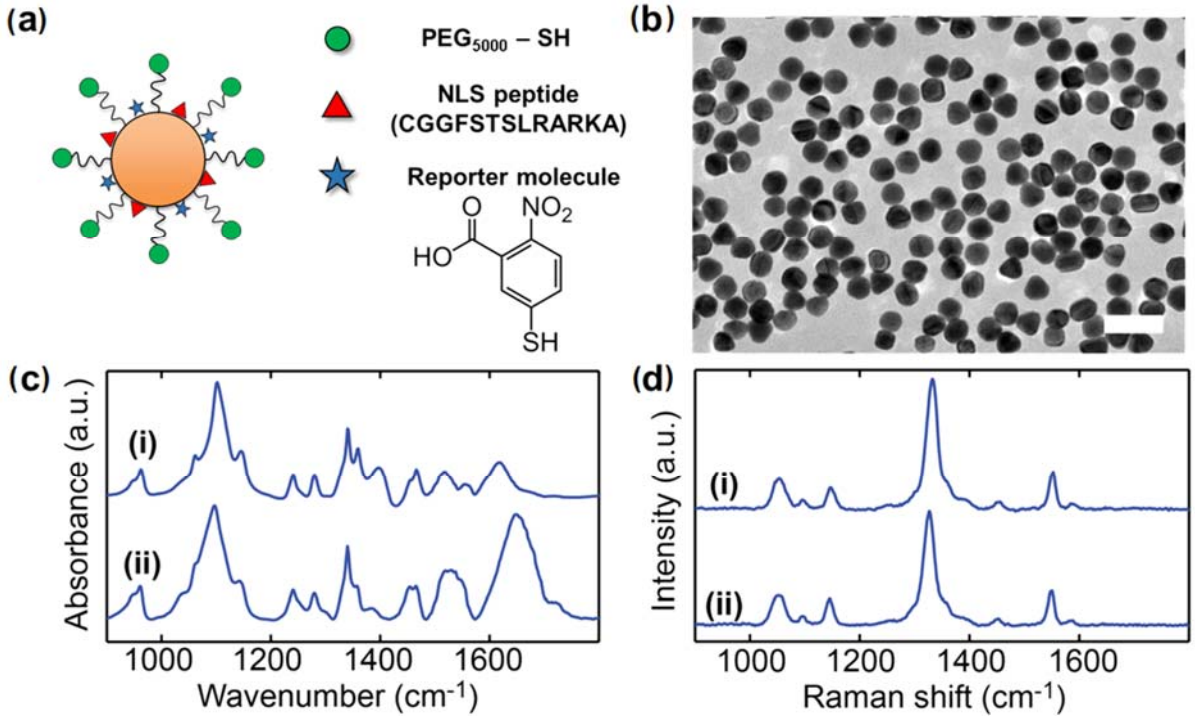

Figure 5.3. (a) Schematic of synthesized SERS probes with conjugated NLS peptide. (b) Transmission electron micrograph of gold nanoparticles. Scale bar: 100 nm. (c) ATR FT-IR spectra of probes and (d) SERS spectra of probes (i) with and (ii) without bound peptides.

Nuclear-targeted gold nanoparticles were synthesized as shown in Figure 5.3. Average nanoparticle size and geometry were confirmed by transmission electron microscopy (TEM) and found to be 37.4 +/- 4.1 nm as determined by measuring the diameter of ~200 nanoparticles. Nanoparticles with diameters of 30 – 50 nm have been repeatedly shown to exhibit enhanced cellular uptake and minimal toxicity as compared to other dimensions.[13,21] These nanoparticles were prepared with a mixed monolayer consisting of thiolated methyl ether polyethylene glycol (PEG_{5000}-SH), nuclear localization sequence (NLS) peptides, and Raman-active reporter molecules (5-thio-2-nitrobenzoic acid or TNB). Previously, Liu and coworkers demonstrated that the adenovirus-derived NLS peptide sequence CGGFSTSLRARKA was effective for targeting the nuclei of HeLa cells with conjugated gold nanoparticles.[22] NLS peptides were attached

covalently to the gold surface with the free cysteine side chain (see Section 5.4). Zeta potential was used to confirm successful surface modification: as-synthesized gold nanoparticles (CTAB-stabilized) had a surface charge of 39 +/- 3 mV. Peptide-conjugated nanoparticles with PEG and TNB had a surface charge of -8 +/- 1 mV. This indicates that the neutral species PEG successfully bound and stabilized the surface. Morphology and size distribution were further characterized by UV/Vis spectroscopy and dynamic light scattering, as shown in Figure 5.4.

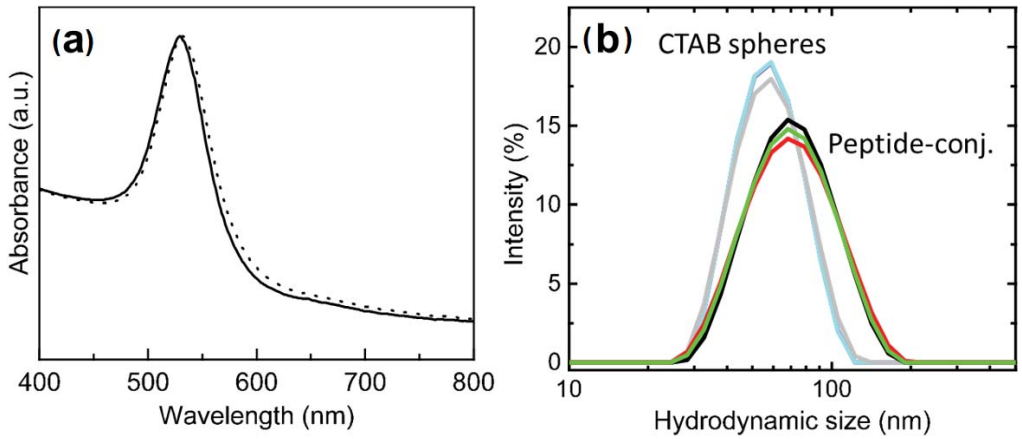

Figure 5.4. (a) UV/Vis spectra of (solid) as-synthesized CTAB nanospheres and (dotted) peptide-conjugated nanospheres with PEG and TNB. (b) Dynamic light scattering of nanospheres before and after peptide conjugation. The addition of PEG and peptide ligands results in an overall larger hydrodynamic size and slightly broader size distribution.

Preparing highly functionalized, targeted nanoprobes can be accomplished by developing nanoparticles with a mixed monolayer of thiolated molecules. Our functionalization strategy was based off our previous characterization studies demonstrating that monolayer formation of small thiolated molecules bind to gold nanoparticles according to a first-order Langmuir adsorption model.[23] Assuming that PEG-SH behaves similarly,[24] we estimate 50% PEG-SH, 25% NLS, and 25% TNB coverage per nanoparticle. To verify surface chemistry composition, dried films of unconjugated and peptide-conjugated nanoparticles on an infrared reflective substrate (MirrIR

low-emissivity glass) were characterized using attenuated total reflectance Fourier transform infrared (ATR FT-IR) spectroscopy. Before characterization, all nanoparticle suspensions were extensively dialyzed in 18.2 MΩ-cm water to remove excess ligands and other byproducts. The ATR FT-IR spectra clearly show differences between the unconjugated and conjugated samples. Most notably, the emergence of an amide I mode centered at 1654 cm^{-1} indicates successful peptide conjugation. Amide II (1545 cm^{-1}) was also observed but there is some overlap with the vibrational modes of TNB. The spectral features of the bound PEG dominate the ATR FT-IR spectra. The vibrational mode at 1096 cm^{-1} corresponds to C-O-H and C-O-C stretching. The bands at 1340 and 1466 cm^{-1} correspond to C-H bending modes.[25] A relatively weak contribution from TNB is observed at 1398 cm^{-1} corresponding to a symmetric N-O stretching mode. An aromatic C-C bending mode (1618 cm^{-1}) from TNB is also observed in the unconjugated sample. To further characterize the surface chemistry, Raman spectroscopy was performed. We observed the characteristic SERS spectra of TNB with an intense vibrational mode at 1333 cm^{-1} (symmetric N-O stretch) and a less intense C-S stretching mode at 1098 cm^{-1}.[26] The SERS spectra of peptide conjugated nanoparticles is indistinguishable from unconjugated nanoparticles, illustrating the need for FT-IR data to confirm surface chemistry composition.

Freshly prepared and characterized nuclear-targeted gold nanoparticles (0.5 nM final concentration) were incubated with MCF-10A cells for 6 hours before ethanol fixation. In Figure 5.5, bright-field (BF) and dark-field (DF) optical microscopy were used to help spatially localize the nanoparticles within the cells. Due to the relatively high concentration of endocytosed nanoparticles, it was possible to clearly see clusters of nanoparticle aggregates in both the BF and DF images). Colocalized images of optical, ATR FT-IR, and Raman were obtained. As a consequence of the need for direct contact of the sample with the crystal, ATR

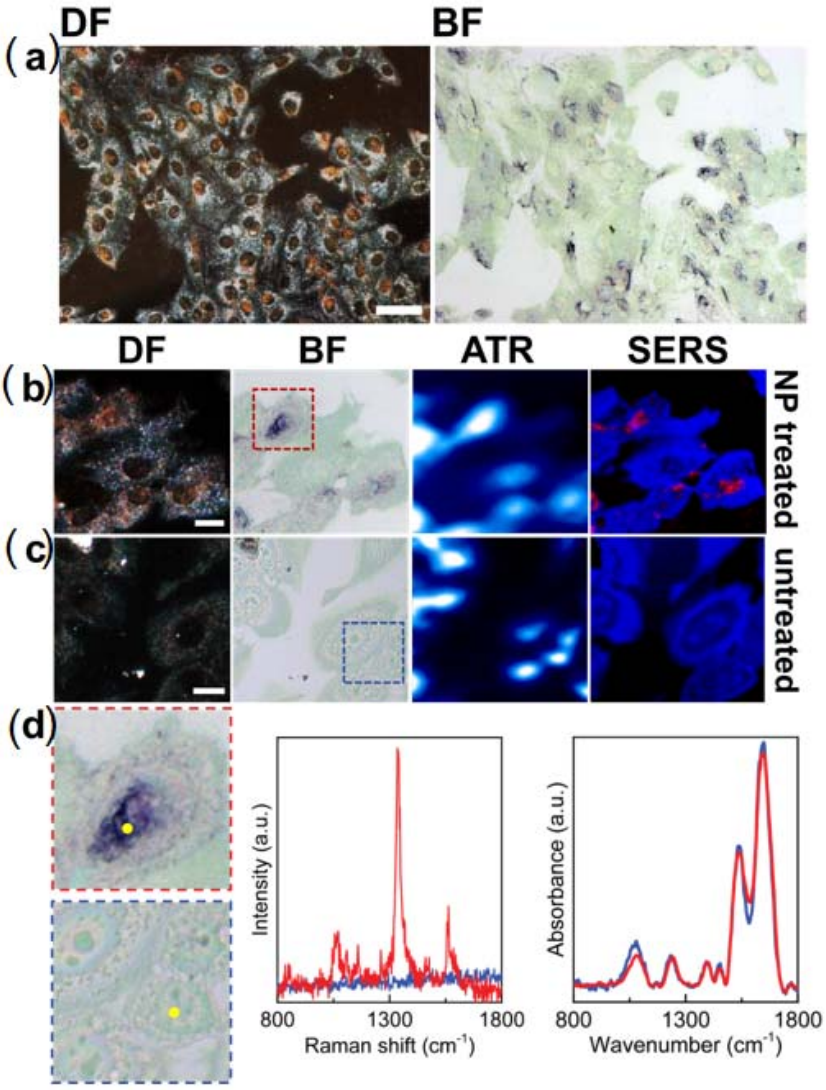

Figure 5.5. (a) Optical microscopy (DF – left, BF – right) images of fixed MCF-10A cells incubated with peptide conjugated nanoparticles for 6 hours before fixation. Scale bar: 50 μm. Colocalized images of DF, BF, ATR FT-IR (Amide I, 1656 cm^{-1}), and SERS (red – symmetric N-O stretch, 1333 cm^{-1}; blue – reflectance) of (b) nanoparticle treated and (c) untreated cells. (d) Enlarged optical images as indicated by the dotted boxes and corresponding single pixel spectra at the indicated position (in yellow).

images tend to have slightly distorted morphological features. We analyzed the infrared spectra using principle component analysis and were unable to successfully distinguish between regions containing a high concentration of nanoparticle aggregates and those without. This is a consequence of the high intensity of cellular infrared spectroscopic signatures with respect to the

relatively weak conjugated nanoparticle signal. Despite these clusters being on order of a few microns, the nanoparticle signature could not be recovered from ATR FT-IR data. An Si-O stretching mode contribution at 1100 cm^{-1} also appears in the spectra.[27]

Despite the ability of gold nanoparticles to concentrate light in the mid-infrared, the SEIRA effect is exceedingly weak as compared to the absorption cross section of the cells. Large clusters of randomly oriented aggregated nanoparticles could, however, significantly influence the scattering spectra throughout the mid-infrared frequencies. While hot-spots are notorious in the field of SERS for making quantification difficult; the challenges associated with imaging nanoparticles with infrared spectroscopy are likely related to scattering effects. Consequently, the lack of influence from gold nanoparticles embedded within tissue may make it possible to extract important chemical information from the cells that would otherwise be obscured in SERS spectra, which is dominated by the nanoparticle signature.

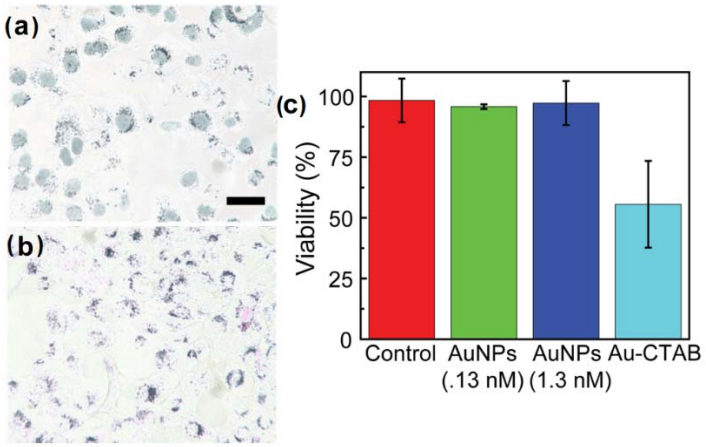

Figure 5.6. Optical image of representative sample of MCF-10A cells incubated with nanoparticles for 24 hours and stained with trypan blue: (a) CTAB-stabilized gold nanospheres and (b) peptide-conjugated gold nanospheres (1.3 nM). Scale bar: 50 μm. (c) Percent viability of a control (no nanoparticles), two concentrations of peptide-conjugated nanospheres (.13 nM and 1.3 nM) and CTAB-stabilized gold nanospheres (1.0 nM).

The toxicity of the mixed monolayer nanoparticles with MCF-10A cells were evaluated

by performing a trypan blue exclusion assay. As shown in Figure 5.6, the trypan blue exclusion assay showed that CTAB-stabilized gold nanoparticles were highly toxic. In contrast, cells incubated with peptide-conjugated gold nanoparticles cellular uptake was observed with minimal cell death. The trypan blue assay indicated that the surface chemistry of peptide-conjugated gold nanoparticles had minimal toxicity.

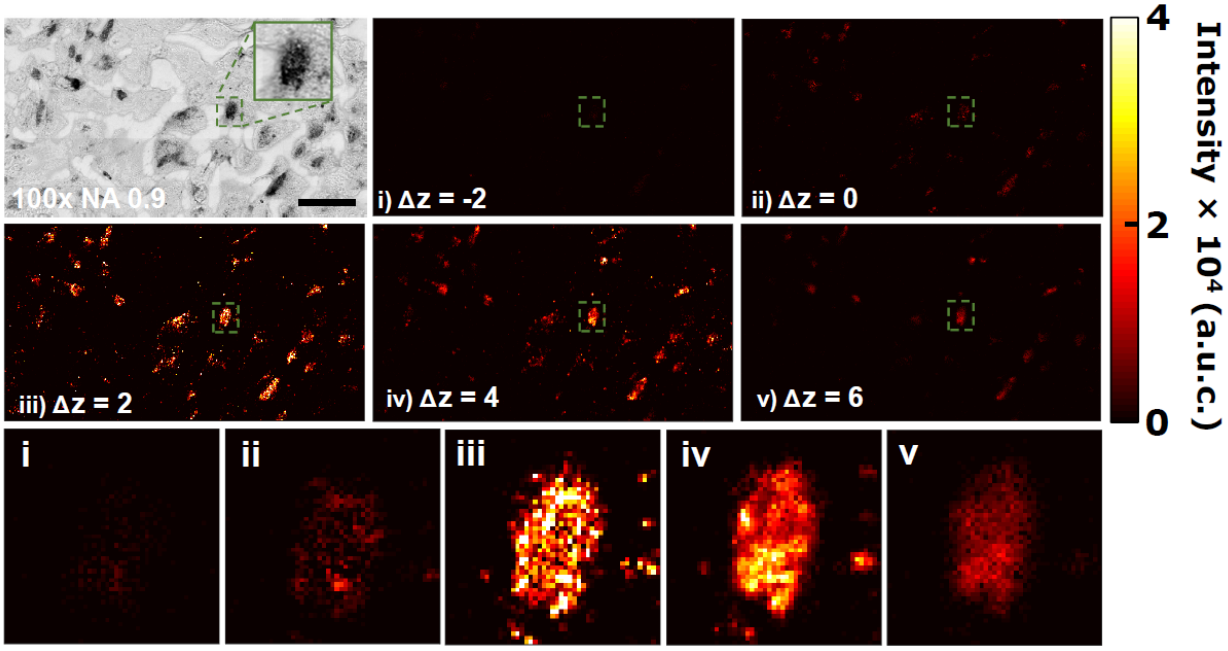

Figure 5.7. Visible light image (top left) and corresponding depth scanned confocal Raman images (i – v) of the N-O stretching mode (1333 cm^{-1}) in 2 μm step sizes. Scale bar: 50 μm.

To further investigate the distribution of the nanoparticles in the cells, we used confocal Raman microscopy (780 nm excitation) to acquire multiple layers of images offset 2 μm per step. As shown in Figure 5.7, we observed that the nanoparticles embedded within cells on reflective substrate are primarily confined to two image planes. The nanoparticles are highly localized to the nucleus and its surroundings, indicating that successful peptide conjugation and targeting occurred. The Raman spectra were acquired with a 100× 0.9 NA objective and the N-O symmetric stretching mode was integrated around 1333 cm^{-1}. Attempts to obtain cellular

chemical spectra (*i.e.*, C-H vibrational modes at ~2800 cm^{-1}) using Raman were unsuccessful due to the overwhelming signature of the nanoparticles. Furthermore, excitation at 532 nm led to rapid melting of the nanoparticles due to the strong localized surface plasmon resonance absorption.

In summary, nuclear-targeted nanoprobes were developed and characterized using optical and infrared spectroscopy. The surface chemistry of the nanoprobes consisted of a mixed monolayer of ligands including NLS peptides, PEG-SH, and TNB. The Raman reporter molecule (TNB) bound to the gold nanoprobe surface was easily observed using confocal Raman microscopy. Using ATR-FTIR, we confirmed the surface chemistry of the peptide-bound nanoprobes and observed the strongest signal to originate from the PEG ligands. The formation of aggregate during the cellular uptake process did not result in a noticeable signal SEIRA enhancement, which is confirmed by our theoretical model that demonstrates dimerized gold nanoparticles have less enhancement contribution in the infrared because the excitation wavelength is far away from the LSPR.

5.4 Experimental

Materials. Cetyltrimethylammonium bromide (CTAB, > 99%), 5,5'-dithiobis-(2-nitrobenzoic acid (DTNB, >95%), poly(ethylene glycol) methyl ether thiol (5,000 g/mol), L-ascorbic acid (>99%), sodium borohydride ($NaBH_4$, 99.99%), tetrachloroauric(III) acid ($HAuCl_4$, > 99.999%), trypan blue and Spectra-Por Float-A-Lyzer G2 dialysis membranes (100,000 g/mol) were purchased from Sigma-Aldrich and used without further modification. Lyophilized peptides with the sequence CGGFSTSLRARKA (NLS) with >95% purity and terminal acetylation/amidation were purchased from Biomatik. All glassware was cleaned with aqua regia (3:1 $HCl:HNO_3$) and rinsed multiple times with 18.2 MΩ-cm H_2O before use.

Instrumentation. Raman microspectroscopy was performed on a Horiba LabRAM HR microscope with a Horiba Synapse deep-depletion detector (1024 × 256 pixels, 26 μm × 26 μm pixel size). Samples were illuminated with a 632.8 nm HeNe laser and a spectral resolution of 10 cm^{-1}. Images were acquired with a 50× 0.75 NA objective and a pixel size of 750 × 750 nm with integration times ranging between 10 – 100 milliseconds per pixel depending on signal strength. Depth scans were performed on a Thermo Fisher DXRxi Raman imaging microscope with a confocal pinhole of 25 μm and an EMCCD detector (1600 × 200 pixels, 16 μm × 16 μm pixel size). Images were acquired with a 100× 0.9 NA objective with a 780 nm excitation wavelength. FTIR transflectance measurements were acquired with a PerkinElmer Spotlight One imaging system with 6.25 μm × 6.25 μm pixel size. ATR-FTIR infrared microspectroscopy images were acquired with a PerkinElmer Spotlight 400 FTIR imaging system, a germanium crystal/ATR attachment, and 1.56 μm × 1.56 μm pixel size. Data was collected using a raster scanning MCT linear array detector with an interferometer speed of 1.0 cm/s. The ATR crystal was put in contact with the tissue with minimum possible contact to capture the cells to minimize sample damage. The background spectra was acquired at 120 scans per pixel and a spectral resolution of 4 cm^{-1}. Atmospheric correction and the ATR correction was applied using PerkinElmer Spotlight software and the further analysis was done in ENVI-IDL or MATLAB. Infrared transflectance and ATR measurements were performed on low-emissivity (low-e) microscope slides (MirrIR, Kevley Technologies). UV/Vis absorption spectra were acquired with a GE Healthcare GeneQuant 1300 spectrophotometer. ζ-potential/dynamic light scattering measurements were performed on a Malvern Zetasizer Nano ZS. Optical bright-field and dark-field microscopy images were acquired with a Zeiss Axiovision Imager M2. Transmission electron microscopy was performed on a JEOL 2100 Cryo TEM with an accelerating voltage of

200 kV. Aqueous samples were deposited on a holey carbon grid (Ted Pella) and allowed to air dry before imaging.

Nanoparticle synthesis. Gold nanospheres stabilized with cetyltrimethylammonium bromide were synthesized according to a well-established protocol.[28] Briefly, a nanoparticle seed solution was made by rapidly mixing 0.25 mL of 10 mM $HAuCl_4$, 7.5 mL of 100 mM CTAB, 0.6 mL of ice-cold, freshly prepared 10 mM $NaBH_4$. Upon addition of the $NaBH_4$, the solution immediately turned light brown. The seed solution was allowed to sit for 1 hour to hydrolyze remaining $NaBH_4$. Gold nanospheres were prepared in large batches to maximize monodispersity and uniformity across samples: a typical growth solution consisted of 64 mL of 100 mM CTAB, 8 mL of 10 mM $HAuCl_4$, and 320 mL of H_2O. The resulting solution appeared bright orange, indicating the formation of an $AuBr_4^-$ complex. Under moderate magnetic stirring, 38 mL of 100 mM L-ascorbic acid was added. The solution immediately turned colorless indicating reduction to Au (I). The seed solution was then diluted 5× and 200 μL was mixed into the solution. The solution slowly turned from colorless to red. After 1 hour, the solution was centrifuged at 5250 × g for 1.5 hours and resuspended in water. Resuspension/centrifugation was performed a total of two times to remove CTAB and reaction byproducts.

Surface modification and peptide conjugation. A solution consisting of 1 mM mPEG-SH was added to a solution of gold nanoparticles (λ = 530 nm, OD = 25) under sonication. After 1 hour, the nanoparticles were spun at 6000 × g for 15 minutes and resuspended in 1 mL of 10× phosphate buffered saline. To the nanoparticle solution, 20 μL of 1 mM DTNB (pH ~ 7 – 8) and 20 μL of NLS (1,394.61 g/mol at a concentration of 4 mM) were added and allowed to sit for 4 hours. Samples were subject to dialysis (100,000 g/mol) for a minimum of 24 hours at room temperature to remove excess, unbound peptides, reporter molecules, and PEG. After

dialysis, samples were stored at 4 degrees Celsius until use. Samples were prepared within a week of usage as a precaution to avoid peptide degradation.

Cell culture. MCF-10A (ATCC, normal human mammary epithelial cells) following standard cell culture procedures[29] were seeded in 24 well plates to reach about 50 – 70% confluency on low-emissivity glass. Cells were incubated with peptide-conjugated gold nanoparticles for 6 hours before washing 3× with 1× PBS and then fixed with 70% ethanol for 30 seconds. In a typical experiment, 1.25 mL of cell culture media was mixed with 0.5 mL of peptide-conjugated nanoparticles (λ = 531 nm, OD = 5 – 7). Cell viability was assessed with a trypan blue exclusion assay using the MCF-10A cell line. Briefly, cells were seeded in triplicate at 5000 cells per well in 96 well plates. After 48 hours of growth, cells were washed 3× in 1× PBS and incubated with nanoparticles in phenol red free complete medium for 24 hours. Post incubation cells were washed 3× with 1× PBS to remove remaining nanoparticles. Cell death was assessed using trypan blue exclusion assays. Cells were seeded at 3×10^5 cells per well in six well plates and grown for 48 hours. Cells were then washed 3× with 1× PBS and incubated with nanoparticles in phenol red free complete medium for 24 hours. Post incubation, cells were washed 3× with 1× PBS to remove remaining nanoparticles. Phenol free medium with 0.04% trypan blue was then added and samples imaged immediately. Images were taken in three spatially distinct areas of each sample and cell counts were performed using ImageJ.

Electromagnetic simulations. Simulations were performed using the MNPBEM v1.4 software package created by U. Hohenester and A. Trügler.[30–32] Silver and gold dielectric constants were obtained using an empirically derived Drude model, as described elsewhere.[16,17]

5.5 References

(1) Xie, W.; Schlücker, S. Rationally Designed Multifunctional Plasmonic Nanostructures for Surface-Enhanced Raman Spectroscopy: A Review. *Rep. Prog. Phys.* **2014**, *77*, 116502.

(2) Sreedhar, H.; Varma, V. K.; Nguyen, P. L.; Davidson, B.; Akkina, S.; Guzman, G.; Setty, S.; Kajdacsy-Balla, A.; Walsh, M. J. High-Definition Fourier Transform Infrared (FT-IR) Spectroscopic Imaging of Human Tissue Sections towards Improving Pathology. *J. Vis. Exp.* **2015**.

(3) Fernandez, D. C.; Bhargava, R.; Hewitt, S. M.; Levin, I. W. Infrared Spectroscopic Imaging for Histopathologic Recognition. *Nat. Biotechnol.* **2005**, *23*, 469–474.

(4) Levin, I. W.; Bhargava, R. Fourier Transform Infrared Vibrational Spectroscopic Imaging: Integrating Microscopy and Molecular Recognition. *Annu. Rev. Phys. Chem.* **2005**, *56*, 429–474.

(5) Holton, S. E.; Walsh, M. J.; Kajdacsy-Balla, A.; Bhargava, R. Label-Free Characterization of Cancer-Activated Fibroblasts Using Infrared Spectroscopic Imaging. *Biophys. J.* **2011**, *101*, 1513–1521.

(6) Le Ru, E. C.; Etchegoin, P. G. Quantifying SERS Enhancements. *MRS Bull.* **2013**, *38*, 631–640.

(7) Ando, J.; Fujita, K.; Smith, N. I.; Kawata, S. Dynamic SERS Imaging of Cellular Transport Pathways with Endocytosed Gold Nanoparticles. *Nano Lett.* **2011**, *11*, 5344–5348.

(8) Bassan, P.; Kohler, A.; Martens, H.; Lee, J.; Byrne, H. J.; Dumas, P.; Gazi, E.; Brown, M.; Clarke, N.; Gardner, P. Resonant Mie Scattering (RMieS) Correction of Infrared Spectra from Highly Scattering Biological Samples. *The Analyst* **2010**, *135*, 268–277.

(9) Vo-Dinh, T.; Liu, Y.; Fales, A. M.; Ngo, H.; Wang, H.-N.; Register, J. K.; Yuan, H.; Norton, S. J.; Griffin, G. D. SERS Nanosensors and Nanoreporters: Golden Opportunities in Biomedical Applications. *Wiley Interdiscip. Rev. Nanomed. Nanobiotechnol.* **2015**, *7*, 17–33.

(10) Moskovits, M. Persistent Misconceptions Regarding SERS. *Phys. Chem. Chem. Phys.* **2013**, *15*, 5301–5311.

(11) Valley, N.; Greeneltch, N.; Van Duyne, R. P.; Schatz, G. C. A Look at the Origin and Magnitude of the Chemical Contribution to the Enhancement Mechanism of Surface-Enhanced Raman Spectroscopy (SERS): Theory and Experiment. *J. Phys. Chem. Lett.* **2013**, *4*, 2599–2604.

(12) Hornemann, A.; Eichert, D.; Flemig, S.; Ulm, G.; Beckhoff, B. Qualifying Label Components for Effective Biosensing Using Advanced High-Throughput SEIRA Methodology. *Phys. Chem. Chem. Phys.* **2015**, *17*, 9471–9479.

(13) Dykman, L. A.; Khlebtsov, N. G. Uptake of Engineered Gold Nanoparticles into Mammalian Cells. *Chem. Rev.* **2013**, *114*, 1258–1288.

(14) Adato, R.; Aksu, S.; Altug, H. Engineering Mid-Infrared Nanoantennas for Surface Enhanced Infrared Absorption Spectroscopy. *Mater. Today* **2015**, *18*, 436–446.

(15) García de Abajo, F. J.; Howie, A. Retarded Field Calculation of Electron Energy Loss in Inhomogeneous Dielectrics. *Phys. Rev. B* **2002**, *65*, 115418.

(16) Etchegoin, P. G.; Ru, E. C. L.; Meyer, M. An Analytic Model for the Optical Properties of Gold. *J. Chem. Phys.* **2006**, *125*, 164705.

(17) Etchegoin, P. G.; Ru, E. C. L. Multipolar Emission in the Vicinity of Metallic Nanostructures. *J. Phys. Condens. Matter* **2006**, *18*, 1175.

(18) Curl, C. L.; Bellair, C. J.; Harris, T.; Allman, B. E.; Harris, P. J.; Stewart, A. G.; Roberts, A.; Nugent, K. A.; Delbridge, L. M. D. Refractive Index Measurement in Viable Cells Using Quantitative Phase-Amplitude Microscopy and Confocal Microscopy. *Cytometry A* **2005**, *65A*, 88–92.
(19) Kneipp, K.; Wang, Y.; Kneipp, H.; Perelman, L. T.; Itzkan, I.; Dasari, R. R.; Feld, M. S. Single Molecule Detection Using Surface-Enhanced Raman Scattering (SERS). *Phys. Rev. Lett.* **1997**, *78*, 1667–1670.
(20) Bordley, J. A.; Hooshmand, N.; El-Sayed, M. A. The Coupling between Gold or Silver Nanocubes in Their Homo-Dimers: A New Coupling Mechanism at Short Separation Distances. *Nano Lett.* **2015**, *15*, 3391–3397.
(21) Jiang, W.; Kim, B. Y. S.; Rutka, J. T.; Chan, W. C. W. Nanoparticle-Mediated Cellular Response Is Size-Dependent. *Nat. Nanotechnol.* **2008**, *3*, 145–150.
(22) Liu, Y.; Shipton, M. K.; Ryan, J.; Kaufman, E. D.; Franzen, S.; Feldheim, D. L. Synthesis, Stability, and Cellular Internalization of Gold Nanoparticles Containing Mixed Peptide-Polyethylene Glycol Monolayers. *Anal. Chem.* **2007**, *79*, 2221–2229.
(23) DeVetter, B. M.; Mukherjee, P.; Murphy, C. J.; Bhargava, R. Measuring Binding Kinetics of Aromatic Thiolated Molecules with Nanoparticles *via* Surface-Enhanced Raman Spectroscopy. *Nanoscale* **2015**, *7*, 8766–8775.
(24) Xia, X.; Yang, M.; Wang, Y.; Zheng, Y.; Li, Q.; Chen, J.; Xia, Y. Quantifying the Coverage Density of Polyethylene Glycol Chains on the Surface of Gold Nanostructures. *ACS Nano* **2012**, *6*, 512–522.
(25) Shameli, K.; Bin Ahmad, M.; Jazayeri, S. D.; Sedaghat, S.; Shabanzadeh, P.; Jahangirian, H.; Mahdavi, M.; Abdollahi, Y. Synthesis and Characterization of Polyethylene Glycol Mediated Silver Nanoparticles by the Green Method. *Int. J. Mol. Sci.* **2012**, *13*, 6639–6650.
(26) Varsányi, G. *Assignments for Vibrational Spectra of Seven Hundred Benzene Derivatives*; Wiley, 1974.
(27) Bassan, P.; Sachdeva, A.; Lee, J.; Gardner, P. Substrate Contributions in Micro-ATR of Thin Samples: Implications for Analysis of Cells, Tissue and Biological Fluids. *The Analyst* **2013**, *138*, 4139.
(28) Wu, X.; Ming, T.; Wang, X.; Wang, P.; Wang, J.; Chen, J. High Photoluminescence Yield Gold Nanocubes: For Cell Imaging and Photothermal Therapy. *ACS Nano* **2009**, *4*, 113–120.
(29) Debnath, J.; Muthuswamy, S. K.; Brugge, J. S. Morphogenesis and Oncogenesis of MCF-10A Mammary Epithelial Acini Grown in Three-Dimensional Basement Membrane Cultures. *Methods* **2003**, *30*, 256–268.
(30) Hohenester, U. Simulating Electron Energy Loss Spectroscopy with the MNPBEM Toolbox. *Comput. Phys. Commun.* **2014**, *185*, 1177–1187.
(31) Hohenester, U.; Trügler, A. MNPBEM – A Matlab Toolbox for the Simulation of Plasmonic Nanoparticles. *Comput. Phys. Commun.* **2012**, *183*, 370–381.
(32) Waxenegger, J.; Trügler, A.; Hohenester, U. Plasmonics Simulations with the MNPBEM Toolbox: Consideration of Substrates and Layer Structures. *Comput. Phys. Commun.* **2015**, *193*, 138–150.

CHAPTER 6

REFLECTIVE SUBSTRATES IN MID-INFRARED SPECTROSCOPY

6.1 Introduction

In mid-infrared spectroscopy, careful consideration of the substrate and illumination geometry are crucial for obtaining high-quality quantitative data. Illumination using transmission, transflection, or attenuated total reflectance (ATR) geometries along with transmissive salt windows (CaF_2, BaF_2, ZnSe, *etc*.) or reflective substrates (gold, aluminum, *etc*.) can influence the resulting spectra and, subsequently, hinder our ability to perform classification algorithms across measurements.[1] Additionally, with recent advances in semiconductor technology, infrared spectroscopy can now be performed using bright, monochromatic coherent light sources rather than weak, incoherent thermal sources that require the use of an interferometer. These sources, called quantum cascade lasers (QCLs), were originally developed by Jerome Faist, Federico Capasso and coworkers at Bell Labs in 1994 and have only recently become commercially available.[2] Consideration of coherent sources adds a new challenge in interpreting the effects of substrates and illumination.

While transmission may be the most ideal illumination geometry, it is often avoided because of the high cost of salt windows and issues with their toxicity and solubility. Transflectance and ATR measurements are commonly used with inexpensive low-emissivity (low-e) glass or other metal-coated glass substrates.[3–5] Reflective substrates, however, have been a subject of controversy because they exhibit an electric field standing wave (EFSW) effect that some researchers believe may cause difficulties in classification of biological materials due to spectral distortions.[6,7] However, consideration of the incoherent propagation of light and multiple collection angles has been shown to minimize the EFSW effect such it is unlikely to significantly

distort a transflectance Fourier transform infrared (FTIR) spectroscopic measurement.[8] While low-e glass is a convenient choice for a reflective substrate, because it is transparent in the visible and reflective in the infrared, the ambiguity over its structure and composition has led to some confusion over its optical properties and, consequently, its influence on infrared spectra as compared to other well-characterized metallic substrates such as gold-coated glass.

To address these concerns, and further understand the EFSW effect on reflective substrates, we present experimental characterization data of a common commercial low-e glass used for mid-infrared spectroscopy. Analytical electromagnetic calculations using Fresnel's equations show significant differences in the spectral features of gold-coated *versus* low-e glass with both transflectance and ATR illumination geometries.

6.2 Theory

An incident plane wave $\mathbf{E}_i(\mathbf{r},t)=\mathbf{E}_0 e^{i(\mathbf{k}\cdot\mathbf{r}-\omega t)}$ propagating toward an interface consisting of a half-plane with index of refraction n_1 for $z < 0$ and n_2 for $z > 0$ may be determined by solving the appropriate boundary conditions at the interface. The Fresnel coefficients for reflection ($r_{s,p}$) and transmission ($t_{s,p}$) for the perpendicular (s-polarized) and parallel (p-polarized) case may be described by the following:[9]

$$r_s = \frac{n_1 \cos\theta_i - n_2 \cos\theta_t}{n_1 \cos\theta_i + n_2 \cos\theta_t} \tag{6.1}$$

$$r_p = \frac{n_1 \cos\theta_t - n_2 \cos\theta_i}{n_1 \cos\theta_t + n_2 \cos\theta_i} \tag{6.2}$$

and

$$t_s = \frac{2n_1 \cos\theta_i}{n_1 \cos\theta_i + n_2 \cos\theta_t} \tag{6.3}$$

$$t_p = \frac{2n_1 \cos\theta_i}{n_1 \cos\theta_t + n_2 \cos\theta_i} \tag{6.4}$$

where θ_i is the incident angle and θ_t is the refracted angle. The reflectance R for either polarization is $R_s = |r_s|^2$ or $R_p = |r_p|^2$. Unpolarized light may be calculated by taking the average of both polarizations: $R = \frac{|r_s^2| + |r_p^2|}{2}$.

Layered planar media may be calculated using the transfer-matrix method (TMM) technique. The TMM may be formulated in terms of a phase-shift matrix $\mathbf{U}_v$ and a refraction matrix $\mathbf{W}_{v,v+1}$:[10–12]

$$\mathbf{U}_v = \begin{pmatrix} e^{i\delta_v} & 0 \\ 0 & e^{-i\delta_v} \end{pmatrix} \tag{6.5}$$

$$\mathbf{W}_{v,v+1} = \begin{pmatrix} 1 & r_{v,v+1} \\ r_{v,v+1} & 1 \end{pmatrix} \frac{1}{t_{v,v+1}} \tag{6.6}$$

where $r_{v,v+1}$ and $t_{v,v+1}$ are the Fresnel coefficients calculated at each interface. The phase-shift is equal to $\delta_v = 2\pi n_v h_v \cos\theta_v / \lambda_0$ where h_v is the layer thickness, n_v is the index of refraction, and θ_v is the entrance angle within each layer. The angle of propagation for each layer, for N interfaces, was determined using Snell's law:

$$n_0 \sin\theta_0 = \ldots = n_N \sin\theta_N \tag{6.7}$$

The partial system transfer matrix for each layer is represented by:

$$\tilde{\mathbf{S}}_{\mathrm{v}} = \mathbf{U}_{\mathrm{v}}\mathbf{W}_{\mathrm{v,v+1}} = \begin{pmatrix} \mathrm{e}^{\mathrm{i}\delta_{\mathrm{v}}} & 0 \\ 0 & \mathrm{e}^{-\mathrm{i}\delta_{\mathrm{v}}} \end{pmatrix} \begin{pmatrix} 1 & r_{\mathrm{v,v+1}} \\ r_{\mathrm{v,v+1}} & 1 \end{pmatrix} \frac{1}{t_{\mathrm{v,v+1}}} \tag{6.8}$$

$$\begin{pmatrix} E_{\mathrm{v}}^{+} \\ E_{\mathrm{v}}^{-} \end{pmatrix} = \tilde{\mathbf{S}}_{\mathrm{v}} \begin{pmatrix} E_{\mathrm{v+1}}^{+} \\ E_{\mathrm{v+1}}^{-} \end{pmatrix} \tag{6.9}$$

where E_{v}^{+} and E_{v}^{-} represent a forward and backward propagating wave, respectively. The system transfer matrix for the entire multilayered system is:

$$\mathbf{S} = \begin{pmatrix} S_{11} & S_{12} \\ S_{21} & S_{22} \end{pmatrix} = \frac{1}{t_{0,1}} \begin{pmatrix} 1 & r_{0,1} \\ r_{0,1} & 1 \end{pmatrix} \prod_{\mathrm{i=1}}^{\mathrm{N-1}} \mathbf{U}_{\mathrm{i}}\mathbf{W}_{\mathrm{i,i+1}} \tag{6.10}$$

The Fresnel coefficients of the multilayered system may then be calculated in terms of the incident and exiting electric field:

$$\begin{pmatrix} E_{0}^{+} \\ E_{0}^{-} \end{pmatrix} = \mathbf{S} \begin{pmatrix} E_{\mathrm{N}}^{+} \\ 0 \end{pmatrix} \tag{6.11}$$

$$r = \frac{E_{0}^{-}}{E_{0}^{+}} = \frac{S_{21}}{S_{11}} \tag{6.12}$$

$$t = \frac{E_{\mathrm{N}}^{+}}{E_{0}^{+}} = \frac{1}{S_{11}} \tag{6.13}$$

where E_{N}^{-} is set to 0 because there are not backward propagating waves after the last interface. The above discussion of Fresnel's equations assumes excitation by coherent, monochromatic plane waves. This technique is susceptible to Fabry-Perot resonances when layer thicknesses approach that of the excitation wavelength. In many cases, incoherent illumination or propagation through inhomogeneous layers is desirable for comparison to FTIR measurements or

disordered biological materials. Incoherent propagation was modeled by transforming the refraction matrix to an intensity matrix. The phase matrix may be discarded for completely dispersive incoherent layers or becomes exponentially decaying for absorptive indices of refraction.[11] Absorption spectra were simulated by taking a ratio between the reflectance of the sample with and without the absorbing layer:

$$A = -\log_{10} \frac{R_{\text{sample}}}{R_{\text{background}}} \tag{6.14}$$

To examine the influence of substrate type, each band was normalized to 3912.5 cm^{-1} and a percent difference between the ratio of bands for each substrate was calculated:

$$\%\,\text{difference} = \frac{\left| A^{\text{Au}} / A^{\text{Au}}_{3912} - A^{\text{low-e}} / A^{\text{low-e}}_{3912} \right|}{A^{\text{low-e}} / A^{\text{low-e}}_{3912}} \times 100\% \tag{6.15}$$

where A^{Au} and $A^{\text{low-e}}$ represent the integrated band intensity of gold and low-e, respectively.

6.3 Results and discussion

In order to alleviate confusion surrounding the optical properties of low-e glass, we first sectioned commercially available low-e using a focused ion beam and mounted it to a copper grid appropriate for transmission electron microscopy (TEM). As shown in Figure 6.1, the TEM cross-sectional images clearly show two thin layers of silver protected by several layers of metal oxide atop a glass substrate. Note that the platinum layer was added purely for mechanical stability during cross sectioning and is not a component of low-e glass. Figure 6.2 shows the confirmation of each using energy-dispersive x-ray spectroscopy (EDS). Two layers of ZnO (corresponding to 40 and 60 nm) were clearly visible from spatially-resolved EDS. The third layer and thinnest layer of ZnO was heavily obscured by the copper background signal such that

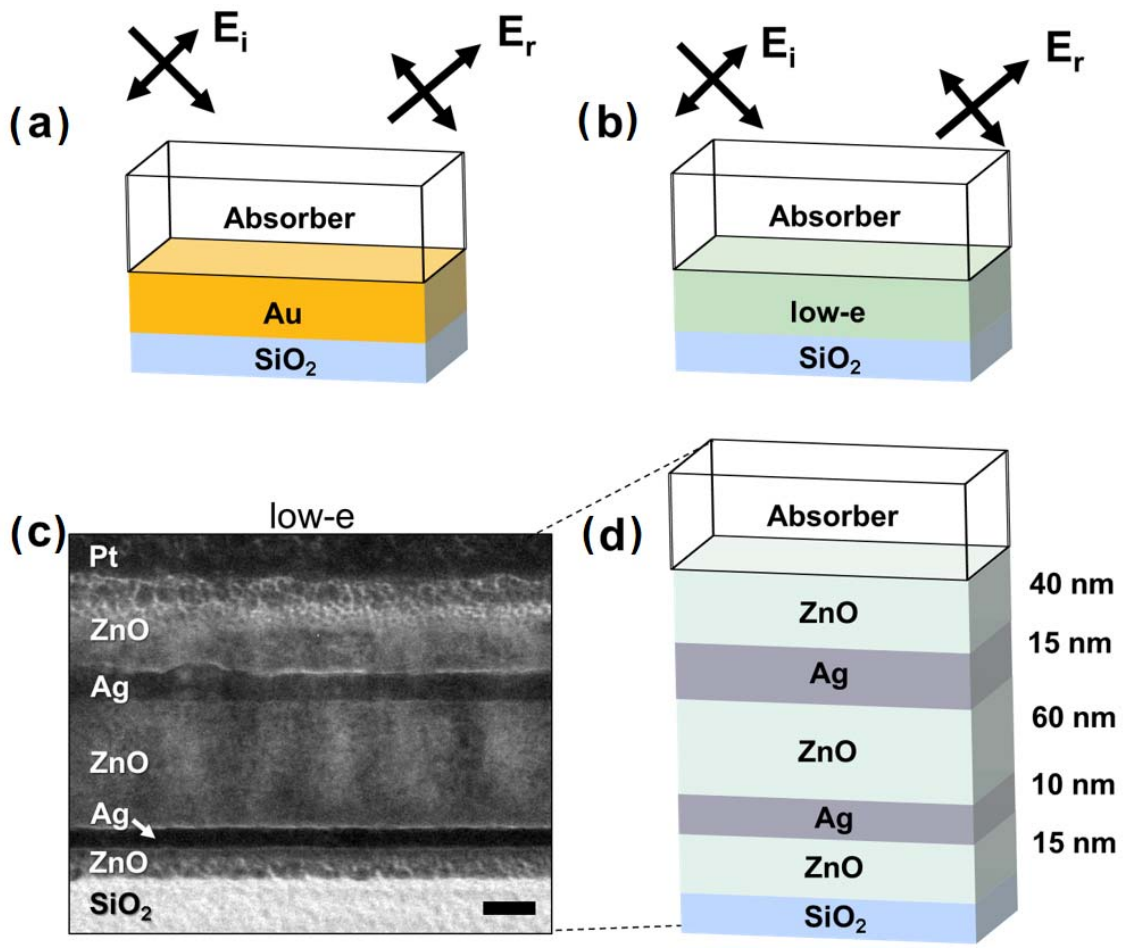

Figure 6.1. Transflectance configuration for an incident plane wave for two common mid-IR reflective substrates (a) gold (typical thickness: 100 nm Au) and (b) low-e glass with an absorbing layer deposited on the surface. (c) Transmission electron micrograph of a cross section of low-e glass. The platinum layer was added for mechanical stability during cross sectioning and is not a constituent of low-e glass. Scale bar: 25 nm. (d) Schematic of multilayered low-e glass model used for simulations.

it was not possible to resolve with EDS. The structure reported here is significantly different than previous studies of the same low-e glass (namely, a single layer of Ag and SnO_2 layers rather than ZnO) and is the only experimentally determined structure of low-e glass reported to date.[6,7] Note that ZnO has a frequency-dependent and relatively lower index of refraction ($n \approx 1.6 – 1.9$) as compared to the SnO_2 ($n = 2$) layers used previously for modeling low-e glass.

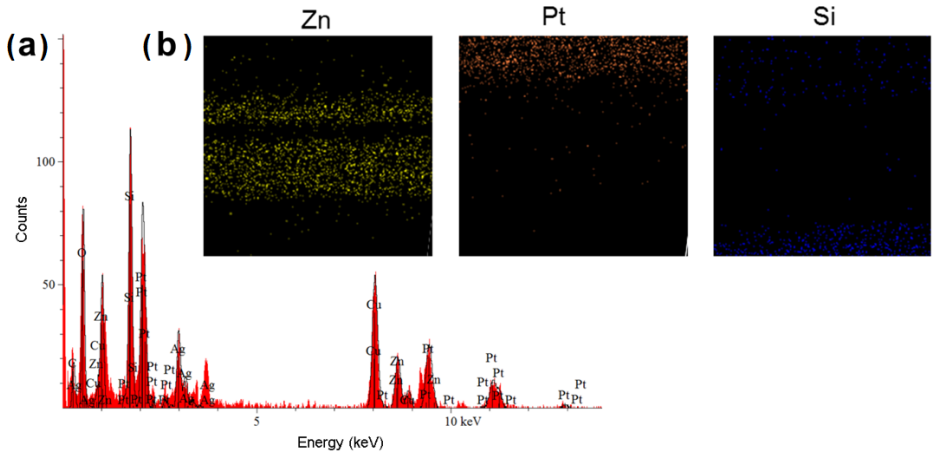

Figure 6.2. (a) EDS spectra of a representative cross section of low-e glass. Fitting revealed the presence of Ag, Zn, Si, and O along with signal from the Pt and Cu supporting structures. Minimal carbon contamination was observed. (b) Spatially resolved EDS illustrating the position of Zn, Pt, and Si. Two layers containing Zn were clearly observed. The thin Zn layer at the Si-ZnO interface was not resolvable.

As shown in Figure 6.3, significant differences in reflectivity between the previously reported structures and the experimentally determined structure exist.

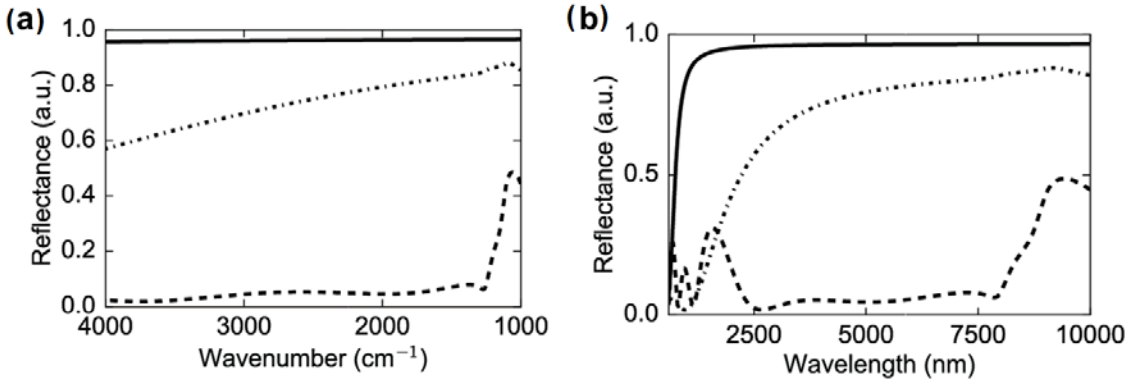

Figure 6.3. Reflectance spectra of low-e glass represented in terms of (a) wavenumber and (b) wavelength using different models for unpolarized coherent light at normal incidence. The experimentally derived model (solid) consists of 40 nm ZnO, 15 nm Ag, 60 nm ZnO, 10 nm Ag, 15 nm ZnO on a SiO_2 substrate. Previously reported models consist of (dot-dash) 50 nm SnO_2, 5 nm Ag, 50 nm SnO_2 and (dash) 300 nm SnO_2, 1 nm Ag, and 300 nm SnO_2 on a SiO_2 substrate. Note that the index of refraction used for SnO_2 was $n = 2 + 0i$.

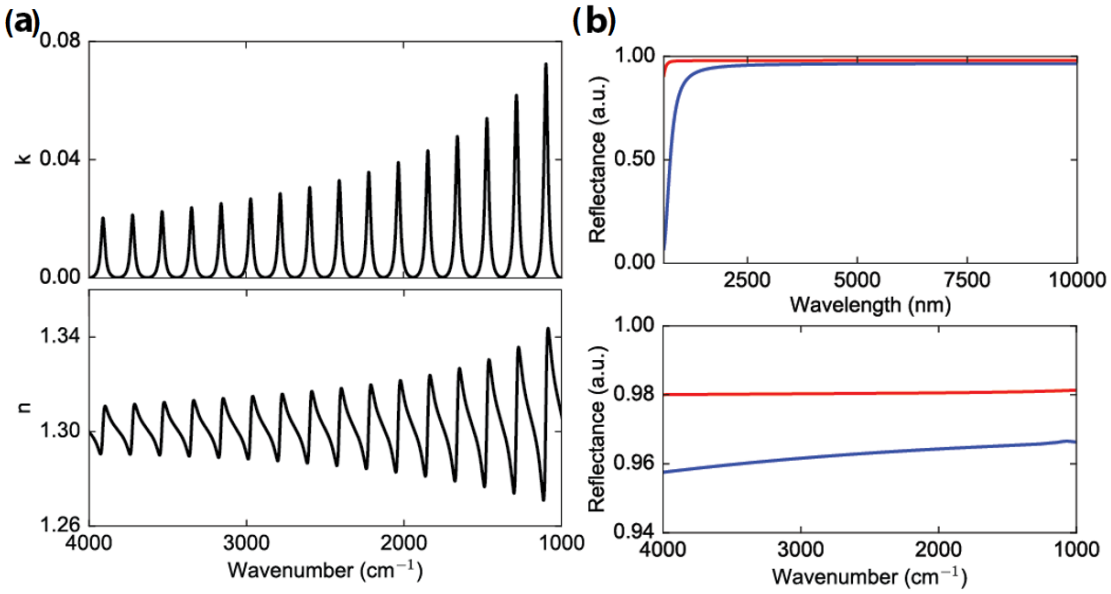

Figure 6.4. (a) Real (*n*) and imaginary (*k*) index of refraction of theoretical absorber consisting of several equally spaced Lorentzian bands. (b) Calculated reflectivity of 100 nm gold-coated (red) and low-e (blue) glass in terms of wavelength and wavenumber excited at normal incidence with monochromatic plane waves.

Figure 6.4 shows the reflectance spectra calculated using the TMM method to simulate the spectra of a theoretical absorber consisting of a series of equally spaced Lorentzian bands from 4000 – 1000 cm^{-1}. The absorptive, or imaginary, part of the refractive index was calculated by assuming each band had a maximum attenuation coefficient of 1000 cm^{-1}. Kramers-Kronig relations were used to calculate the dispersive part of the refractive index centered around a value of 1.3. At first glance, the reflectivity of gold versus low-e glass may seem negligible in the mid-IR but the reflectivity of low-e glass has a distinct curvature that is not present in the gold-coated substrate. A small contribution at 1100 cm^{-1} in the low-e reflectance spectra is attributed to a Si-O stretching mode.

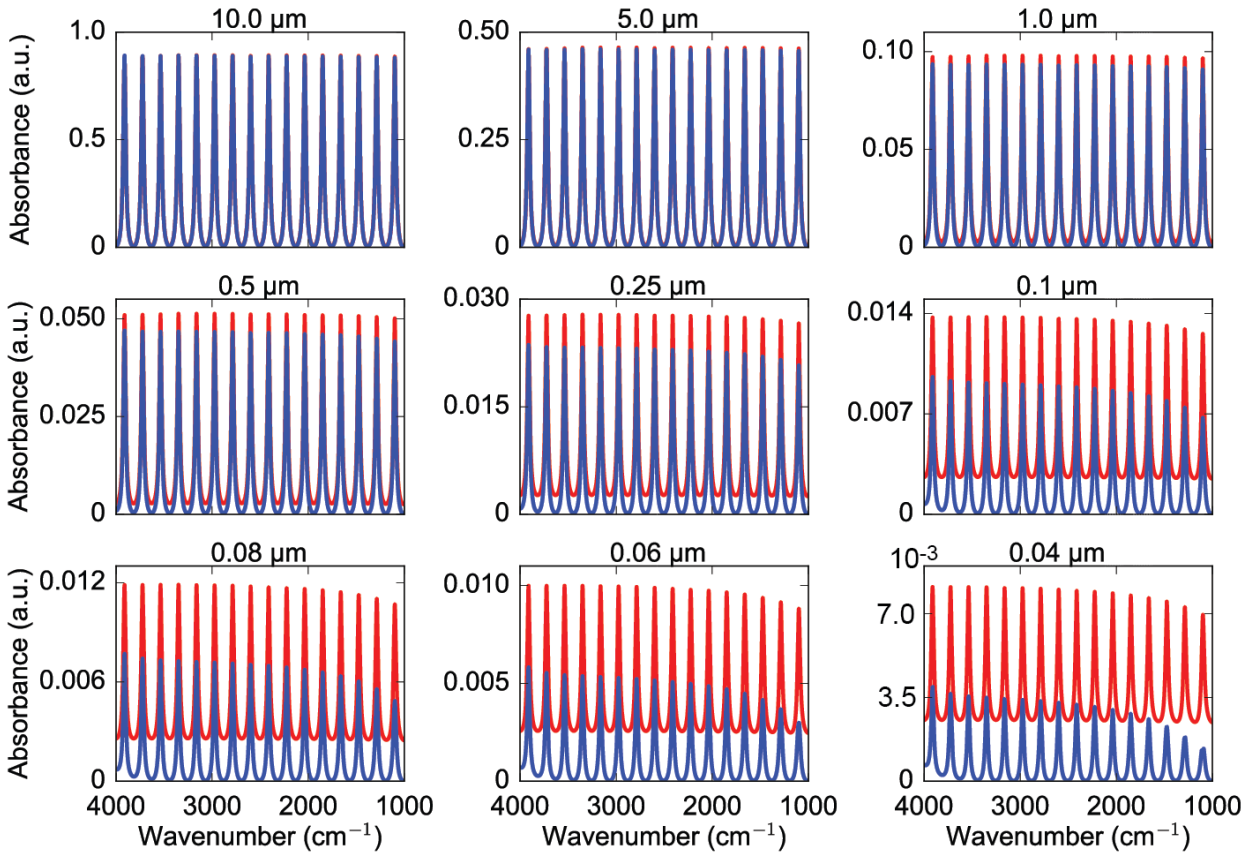

Figure 6.5. Simulated absorbance spectra (red: gold-coated glass; blue: low-e glass) for absorber thicknesses ranging from 10 μm – 0.04 μm. Unpolarized plane wave excitation at an angle of incidence of 30 degrees and incoherent light propagation throughout all layers was assumed.

Transflectance simulations at an angle of incidence of 30 degrees were performed to evaluate differences in the spectral characteristics of gold-coated versus low-e glass as described in Figure 6.5. The absorber thickness was varied from 10 μm – 0.04 μm and incoherent propagation of light throughout each layer was assumed. This particular configuration mimics that of an FTIR instrument at a single collection angle. It should be noted that there are minimal differences in the spectra for other collection angles ranging from 30 – 45 degrees. As anticipated, the standing wave effect was not observed for incoherent propagation. For thick samples, the spectra has negligible differences. For practical FTIR measurements, this indicates that thick films of sample are minimally affected by reflective substrate choice. As the absorber

thicknesses decrease, we observe that low-e has decreased band height toward shorter wavenumber as a consequence of increased penetration into the multilayered low-e structure. To quantify these differences, we evaluated the intensities of each band and normalized to 3912 cm^{-1} to calculate a percent difference between the gold and low-e band height, as described in Figure 6.6. Thin absorber films of have significant differences in band height ratios up to 43% for a 40 nm thick film.

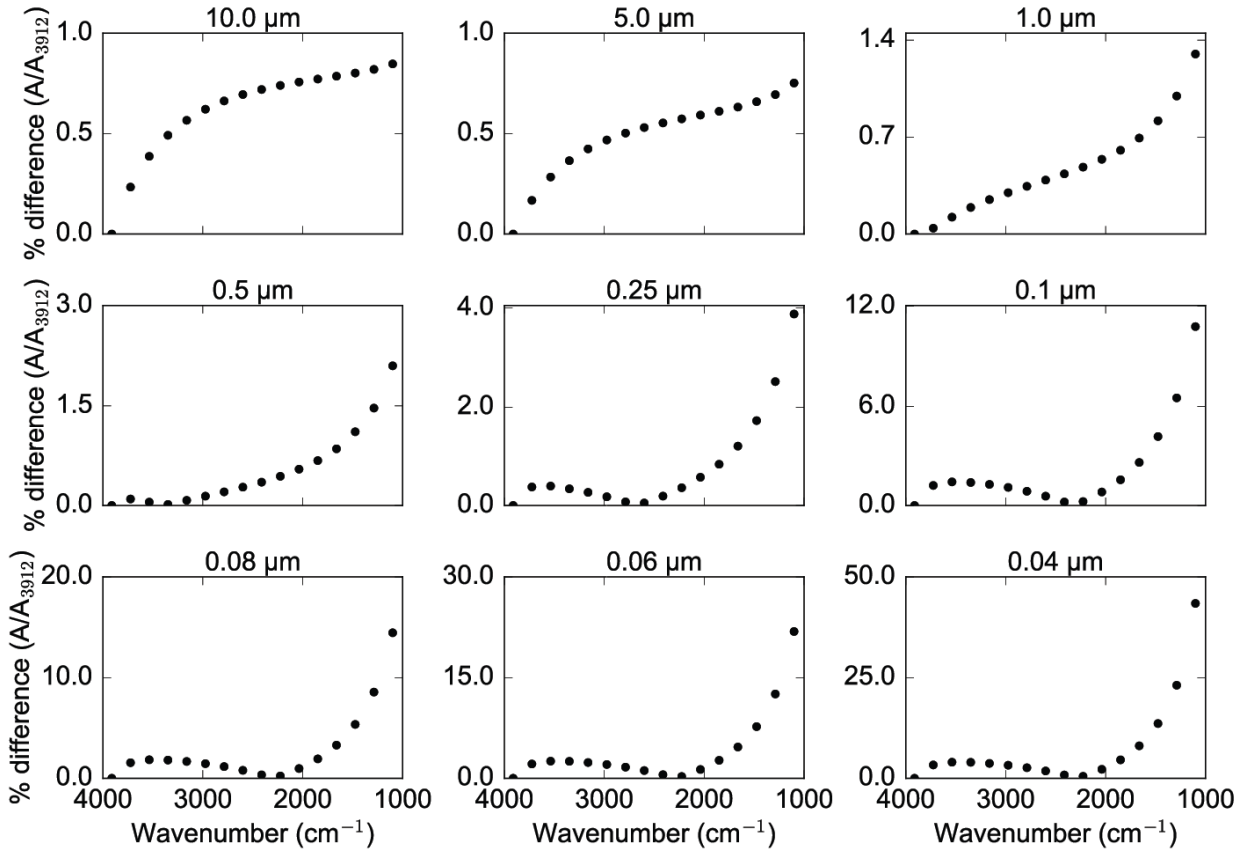

Figure 6.6. Calculated percent difference between band height ratios (A/A_{3912}) of gold-coated and low-e glass for absorber thicknesses ranging from 10 μm – 0.04 μm. Unpolarized plane wave excitation at an angle of incidence of 30 degrees and incoherent light propagation throughout all layers was assumed.

With the emergence of QCLs, it is also important to consider coherent sources and how substrates can influence the measured spectra. Using the same absorber and film thicknesses,

simulations at normal incidence with unpolarized coherent light were performed, as shown in Figure 6.7. Normal incidence results in an increased penetration depth into the multilayered

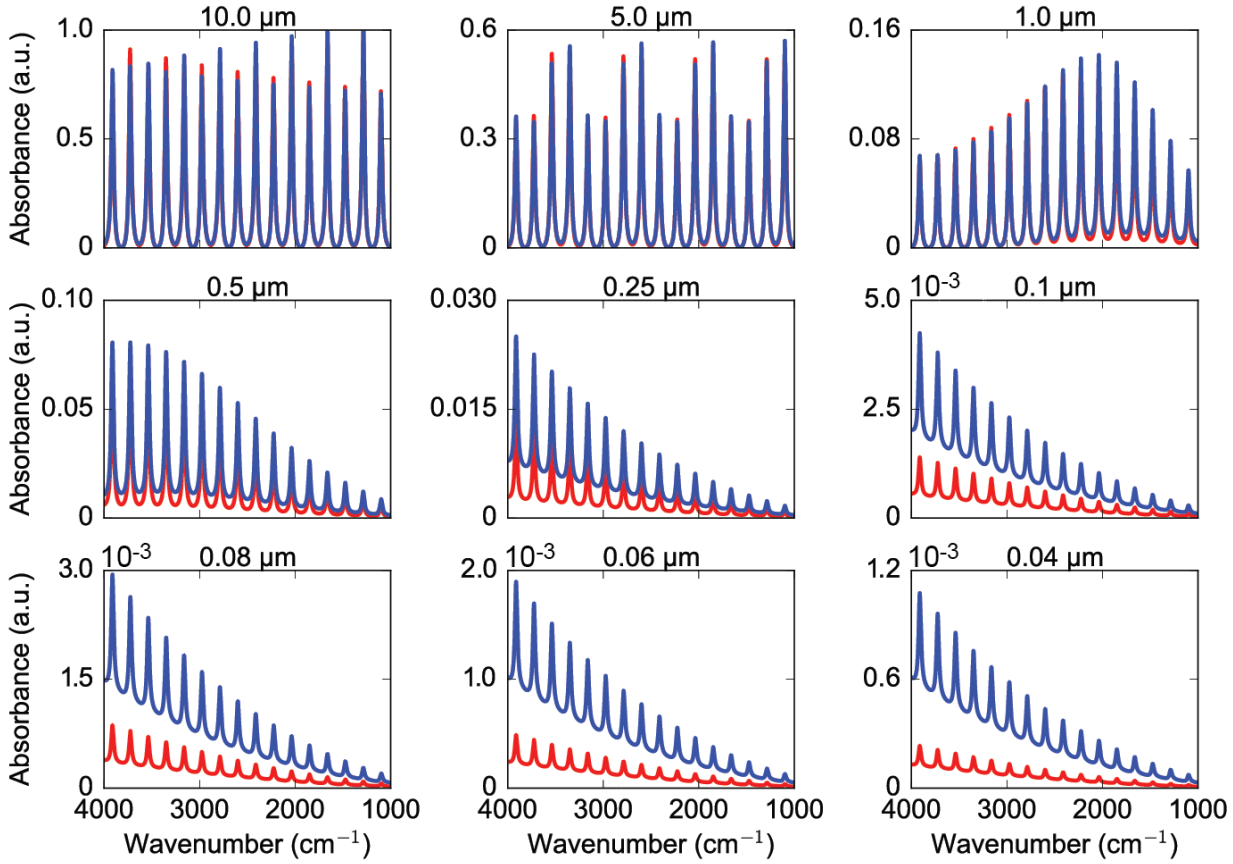

Figure 6.7. Simulated absorbance spectra (red: gold-coated glass; blue: low-e glass) for absorber thicknesses ranging from 10 μm – 40 nm. Unpolarized coherent plane wave excitation at normal incidence was assumed. The EFSW effect was observed for absorber layers on the order of the excitation wavelength.

low-e structure. Here, the EFSW is evident for thick absorber layers. For homogeneous films where the EFSW effect is likely to occur most noticeably, difficulties in classification will arise, as described by Bassan and coworkers.[6] The percent difference for each absorber thickness was also calculated in Figure 6.8. The EFSW effect causes significant (nearly 20%) differences in band ratios between the gold-coated and low-e glass. Unlike in the incoherent case, thick absorbers exhibit a significant A/A_{3912} ratio because the curvature of the reflectivity of low-e

glass in combination with the EFSW cause sudden shifts in peak height. At absorber thicknesses below 0.5 μm where the EFSW effect is negligible there is still a considerable difference between these two substrates (up to 15%). This primarily arises from a difference in frequency-dependent penetration of light into the low-e.

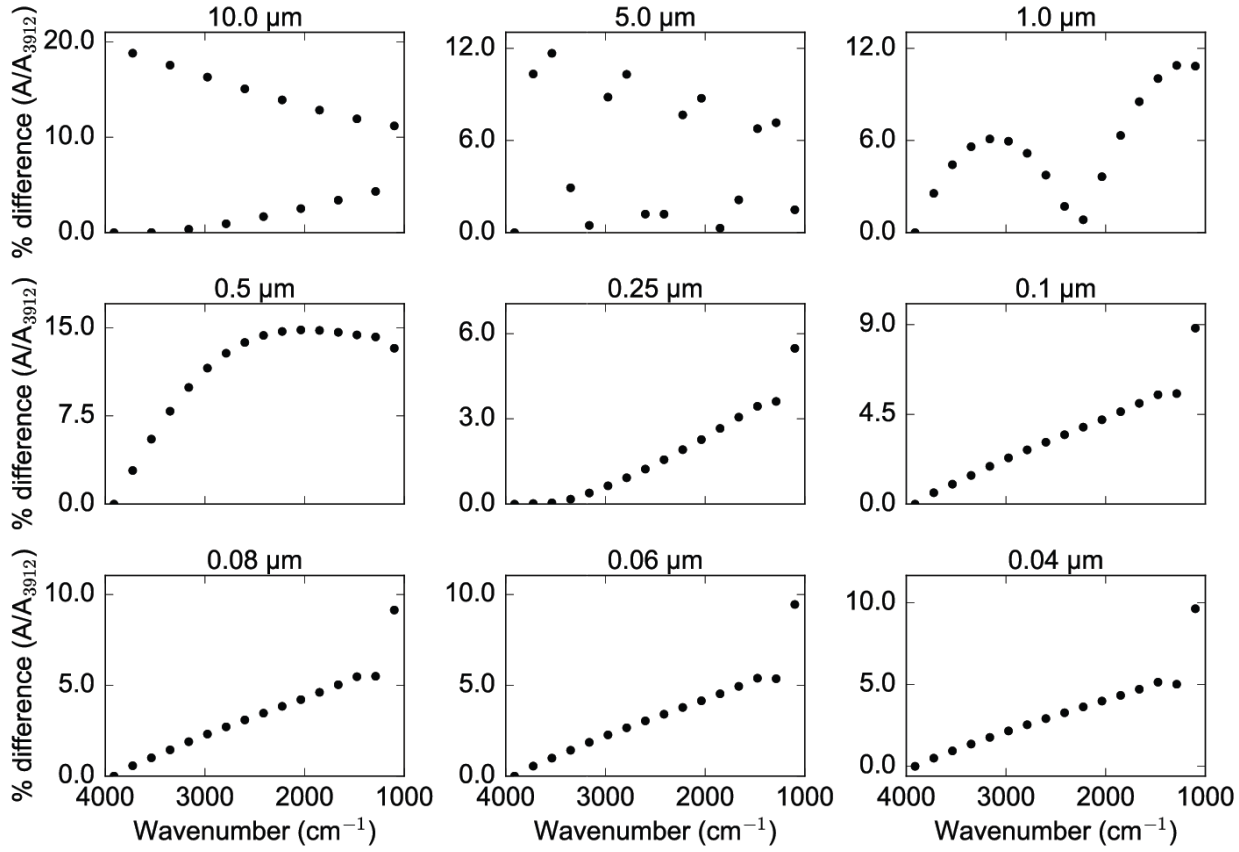

Figure 6.8. Calculated percent difference between band height ratios (A/A_{3912}) of gold-coated and low-e glass for absorber thicknesses ranging from 10 μm – 0.04 μm. Unpolarized coherent plane wave excitation at normal incidence was assumed.

ATR-FTIR is a common technique to probe the chemical information of thin films, liquids, and biological materials that would otherwise yield a poor or unusable transflectance infrared signature. For biological materials, which are highly susceptible to scattering due to

inhomogeneities in their morphology, ATR is a convenient method for minimizing undesirable scattering that can lead to spectral distortions. In the case of Ge crystals (n = 4 + 0i), ATR

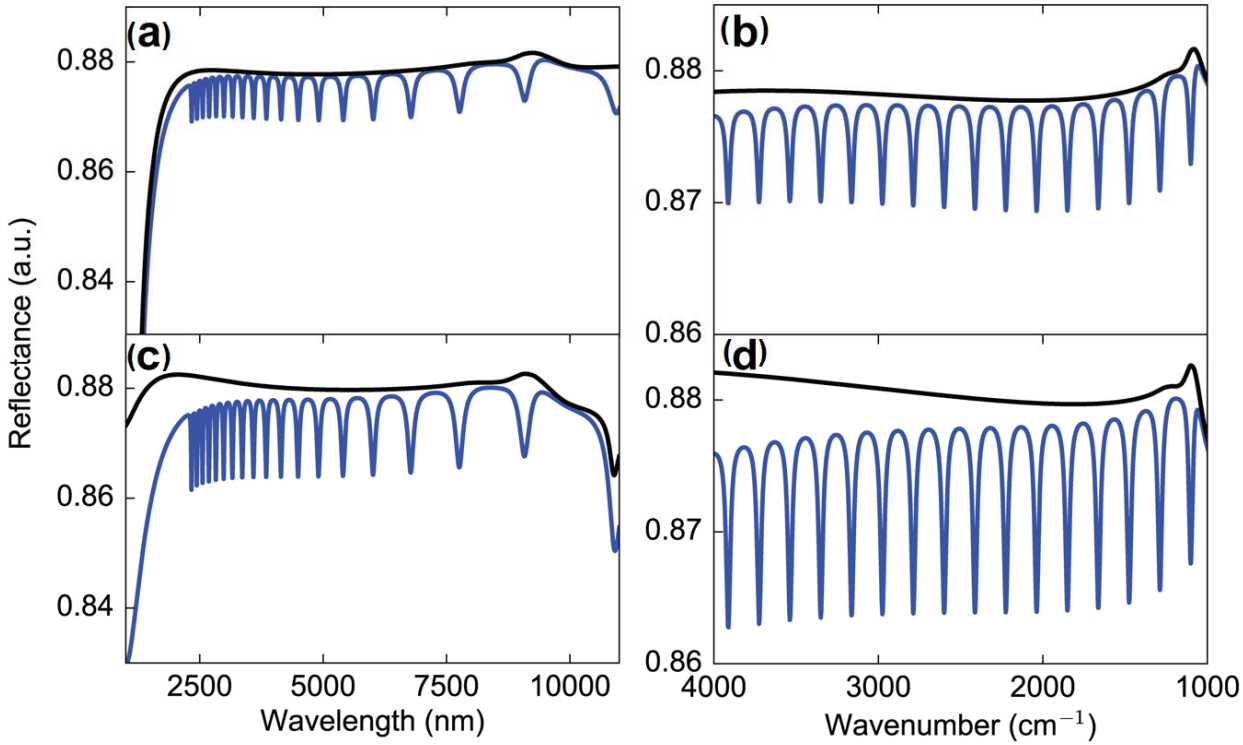

Figure 6.9. Simulated ATR spectra (black: without absorber; blue: with a 10 nm thick absorbing layer) of low-e glass for an angle of incidence of (a) 23 degrees in terms of wavelength, (b) 23 degrees in terms of wavenumber, (c) 30 degrees in terms of wavelength, and (d) 30 degrees in terms of wavenumber.

attachments to FTIR instruments are commonly designed to have angles of incidence ranging from 23 – 30 degrees to ensure total internal. Slightly below 23 degrees, surface waves for both gold-coated and low-e glass can be generated and lead to a reduction in reflectance. Simulated ATR spectra in Figures 6.9 and 6.10 were calculated by assuming a Ge crystal was placed in contact with a low-e glass slide. Using the experimentally derived structure, the Si-O stretch at 1100 cm^{-1} was observed.

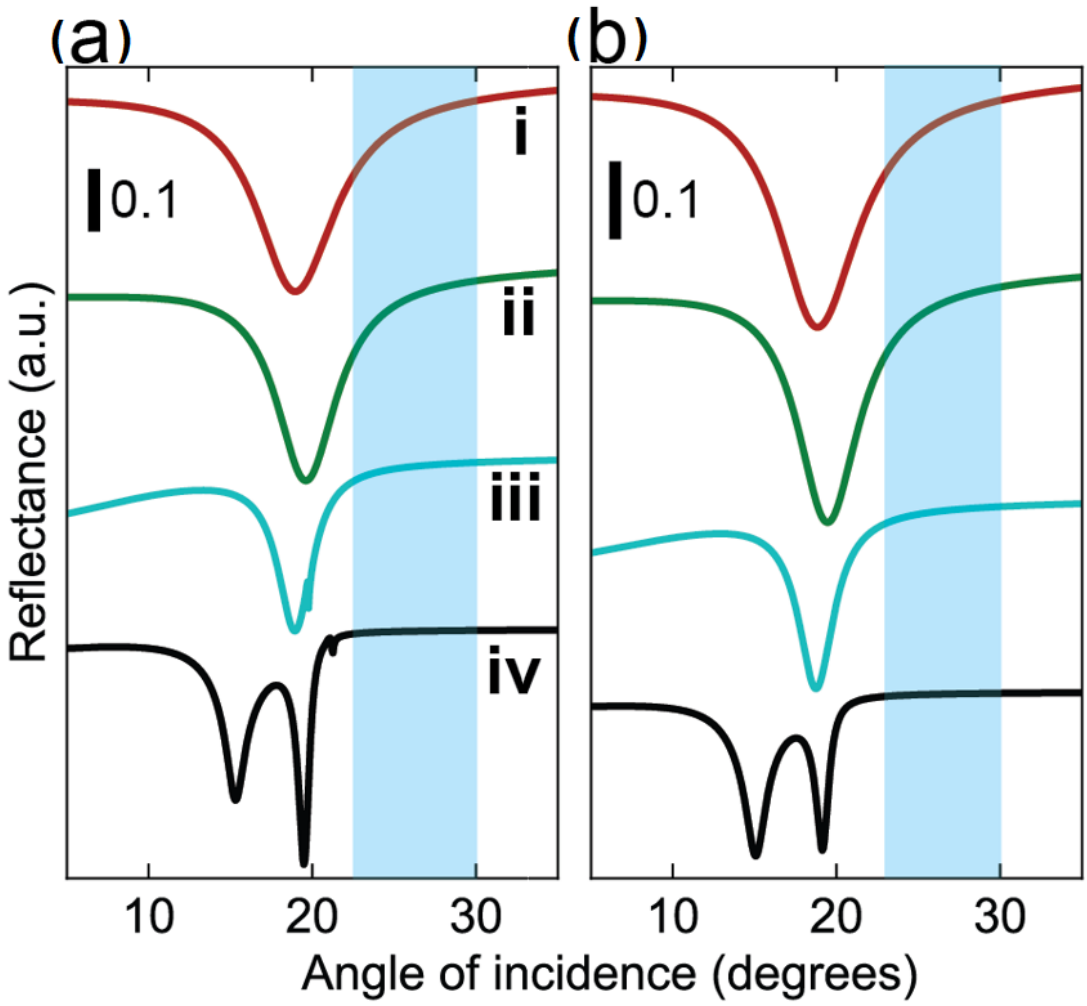

Figure 6.10. Simulated reflectance spectra of (a) low-e and (b) gold-coated (100 nm) glass for unpolarized monochromatic light in ATR mode and an absorber thickness of 1.5 μm. Excitation wavelength (i) 10 μm, (ii) 7.5 μm, (iii) 5.0 μm, and (iv) 2.5 μm. The highlighted region (blue) corresponds to angles of incidence (23 – 30 degrees) found in some ATR attachments.

In Figure 6.11, ATR-FTIR absorption spectra were calculated for gold-coated and low-e glass slides. The background reflectance $R_{background}$ was calculated by placing the Ge crystal in direct contact with the substrate. As expected, the choice of substrate only influenced thin absorbing layers (less than the wavelength of light) where light could partially penetrate into the glass. Thick absorber layers had negligible differences in absorption spectra for either substrate.

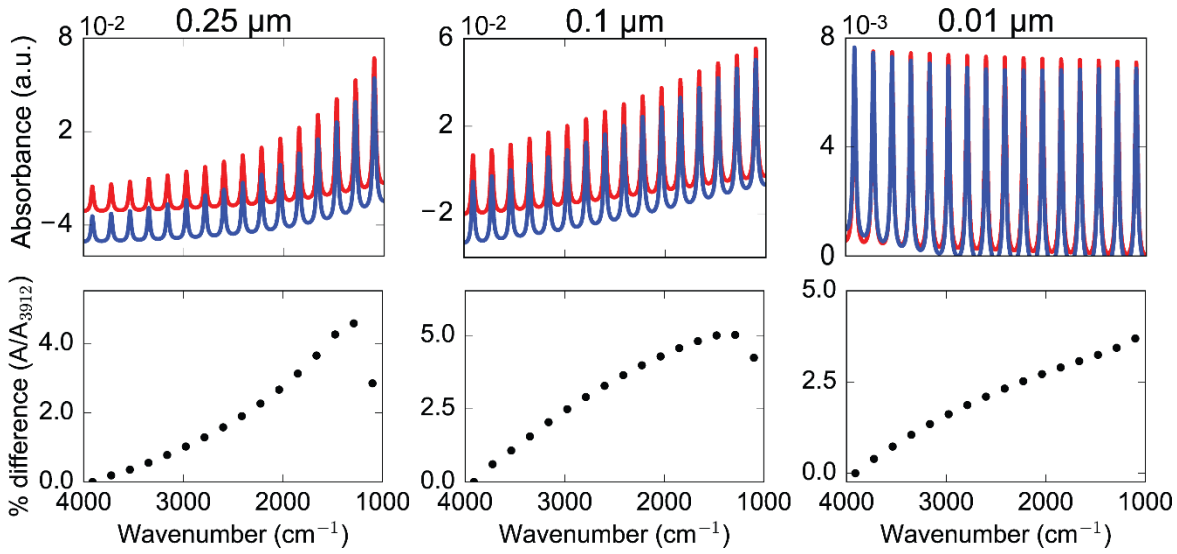

Figure 6.11. Simulated ATR spectra (absorbance and A/A_{3912}) of gold-coated and low-e glass at an angle of incidence of 30 degrees for thicknesses 0.25 μm, 0.1 μm, and 0.01 μm.

Furthermore, we can visualize the field penetrating the substrate as illustrated in Figure 6.12. As shown, we observe some penetration into the SiO_2 layer at an angle of incidence of 30 degrees.

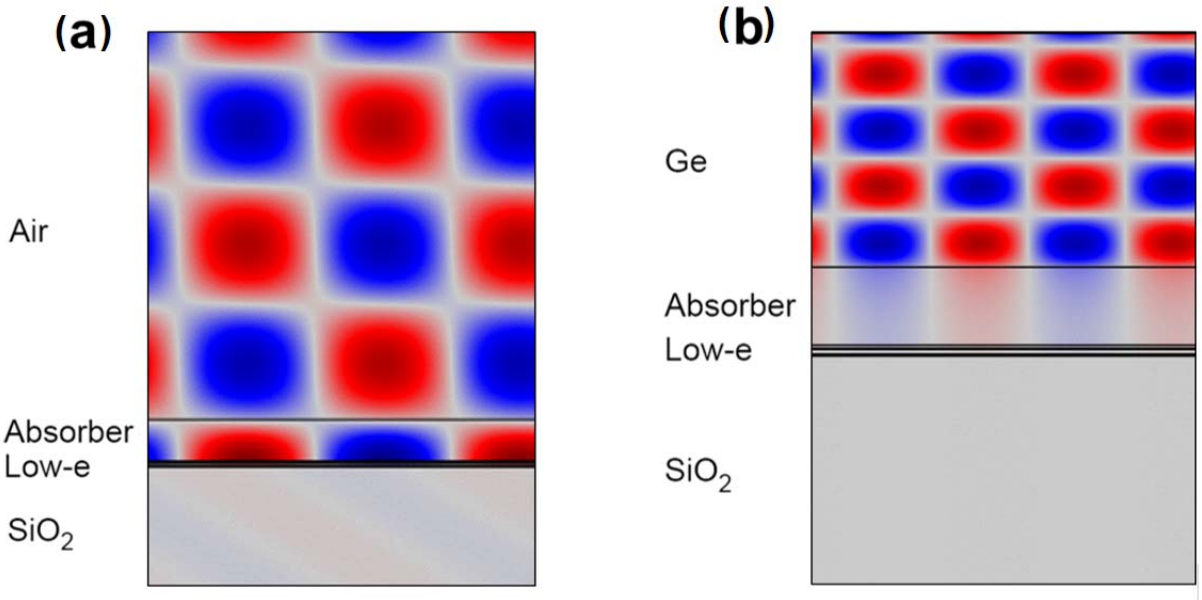

Figure 6.12. Simulated schematic illustration of the field distribution (Hz) for a p-polarized plane wave incident (λ = 5 μm) on a low-e substrate in (a) transflection mode and (b) ATR mode at an angle of incidence of 30 degrees. The absorber thickness was set to 0.5 μm.

6.4 Experimental

Instrumentation. Transmission electron microscopy was performed on a JEOL 2010F TEM with an accelerating voltage of 200 kV. Scanning transmission electron microscopy/EDS were performed on a JEOL 2010F TEM with a probe size of 0.5 nm. Focused ion beam (FIB) cross sectioning was performed on an FEI Helios NanoLab 600i FIB.

Simulations. Field calculations were performed with COMSOL Multiphysics 5.0 using the RF Module. Analytical calculations were performed with either MATLAB or Python (NumPy). Gold and silver optical constants were obtained from an empirically fit Drude model and extended up to mid-infrared frequencies, as described elsewhere.[13,14] Silicon dioxide's optical constants were obtained from Kischkat and coworkers.[15] The index of refraction of zinc oxide was assumed to be completely dispersive and calculated using the Sellmeier equation:[16] $n^2 = 2.81418 + \frac{.87968\lambda^2}{\lambda^2 - .3042^2} - .00711\lambda^2$. The complex index of refraction of tin oxide was calculated using the Drude model assuming a carrier density of $n_e = 3.5 \times 10^{26}$ m^{-3}, mobility $\mu = 4 \times 10^{-3}$ cm^2/Vs, and high-frequency permittivity limit $\varepsilon_\infty = 3.85$.[17] Germanium was assumed to have a constant index of refraction of $n = 4 + 0i$.

6.5 Conclusion

There exists some disagreement about the reliability of transflectance measurements using reflective substrates. We have analyzed a series of Lorentzian bands in the mid-IR for both gold-coated and low-e glass in order to help alleviate these concerns. Low-e glass, in particular, is desirable because it is low cost, disposable, and is optically transparent. Nonetheless, all reflective substrates are subject to the EFSW effect and therefore, we must treat each reflective substrate carefully. Our simulated results indicate that there are indeed spectral differences

between gold and low-e for coherent and incoherent propagation of light through the multilayers. For FTIR measurements, it the difference between substrates is minimal when the absorber thickness approaches that of the wavelength of light. In contrast, coherent measurements using devices such as QCLs are significantly more susceptible to the EFSW effect and correspondingly spectral distortions across substrates. ATR measurements show small differences between substrates but also have a Si-O contribution at 1100 cm^{-1}, which can distort nearby bands.

6.6 References

(1) Baker, M. J.; Trevisan, J.; Bassan, P.; Bhargava, R.; Butler, H. J.; Dorling, K. M.; Fielden, P. R.; Fogarty, S. W.; Fullwood, N. J.; Heys, K. A.; *et al.* Using Fourier Transform IR Spectroscopy to Analyze Biological Materials. *Nat. Protoc.* **2014**, *9*, 1771–1791.

(2) Faist, J.; Capasso, F.; Sivco, D. L.; Sirtori, C.; Hutchinson, A. L.; Cho, A. Y. Quantum Cascade Laser. *Science* **1994**, *264*, 553–556.

(3) Cui, L.; Butler, H. J.; Martin-Hirsch, P. L.; Martin, F. L. Aluminum Foil as a Potential Substrate for ATR-FTIR, Transflection FTIR or Raman Spectrochemical Analysis of Biological Specimens. *Anal. Methods* **2015**.

(4) Rafferty, D. W.; Virnelson, C. A Novel Reflective FT-IR Microscopy Method. *Spectroscopy* **1997**, *12*, 42–44.

(5) Cohen, J. A.; Virnelson, R. C. FT-IR Spectrometer Window and Method. US5160826 A, November 3, 1992.

(6) Bassan, P.; Lee, J.; Sachdeva, A.; Pissardini, J.; Dorling, K. M.; Fletcher, J. S.; Henderson, A.; Gardner, P. The Inherent Problem of Transflection-Mode Infrared Spectroscopic Microscopy and the Ramifications for Biomedical Single Point and Imaging Applications. *The Analyst* **2013**, *138*, 144–157.

(7) Bassan, P.; Sachdeva, A.; Lee, J.; Gardner, P. Substrate Contributions in Micro-ATR of Thin Samples: Implications for Analysis of Cells, Tissue and Biological Fluids. *The Analyst* **2013**, *138*, 4139.

(8) Wrobel, T. P.; Wajnchold, B.; Byrne, H. J.; Baranska, M. Electric Field Standing Wave Effects in FT-IR Transflection Spectra of Biological Tissue Sections: Simulated Models of Experimental Variability. *Vib. Spectrosc.* **2013**, *69*, 84–92.

(9) Jin, J.-M. *Theory and Computation of Electromagnetic Fields*; Wiley: New York, 2010.

(10) Knittl, Z. *Optics of Thin Films: An Optical Multilayer Theory*; Wiley: New York, 1976.

(11) Troparevsky, M. C.; Sabau, A. S.; Lupini, A. R.; Zhang, Z. Transfer-Matrix Formalism for the Calculation of Optical Response in Multilayer Systems: From Coherent to Incoherent Interference. *Opt. Express* **2010**, *18*, 24715.

(12) Katsidis, C. C.; Siapkas, D. I. General Transfer-Matrix Method for Optical Multilayer Systems with Coherent, Partially Coherent, and Incoherent Interference. *Appl. Opt.* **2002**, *41*, 3978.

(13) Etchegoin, P. G.; Ru, E. C. L. Multipolar Emission in the Vicinity of Metallic Nanostructures. *J. Phys. Condens. Matter* **2006**, *18*, 1175.
(14) Etchegoin, P. G.; Ru, E. C. L.; Meyer, M. An Analytic Model for the Optical Properties of Gold. *J. Chem. Phys.* **2006**, *125*, 164705.
(15) Kischkat, J.; Peters, S.; Gruska, B.; Semtsiv, M.; Chashnikova, M.; Klinkmüller, M.; Fedosenko, O.; Machulik, S.; Aleksandrova, A.; Monastyrskyi, G.; *et al.* Mid-Infrared Optical Properties of Thin Films of Aluminum Oxide, Titanium Dioxide, Silicon Dioxide, Aluminum Nitride, and Silicon Nitride. *Appl. Opt.* **2012**, *51*, 6789–6798.
(16) Bass, M.; DeCusatis, C.; Enoch, J.; Lakshminarayanan, V.; Li; G.; MacDonald, C.; Mahajan, V.; Van Strylan, E.; Handbook of Optics, 3rd ed. Volume IV: Optical Properties of Materials, Nonlinear Optics, Quantum Optics; McGraw Hill, 2009.
(17) Haitjema, H.; Elich, J. The Physical Properties of Fluorine-Doped Tin Dioxide Films and the Influence of Ageing and Impurity Effects. *Sol. Energy Mater.* **1987**, *16*, 79–90.

CHAPTER 7

COHERENT NANOAREA ELECTRON DIFFRACTION OF AU@AG NANORODS REVEALS STRUCTURAL INFORMATION

7.1 Introduction

The structural properties of gold and gold-silver (Au@Ag) core-shell nanorods were analyzed using coherent nanoarea electron diffraction (NED) and high-angle annular dark-field scanning transmission electron microscopy (HAADF-STEM). We observed bending and twisting in gold nanorods which was subsequently reduced by the epitaxial growth of a silver shell.

Refinement in the synthesis of colloidal plasmonic nanocrystals has recently led to exciting advances in catalysis,[1,2] imaging and sensing,[3–5] and drug delivery.[6,7] Typically composed of coinage metals (gold, silver, or copper), plasmonic nanocrystals are particularly useful from an optical sensing perspective because of their ability to confine electromagnetic fields at sub-diffraction-limited dimensions. This confinement or localization of incident light leads to a resonance condition called the localized surface plasmon resonance (LSPR), resulting in their brilliant optical properties.

Recently, bimetallic nanostructures have garnered much attention as efforts to improve and tune the optical, magnetic, or catalytic properties of plasmonic nanocrystals have intensified. Two classes of bimetallic nanocrystals exist: alloys and core-shell structures.[8,9] Alloys are typically formed *via* co-reduction in the presence of two metallic precursors or through a sacrificial template and galvanic replacement. Gold-silver nanocages, for example, have been successfully applied to a wide variety of biomedical imaging, chemical sensing, and catalysis applications.[1,10,11] The second class called core-shell consists of a shell grown around a core material. Several common core-shell nanostructures include Au@Pd, Au@Ag, and

Fe_3O_4@Au.[4,8,12] Regardless of classification, bimetallic nanocrystals are especially attractive because the resulting nanostructure gains useful properties of the shell while maintaining many of the desirable properties of the core.

7.2 Results and discussion

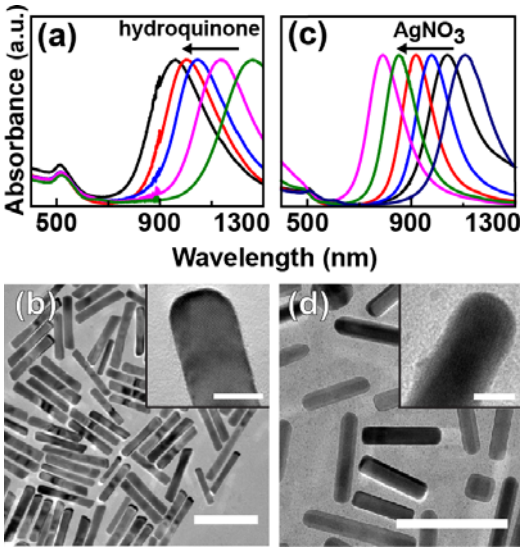

Figure 7.1. (a) Electronic absorption spectra of gold nanorods with varying concentration of reducing agent, hydroquinone. (b) Transmission electron micrograph of gold nanorods. Scale bar: 60 nm. Inset: High magnification electron micrograph. Scale bar: 10 nm. (c) Electronic absorption spectra of Au@Ag nanorods with varying degrees of $AgNO_3$ added. (d) Transmission electron micrograph of Au@Ag nanorods. Scale bar: 60 nm. Inset: High magnification electron micrograph of Au@Ag nanorods. Scale bar: 10 nm.

Here, we investigated the structural properties of Au@Ag nanorods using coherent nanoarea electron diffraction (NED) and high-angle annular dark-field scanning transmission electron microscopy (HAADF-STEM). Coherent NED provides localized information on the nanostructure's facet size, facet sharpness, and may be used to quantify the directions of high-index facets.[13] HAADF-STEM provides atomic resolution images of core-shell nanostructures and the contrast necessary to resolve interface sharpness.

Gold nanorods were synthesized using a recently developed, high-yield seed-mediated technique that produces monocrystalline gold nanorods with LSPRs ranging from 800 – 1300 nm, as shown in Figure 7.1.[14] This synthetic procedure uses a relatively weak reducing agent, hydroquinone, to slow the kinetics of crystal growth. Notably, the resulting nanorods have asymmetrical endcaps rather than spherical endcaps found in ascorbic acid-reduced nanorods. Using transmission electron microscopy and electronic absorption spectroscopy, we confirmed the morphological and optical properties of the nanorods. In particular, we studied long aspect ratio nanorods with transverse diameters of approximately 15 nm and lengths between 75 – 110 nm. Epitaxial growth of silver was accomplished using well-established protocols.[15,16]

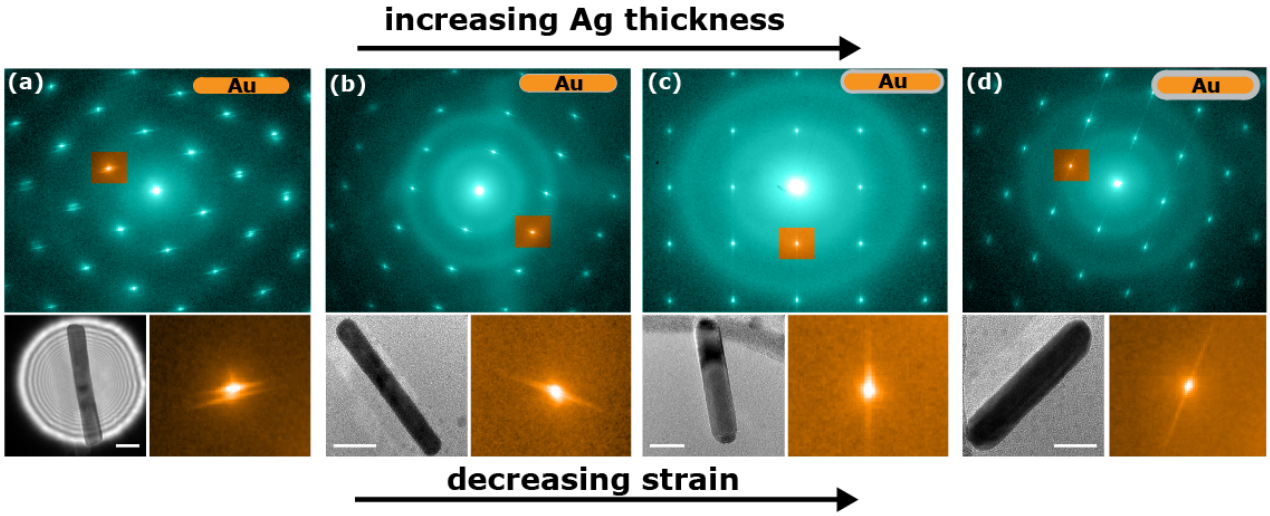

Figure 7.2. Coherent NED revealed anisotropic, elongated diffraction spots with varying degrees of splitting in (a) gold nanorods (strong splitting), Au@Ag nanorods with an average silver thickness of (b) < 1 nm (weak splitting), (c) 1 – 2 nm (no splitting), and (d) 3 – 4 nm (no splitting). Diffraction streak splitting is indicative of internalized bending and twisting of the nanorod. Scale bar: 30 nm.

Despite the facile synthesis, excellent biocompatibility, colloidal stability, and optical tunability of gold nanorods, they lack the superior plasmonic properties of silver nanocrystals,

primarily due to gold's interband transitions.[17] For sensing applications, where sensitivity and a low limit of detection are crucial, improved plasmonic properties are highly desirable. Hence, we investigated the optical and structural properties of Au@Ag core-shell nanorods because they maintain many of the desirable characteristics of gold nanorods, such as stability, and inherit the improved plasmonic properties of silver nanocrystals.[15,18–20] We chose gold nanorods as the core material because they are easily synthesized in nonhazardous aqueous chemistry, have tunable optical properties, and have a high yield. Epitaxial growth of silver onto gold is possible because the bulk lattice constant of gold (a = 4.080 Å) is similar to that of silver (a = 4.090 Å). Au@Ag core-shell nanorods are highly stable in aqueous solution and their LSPR may be tuned by varying either the aspect ratio of the gold nanorod or the thickness of epitaxially grown silver.[18,19]

Figure 7.2 shows representative coherent NED patterns (in cyan) of four nanorod samples, their corresponding bright-field transmission electron microscopy (TEM) images, and magnified diffraction spot (in orange). The gold nanorod sample shows a splitting in the diffraction pattern which could indicate the presence of a twin, grain boundary, or bending within the nanorod. As silver was epitaxially grown from sub-monolayer coverage to several nanometers (3 – 4 nm) of thickness the splitting diminished and sharp diffraction spots were observed. When a 1 – 2 nm thick silver shell was grown around the gold core, an intermediate state with a high degree of surface roughness was observed. As additional layers of silver were grown, the facet streaks became longer, indicating sharpening of the facets. Facet sharpness parameters measured from the {1-10} planes of [100] diffraction patterns were 0.15, 0.15, 0.10, and 0.18 $Å^{-1}$, respectively, for gold nanorods and Au@Ag nanorods with increasing silver thickness. This demonstrates that the facet sharpness for the Au@Ag nanorod sample with

1 – 2 nm of silver had an increased facet roughness whereas the Au@Ag nanorod sample with 3 – 4 nm of silver had an increased facet sharpness as compared to the gold nanorod. In summary, our results indicate that epitaxially grown silver relieves bending within the nanorod. This is a surprising result because in traditional epitaxial systems such as thin films, heteroepitaxial layers increase or add strain to the substrate.[21]

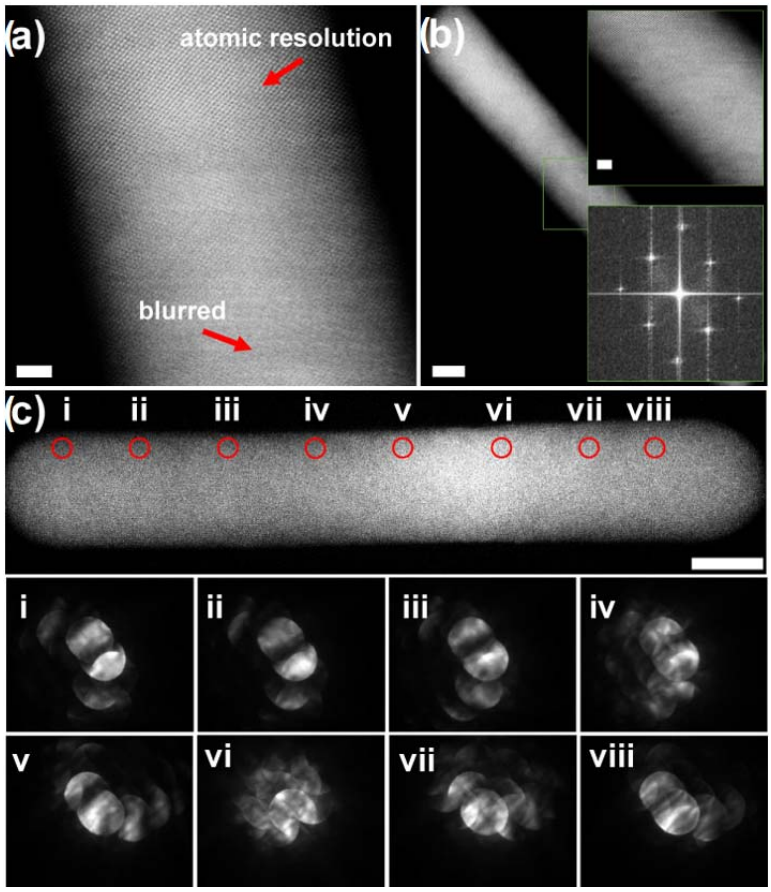

Figure 7.3 HAADF-STEM image of a gold nanorod illustrating areas with atomic resolution and blurring. Scale bar: 2 nm. (b) Low magnification image of a gold nanorod. Scale bar: 10 nm. Inset: atomic resolution image of the mid-section of the nanorod and its corresponding Fourier transform showing splitting of reflections caused by bending/twisting of the nanorod. Scale bar: 2 nm. (c) HAADF-STEM diffraction maps of the gold nanorod in (b) at positions (i) through (viii). Scale bar: 10 nm.

To confirm the mechanism for the observed splitting, we acquired HAADF-STEM images and scanning diffraction patterns, as shown in Figure 7.3. The HAADF-STEM images

show an interesting trend—only part of the nanorod was observed with atomic resolution, while the remaining nanorod was blurred. The presence of sharp atomic resolution STEM images relies on a highly focused probe as well as the sample being on a consistent low-index zone axis such that the probe electrons channel down atomic columns. Our observation indicates that since only part of the nanorod was imaged at atomic resolution, the remaining portion of the nanorod was likely strained and bent away. The Fourier transform in portions of atomic resolution STEM images revealed splitting in the reflections, further confirming bent or twisted nanorods. Additionally, scanning diffraction maps yield clear diffraction patterns showing a high degree of bending in these nanorods.

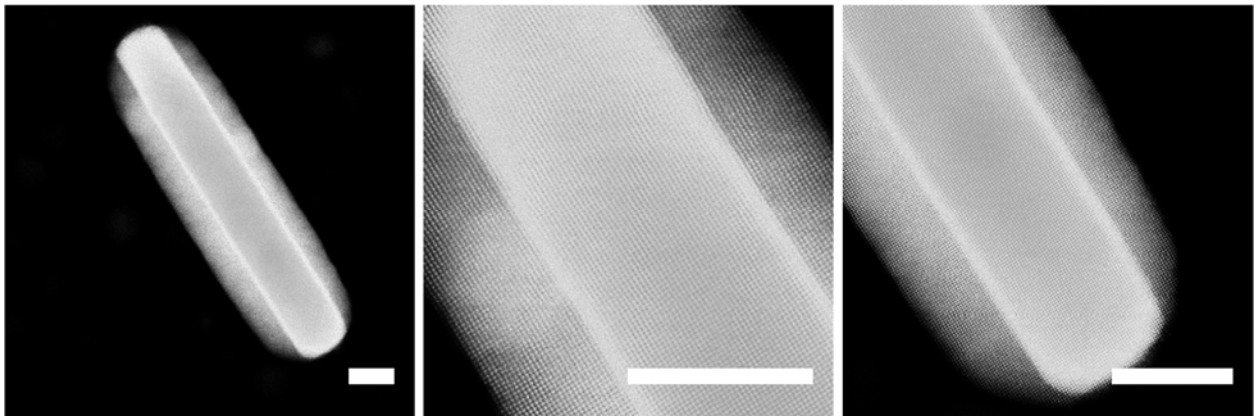

Figure 7.4. HAADF-STEM images of Au@Ag nanorods with silver shell thicknesses of 4 – 7 nm. Scale bar: 10 nm. Atomic resolution was observed throughout the entire Au@Ag nanostructure.

As observed in Figure 7.4, epitaxial growth of 1 – 2 nm of silver around a gold nanorod core showed clear atomic resolution without severe bending as observed with HAADF-STEM. The addition of a silver shell (> 3 nm) reduced the bending of nanorods and enhanced the sharpness of facets. This is surprising because during traditional semiconductor heteroepitaxy (Frank–van der Merwe layer-by-layer growth) the addition of films on the substrate increases strain when a lattice constant mismatch exists. Strain builds up as additional layers are grown.

The strain can be relieved by the formation of defects, such as dislocations, or the breakdown of layer-by-layer growth (*i.e.*, island formation). Our results indicate that the heteroepitaxy of silver onto gold reduces the bending and eventually forms very sharp facets with an intermediate rougher state.

In summary, we investigated the structural properties of gold and Au@Ag nanorods whose understanding can lead to improved use of this novel class of nanostructure in imaging using highly sensitive chemical sensing techniques such as surface-enhanced Raman spectroscopy (SERS). While strain engineering has been used extensively by the semiconductor industry to tune the electrical properties of devices by enhancing carrier mobility,[22,23] strain engineering of plasmonic substrates and nanocrystals is largely unexplored. Park and co-workers theoretically investigated strained gold and silver nanocrystals using Mie theory.[24–26] Their calculations indicate that strain can improve the near-field optical properties of certain geometries of nanocrystals and attributed this effect to changes in electron density. As observed by coherent NED the observation of bending in gold nanorods may prove useful in designing optical probes in future studies with enhanced optical properties.

7.3 Experimental

Materials. Cetyltrimethylammonium bromide (CTAB, >99%), cetyltrimethylammonium chloride (CTAC, >98%), silver nitrate (99%), gold (III) chloride hydrate (>99 %), L-ascorbic acid (AA, >99%), hydroquinone (>99.5%), sodium polyacrylate (PAA, ~5,100 MW), sodium chloride (NaCl, >99%), poly (allylamine hydrochloride) (PAH, ~15,000 MW), and methylene blue (>82%) were purchased from Sigma-Aldrich and used without further purification. Ultrathin holey carbon transmission electron microscopy grids were purchased from Ted Pella. TEM grids were prepared by allowing a 10 μL droplet of solution air dry on the grid. UV-Vis-NIR

absorbance spectra were measured with a Cary 5G spectrophotometer in a 1 cm path length fused silica cuvette.

Gold nanorod synthesis. Long aspect ratio hydroquinone-reduced gold nanorods were prepared by following the procedure described by Zubarev and coworkers.[14] Briefly, a seed solution was prepared by rapidly stirring 0.5 mL of $HAuCl_4$ (0.01 M) with 9.5 mL of CTAB (0.1 M), resulting in a brilliant yellow-orange solution. To the seed solution, 0.46 mL of ice-cold, freshly prepared 0.01 M $NaBH_4$ containing 0.01 M NaOH was added. The solution immediately turned a light brown color indicating the formation of CTAB stabilized seed nanocrystals. The seed solution was allowed to sit at room temperature for a minimum of one hour to fully hydrolyze remaining borohydride species. Gold nanorods were prepared in ~100 mL batches containing 95 mL of 0.01 M CTAB, 5 mL $HAuCl_4$, and 0.7 mL of 0.1 M $AgNO_3$. To this solution, varying volumes of hydroquinone (0.1 M) were added to tune the aspect ratio. In a typical synthesis, 5 – 10 mL of hydroquinone was added. The addition of hydroquinone turned the solution colorless after 30 seconds. Finally, 1.6 mL of seed solution was added and gently mixed for 20 seconds. After several hours the solution turned dark brown indicating the formation of long aspect ratio gold nanorods. All solutions were allowed 24 hours to complete growth before purification. Gold nanorod solutions were purified *via* centrifugation at 5250 × g for three hours twice to remove excess CTAB and growth reagents.

Au@Ag nanorod synthesis. Silver shell growth was accomplished by dispersing purified CTAB stabilized gold nanorods in 0.1 M CTAC.[15] In a typical procedure, a 7 mL aliquot of gold nanorods (OD ~ 18.5) in CTAC were mixed with varying amounts (0.15 – 2 mL) of 10 mM $AgNO_3$. Ascorbic acid (0.1 M) acted as the reducing agent. The volume of ascorbic acid added

was one-half the volume of $AgNO_3$. Samples were placed in an oven at 60 °C for a minimum of three hours to complete the reduction of silver.

Nanoarea electron diffraction and electron microscopy. Coherent nanoarea electron diffraction (NED) patterns were acquired with a 197 kV JEOL JEM2010F transmission electron microscope with parallel probe sizes of 55 – 120 nm and were recorded onto imaging plates. The nanorods were tilted onto a low-index zone axis, typically [001] or [110]. High-angle annular dark-field scanning transmission electron microscopy (HAADF-STEM) images were acquired with a 200 kV JEOL JEM2200FS aberration corrected STEM with a probe size of ~0.1 nm. To detect the presence of nanorod bending, we reduced the convergence angle and scanned the beam while collecting diffraction patterns onto a CCD.

7.4 References

(1) Zhang, H.; Jin, M.; Xiong, Y.; Lim, B.; Xia, Y. Shape-Controlled Synthesis of Pd Nanocrystals and Their Catalytic Applications. *Acc. Chem. Res.* **2013**, *46*, 1783–1794.

(2) Hu, Y.; Liu, Y.; Sun, Y. Mesoporous Colloidal Superparticles of Platinum-Group Nanocrystals with Surfactant-Free Surfaces and Enhanced Heterogeneous Catalysis. *Adv. Funct. Mater.* **2015**, *25*, 1638–1647.

(3) Qian, X.; Peng, X.-H.; Ansari, D. O.; Yin-Goen, Q.; Chen, G. Z.; Shin, D. M.; Yang, L.; Young, A. N.; Wang, M. D.; Nie, S. In Vivo Tumor Targeting and Spectroscopic Detection with Surface-Enhanced Raman Nanoparticle Tags. *Nat Biotech* **2008**, *26*, 83–90.

(4) Kircher, M. F.; Zerda, A. de la; Jokerst, J. V.; Zavaleta, C. L.; Kempen, P. J.; Mittra, E.; Pitter, K.; Huang, R.; Campos, C.; Habte, F.; *et al.* A Brain Tumor Molecular Imaging Strategy Using a New Triple-Modality MRI-Photoacoustic-Raman Nanoparticle. *Nat. Med.* **2012**, *18*, 829–834.

(5) Bogart, L. K.; Pourroy, G.; Murphy, C. J.; Puntes, V.; Pellegrino, T.; Rosenblum, D.; Peer, D.; Lévy, R. Nanoparticles for Imaging, Sensing, and Therapeutic Intervention. *ACS Nano* **2014**, *8*, 3107–3122.

(6) Huschka, R.; Barhoumi, A.; Liu, Q.; Roth, J. A.; Ji, L.; Halas, N. J. Gene Silencing by Gold Nanoshell-Mediated Delivery and Laser-Triggered Release of Antisense Oligonucleotide and siRNA. *ACS Nano* **2012**, *6*, 7681–7691.

(7) Kang, B.; Afifi, M. M.; Austin, L. A.; El-Sayed, M. A. Exploiting the Nanoparticle Plasmon Effect: Observing Drug Delivery Dynamics in Single Cells *via* Raman/Fluorescence Imaging Spectroscopy. *ACS Nano* **2013**, *7*, 7420–7427.

(8) DeSantis, C. J.; Weiner, R. G.; Radmilovic, A.; Bower, M. M.; Skrabalak, S. E. Seeding Bimetallic Nanostructures as a New Class of Plasmonic Colloids. *J. Phys. Chem. Lett.* **2013**, *4*, 3072–3082.
(9) Rycenga, M.; Cobley, C. M.; Zeng, J.; Li, W.; Moran, C. H.; Zhang, Q.; Qin, D.; Xia, Y. Controlling the Synthesis and Assembly of Silver Nanostructures for Plasmonic Applications. *Chem. Rev.* **2011**, *111*, 3669–3712.
(10) Sun, Y.; Xia, Y. Shape-Controlled Synthesis of Gold and Silver Nanoparticles. *Science* **2002**, *298*, 2176–2179.
(11) Cobley, C. M.; Au, L.; Chen, J.; Xia, Y. Targeting Gold Nanocages to Cancer Cells for Photothermal Destruction and Drug Delivery. *Expert Opin. Drug Deliv.* **2010**, *7*, 577–587.
(12) Xu, Z.; Hou, Y.; Sun, S. Magnetic Core/Shell Fe3O4/Au and Fe3O4/Au/Ag Nanoparticles with Tunable Plasmonic Properties. *J. Am. Chem. Soc.* **2007**, *129*, 8698–8699.
(13) Shah, A. B.; Sivapalan, S. T.; DeVetter, B. M.; Yang, T. K.; Wen, J.; Bhargava, R.; Murphy, C. J.; Zuo, J.-M. High-Index Facets in Gold Nanocrystals Elucidated by Coherent Electron Diffraction. *Nano Lett.* **2013**, *13*, 1840–1846.
(14) Vigderman, L.; Zubarev, E. R. High-Yield Synthesis of Gold Nanorods with Longitudinal SPR Peak Greater Than 1200 nm Using Hydroquinone as a Reducing Agent. *Chem. Mater.* **2013**, *25*, 1450–1457.
(15) Okuno, Y.; Nishioka, K.; Kiya, A.; Nakashima, N.; Ishibashi, A.; Niidome, Y. Uniform and Controllable Preparation of Au–Ag Core–shell Nanorods Using Anisotropic Silver Shell Formation on Gold Nanorods. *Nanoscale* **2010**, *2*, 1489–1493.
(16) Liu; Guyot-Sionnest, P. Mechanism of Silver(I)-Assisted Growth of Gold Nanorods and Bipyramids. *J. Phys. Chem. B* **2005**, *109*, 22192–22200.
(17) Maier, S. A. *Plasmonics: Fundamentals and Applications*; Springer, 2007.
(18) Fernanda Cardinal, M.; Rodríguez-González, B.; Alvarez-Puebla, R. A.; Pérez-Juste, J.; Liz-Marzán, L. M. Modulation of Localized Surface Plasmons and SERS Response in Gold Dumbbells through Silver Coating. *J. Phys. Chem. C* **2010**, *114*, 10417–10423.
(19) Anh, D. T. N.; Singh, P.; Shankar, C.; Mott, D.; Maenosono, S. Charge-Transfer-Induced Suppression of Galvanic Replacement and Synthesis of (Au@Ag)@Au Double Shell Nanoparticles for Highly Uniform, Robust and Sensitive Bioprobes. *Appl. Phys. Lett.* **2011**, *99*, 073107.
(20) Jiang, R.; Chen, H.; Shao, L.; Li, Q.; Wang, J. Unraveling the Evolution and Nature of the Plasmons in (Au Core)–(Ag Shell) Nanorods. *Adv. Mater.* **2012**, *24*, OP200–OP207.
(21) Cao, G.; Wang, Y. *Nanostructures and Nanomaterials: Synthesis, Properties, and Applications*; 2nd ed.; World Scientific, 2011.
(22) Giri, G.; Verploegen, E.; Mannsfeld, S. C. B.; Atahan-Evrenk, S.; Kim, D. H.; Lee, S. Y.; Becerril, H. A.; Aspuru-Guzik, A.; Toney, M. F.; Bao, Z. Tuning Charge Transport in Solution-Sheared Organic Semiconductors Using Lattice Strain. *Nature* **2011**, *480*, 504–508.
(23) Feng, J.; Qian, X.; Huang, C.-W.; Li, J. Strain-Engineered Artificial Atom as a Broad-Spectrum Solar Energy Funnel. *Nat. Photonics* **2012**, *6*, 866–872.
(24) Ben, X.; Park, H. S. Strain Engineering Enhancement of Surface Plasmon Polariton Propagation Lengths for Gold Nanowires. *Appl. Phys. Lett.* **2013**, *102*, 041909.
(25) Qian, X.; Park, H. S. Strain Effects on the SERS Enhancements for Spherical Silver Nanoparticles. *Nanotechnology* **2010**, *21*, 365704.

(26) Qian, X.; Park, H. S. The Influence of Mechanical Strain on the Optical Properties of Spherical Gold Nanoparticles. *J. Mech. Phys. Solids* **2010**, *58*, 330–345.